

Dissertation
submitted to the
Combined Faculty of Mathematics, Engineering and Natural Sciences
of Heidelberg University, Germany
for the degree of
Doctor of Natural Sciences

Put forward by

Menno Door

born in: Emden

Oral examination: 22.07.2024

**Precision Mass and Mass-Ratio Measurements
of Neon and Ytterbium Isotopes
for Tests of Fundamental Physics**

Referees:

Prof. Dr. Klaus Blaum

Prof. Dr. Skyler Degenkolb

High-Precision Mass and Mass-Ratio Determinations of Neon and Ytterbium Isotopes for Tests of Fundamental Physics

During the research for this thesis, several mass ratios were measured with a relative uncertainty of a few parts per trillion using the cryogenic Penning trap mass spectrometer PENTATRAP. The determination of the mass ratio of the ^{20}Ne isotope against the ^{12}C isotope reached a relative uncertainty of 4×10^{-12} and, with a deviation of 4 standard deviations to the former literature value, results in the most precise mass measurement in atomic mass units to date and an improvement of this mass value by a factor of nineteen. This precision mass determination is used in a test of the theory of quantum electrodynamics (QED), especially confirming one- and two-loop corrections of bound-state QED at highest precision. The determination of mass ratios between the five stable even ytterbium isotopes reached a precision of also 4×10^{-12} . These mass ratios are used in a King plot analysis of isotope shifts in atomic transitions to exclude the existence of a proposed new boson mediating a new 5th force. The measurements improve the respective mass ratios determined from literature masses by one to two orders of magnitude. Lastly, the binding energies of the valence electrons in $^{172}\text{Yb}^{41+}$ and $^{172}\text{Yb}^{42+}$ are determined to sub-eV precision as a cross-check of the measurement accuracy and a test of the theoretical models and methods used to calculate these binding energies.

The presented cyclotron frequency determinations show an improvement of at least a factor of two compared to previous measurements of isotope mass ratios at PENTATRAP and an improvement of a factor of six in the determination of binding energies of highly charged ions, made possible by an upgrade of the experiments detection system within this thesis. The measurement of the mass of ^{20}Ne was the first measurement of light ions and the first measurement against the atomic mass unit reference ^{12}C at this experiment, and, with the precision demonstrated, paves the way for further high-precision mass determinations in atomic mass units in this experiment. The presented accuracy of binding energy determinations will enable stringent tests of QED-theory in the future by determining the binding energies of electrons in heavier atoms and higher charge states.

Hochpräzise Bestimmung der Massen und Massenverhältnisse von Neon- und Ytterbiumisotopen zur Überprüfung grundlegender physikalischer Prinzipien

Im Rahmen dieser Arbeit wurden mithilfe des kryogenen Penningfallen-Massenspektrometers PENTATRAP mehrere Massenverhältnisse mit einer relativen Unsicherheit von einigen 1×10^{-12} gemessen. Die Bestimmung des Massenverhältnisses der Isotope ^{20}Ne und ^{12}C erreichte eine relative Unsicherheit von 4×10^{-12} mit einer Abweichung von 4 Standardabweichungen zum bisherigen Literaturwert. Dies ist die bisher genaueste Massenmessung in atomaren Masseneinheiten und entspricht einer Verbesserung dieses Massenwertes um den Faktor 19. Diese Präzisionsmassenbestimmung dient der Überprüfung und Bestätigung der Theorie der Quantenelektrodynamik (QED), insbesondere der Bestätigung der one- und two-loop Korrekturen der bound-state-QED mit höchster Präzision. Die Bestimmung der Massenverhältnisse zwischen den fünf stabilen geraden Ytterbium-Isotopen erreichte ebenfalls eine Präzision von 4×10^{-12} . Diese Massenverhältnisse werden in einer King-Plot-Analyse von Isotopenverschiebungen in atomaren Übergängen verwendet, um die Existenz eines vorgeschlagenen neuen Bosons und einer damit zusammenhängenden fünften fundamentalen Wechselwirkung auszuschließen. Im Vergleich zu den aktuellen Literaturwerten dieser Massenverhältnisse, wird eine Verbesserung von bis zwei Größenordnungen erreicht. Schließlich werden die Bindungsenergien der Valenzelektronen in $^{172}\text{Yb}^{41+}$ und $^{172}\text{Yb}^{42+}$ mit sub-eV-Präzision bestimmt, um die Messgenauigkeit zu überprüfen und die zur Berechnung dieser Bindungsenergien verwendeten theoretischen Modelle und Methoden zu testen.

Die vorgestellten Bestimmungen von Zyklotronfrequenz-Verhältnissen zeigen eine Verbesserung in der erreichten Genauigkeit um mindestens einen Faktor zwei im Vergleich zu früheren Messungen der Isotopenmassenverhältnisse bei PENTATRAP sowie eine Verbesserung um einen Faktor sechs bei der Bestimmung der Bindungsenergien hochgeladener Ionen, ermöglicht durch eine Verbesserung des Detektionssystems im Rahmen dieser Arbeit. Die Messung der Masse von ^{20}Ne ist die erste Messung mit leichten Ionen und die erste Messung als Massenverhältnis zu dem Isotope ^{12}C an diesem Experiment und ebnet mit der gezeigten Präzision den Weg für weitere hochpräzise Massenbestimmungen in atomaren Masseneinheiten bei PENTATRAP. Mit möglichem Zugang zu schwereren Atomen und höheren Ladungszuständen in der Zukunft, erlaubt die präsentierte Genauigkeit der Bindungsenergiebestimmung direkte, hochpräzise Tests der QED-Theorie.

Contents

1	Introduction	1
1.1	Test of bound-state QED	2
1.2	Mass-ratios for the search of new physics	4
1.3	Structure of this thesis	5
2	Penning Trap Theory	7
2.1	The ideal Penning trap	7
2.2	Mass spectrometry with Penning traps	11
2.3	The real Penning trap	15
2.3.1	Electrostatic field imperfections	16
2.3.2	Magnetic field imperfections	18
2.3.3	Combined field imperfections	19
2.3.4	Tilt, ellipticity and the invariance theorem	20
2.3.5	Relativistic shift	21
2.3.6	Image charge shift	22
2.3.7	Image current shift	23
2.4	Driving and coupling modes	23
2.5	Detection methods	25
2.5.1	Axial detection system	25
2.5.2	Radial frequency determination	29
2.5.3	Phase sensitive measurement methods	29
3	The Pentatrap Mass Spectrometer	35
3.1	Ion production and transport	35
3.2	Penning trap apparatus	38
3.2.1	Superconducting magnet and stabilization system	38
3.2.2	Cryogenic insert - traps and electronics	39
3.2.3	Room temperature electronics	43
3.3	Measurement scheme	47
3.3.1	Measurement preparation	48
3.3.2	Main measurement sequence	49
4	Data Analysis and Trap Characterization	51
4.1	Data analysis	51
4.1.1	Extracting axial frequencies and phases from measurement data	51
4.1.2	Phase unwrapping, N determination and ν_+ frequency	52
4.1.3	Determining the free cyclotron frequency	53
4.1.4	Ratio determination via interpolation	54
4.1.5	Ratio determination via polynomial fit	55
4.1.6	Cancellation method	56
4.2	Characterization measurements	56

4.2.1	Tuning ratio optimization	57
4.2.2	Odd trap potential anharmonics	57
4.2.3	Magnetic field inhomogeneities	58
4.2.4	Detection system temperature	59
4.2.5	Axial dip measurement systematics	59
4.2.6	Phase transfer function	60
4.2.7	Image charge shift	61
5	Mass Determination of ^{20}Ne	63
5.1	Ion charge state choice and production	63
5.2	Preliminary systematic considerations	64
5.3	Cyclotron frequency ratio	65
5.4	Extrapolation to zero excitation amplitude	69
5.5	Systematic corrections	70
5.6	Atomic mass of neutral ^{20}Ne	74
5.7	g -factor of hydrogenlike $^{20}\text{Ne}^{9+}$	74
6	Ytterbium Mass-Ratio Determinations	77
6.1	Ion production anwithring choices	77
6.2	Mass-ratio determinations with detection system tuning	79
6.2.1	Systematic corrections	84
6.2.2	Nuclear mass ratios and neutral masses	85
6.3	Mass-ratio determinations with trap-depth tuning	86
6.4	Binding energy measurement	86
6.5	King Plot analysis	87
7	Conclusion & Outlook	89
7.1	Conclusion	89
7.2	Outlook	92
7.2.1	Improvements of the apparatus	92
7.2.2	Additional motivations for future mass determinatios	95
	List of Publications	96
	Bibliography	99
A	Appendix	107
A.1	Ytterbium cyclotron frequency ratios	107
A.2	Impact of fluctuating electrostatic potential	109
	Acknowledgements	111

List of Figures

1.1	Yb King plot example	5
1.2	Exclusion plot	6
2.1	Cyclotron motion	7
2.2	Quadrupolar trapping potential	8
2.3	Axial motion	8
2.4	Radial motion	9
2.5	Full ion motion	10
2.6	Precision and accuracy	14
2.7	Rendering of PENTATRAP's Penning trap	15
2.8	PENTATRAP's trap and calculated axial potential	16
2.9	Magnetic moment of an ion	18
2.10	Field misalignment	20
2.11	Resonant excitation	24
2.12	Image current	25
2.13	Detection system principle	26
2.14	Plor resonator response impedance and coil pulling shift	27
2.15	Plot dip-fit function	28
2.16	PnP measurement scheme and phase space	31
2.17	N determination principle	32
3.1	EBIT simple schematic	35
3.2	Beamline overview	36
3.3	Magnet stabilization Allan plot	39
3.4	Cryogenic insert	39
3.5	Trap tower	40
3.6	Pulse shaping	41
3.7	Varactor board	41
3.8	Varactor circuit upgrade	42
3.9	Varactor impact	43
3.10	Resonator tunability trap 2 & 3	43
3.11	Allan deviations StaRep	45
3.12	Detection chain	46
3.13	Ion configuration for measurement	48
3.14	Measurement procedure	50
4.1	Phase spectrum example	51
4.2	Phase spectrum example	53
4.3	Interpolation method	54
4.4	Polynomial fit method	55
4.5	Simple tuning ratio optimization	57
4.6	Trap parameter extraction	58

4.7	Linear magnetic field gradient determination	59
4.8	Nonlinear phase shift	61
5.1	Neon campaign example dip fits	65
5.2	Neon and carbon example phase and axial data	67
5.3	Neon and carbon example cyclotron data	68
5.4	Neon ratios	69
5.5	Neon ratio extrapolations	70
5.6	Tuning ratio and B_1 measurements	72
5.7	Neon position investigation	73
5.8	Neon dip fit scan	74
5.9	Neon mass vs. AME	74
6.1	Yb isotopes target	77
6.2	Ytterbium campaign preliminary check of relativistic shifts	80
6.3	Ytterbium campaign example dip fits	82
6.4	Ytterbium example phase and axial data	82
6.5	Ytterbium example cyclotron data	83
6.6	Results cyclotron ratio 172/176 Yb - with varactor tuning	83
6.7	Dip lineshape effect	85
6.8	Results cyclotron ratio 172 Yb 42/41 - with varactor tuning	87
6.9	Mass normalized King plot	88
A.1	Results cyclotron ratio 172/168 Yb - with varactor tuning	107
A.2	Results cyclotron ratio 172/170 Yb - with varactor tuning	108
A.3	Results cyclotron ratio 172/174 Yb - with varactor tuning	108
A.4	Results cyclotron ratio 172 Yb 43/42 - with varactor tuning	108
A.5	Impact of voltage noise on ω_+	109

List of Tables

3.1	Geometric parameters of PENTATRAP's 5-pole Penning trap	40
3.2	Leading order even electrostatic coefficients c_i from simulation	40
5.1	Trap properties during the Neon mass campaign	66
5.2	Neon measurement settings	66
5.3	Systematic corrections of Neon measurement campaign	71
5.4	Thermal amplitudes	71
5.5	Field coefficients Neon meas.	71
5.6	$^{20}\text{Ne}^{9+}$ bound electron g -factor comparison	75
6.1	Approximate values for tuned parameters of the ytterbium campaign	78
6.2	Ytterbium campaign trap parameters	81
6.3	Ytterbium measurement settings	81
6.4	Yb isotopes cyclotron frequency ratios	83
6.5	Yb campaign systematic corrections	84
6.6	Yb cyclotron frequency and nuclear mass ratios	85
6.7	Yb campaign neutral atomic masses	86
6.8	Yb cyclotron frequency ratios determined using trap depth tuning	86
6.9	Yb cyclotron frequency ratios and binding energies	87

Chapter 1

Introduction

All fundamental particles and interactions are summarized in the so-called Standard Model of Particle Physics (SM) with the exception of the gravitational force, which could so far not be unified with the SM and is described by the theory of general relativity (GR). It is common knowledge that the SM is incomplete because it cannot explain some significant observations made by experiments. Prominent examples are the observation of neutrino oscillation between flavor eigenstates which require at least two neutrino mass eigenstates to be non-zero [1, 2], the baryon asymmetry in the universe (there is *much* more matter than antimatter) [3] and the indirect observation of dark matter and dark energy by astronomical observations of e.g. deviations in the gravitational pull of observed galaxy cluster mergers [4–6], the flatness of rotational curves of galaxies [7], the observed structure formation of matter in the universe [8], and the accelerating expansion of the universe [9]. Research in fundamental physics aims at improving the confidence and accuracy of the predictions made by the theoretical models (testing the SM) and probing for new interactions and particles spawning new theoretical models that can explain the so far unexplained observations (probing physics beyond SM), while the latter profits from the former.

Precision mass measurements can help in these endeavors, since the mass of an atom includes also the energy of the interactions, the strong and electromagnetic forces keeping the particles together, which is due to Einstein's famous relationship $E = mc^2$ equivalent to a mass. Given the masses of the proton, neutron and electron (m_p , m_n , m_e), the mass of a neutral atom of element X is given by:

$$m\left({}^A X_Z\right) = Z(m_p + m_e) + (A - Z)m_n - E_{\text{nucl.}} - E_{\text{elec.}}, \quad (1.1)$$

with the proton number Z , defining the element, the total number of nucleons A , the electronic binding energy $E_{\text{elec.}}$, which must be supplied to the system to overcome the electromagnetic force holding the electrons in place, and the nuclear binding energy $E_{\text{nucl.}}$ which must be supplied to overcome the *strong force* to split the nucleus into its constituents¹.

The mass differences between isotopes having the same number of electrons can be used to probe the strong force and to gain insight into nuclear physics [10]. Vice versa, the mass differences of differently charged ions of the same isotope can be used to study and test quantum electrodynamics (QED) [11]. Nuclear masses also affect the interaction with the electrons in the bound system of an atom or ion and are needed for tests of bound-state QED [12]. Even metastable electronic states (with sufficient life time) can be measured as mass differences with respect to the ground state [13]. Furthermore, nuclear reactions, which include interactions via the weak force, can be studied by measuring the Q-value of the reaction [14–16] — i. e. the mass difference between the mother and daughter nucleus, which is equal to the sum of energy (and

¹The minus in the equation is kind of arbitrary, the binding energies can also be defined to be negative.

masses) released in the decay. Comparison of the Q-value with the released energy determined in other experiments can be used to establish new limits on neutrino masses or to test the theory of special relativity [17, 18].

The mass of an atom or ion, mass ratios, and mass differences are therefore a window to fundamental forces which can be used to test the respective theoretical models behind them. Most of the motivations mentioned above require mass measurements at a level of a few 10 parts per trillion (ppt) relative precision or lower, which can only be performed by state-of-the-art Penning-trap mass spectrometers (PTMS) based on the Fourier-transform ion-cyclotron-resonance technique (FT-ICR) [19]. PENTATRAN [20], the PTMS experiment described and used in this thesis, is one of the most accurate mass spectrometers around the world and is steadily improving its accuracy.

Only a few experiments worldwide are competitive (or possibly will be competitive) with at about 10 ppt relative precision or better: the Liontrap experiment at JGU in Mainz (specialized in light isotopes and recently decommissioned) [21], the FSU-trap in Tallahassee (providing results even with only low charged ions) [22], the BASE Collaboration at CERN in Geneva (only proton / antiproton) [23], CHIPTRAP at MSU in East Lansing (currently in the build-up phase) [24] and TRAPSENSOR at UGR in Granada (also currently in the build-up phase and developing a novel optical eigenfrequency detection system) [25]. A comparison with the results of these other experiments allows us to verify our measurement accuracy [11]. However, given our now reached precision, the best verification can be made by measuring atomic binding energies and comparing them with theoretical calculations, which is part of this thesis within the ytterbium measurement campaign.

In the following sections, the specific motivations behind the measurements performed within this thesis are explained in more detail.

1.1 Test of bound-state QED

Quantum electrodynamics (QED) is the theory of the electromagnetic interaction between charged particles and photons. This theory is considered the most successful theory in physics because it was tested to highest precision and did not fail so far [26–32].

Mass measurements for g -factor determination One prominent way to test QED theory in strong fields is the determination of the magnetic moment or g -factor of a bound electron in highly charged ions [28, 31–33]. The experimentally determined bound electron g -factor, given by

$$g_{\text{exp}} = 2 \frac{\nu_L}{\nu_c} \frac{m_e}{m_{\text{ion}}} \frac{q_{\text{ion}}}{e} = 2 \Gamma \frac{m_e}{m_{\text{ion}}} \frac{q_{\text{ion}}}{e} \quad , \quad (1.2)$$

relies on multiple measured quantities: The Larmor precession frequency ν_L of the spin state in a magnetic field, the free cyclotron frequency ν_c of the ion in that same magnetic field (often determined as a frequency ratio Γ in an experiment), and the charge-to-mass ratio of the electron and ion involved. Γ is also determined in a Penning-trap experiment with a stored single ion that probes the spin orientation of the valence electron by the continuous Stern-Gerlach effect in an inhomogeneous magnetic field and creates a Larmor-frequency resonance by driving spin flips with scanned microwaves irradiated into the trap [34].

The most precise value of the electron mass was measured in atomic mass units [35], which was actually determined in the same way by *trusting* QED and the theoretical g -factor and solving Equation 1.2 for the electron mass using an experimentally determined

Γ of the bound electron of $^{12}\text{C}^{5+}$:

$$m_e = \frac{g_{\text{theory}}}{2} \frac{e}{q_{\text{ion}}} \frac{m_{\text{ion}}}{\Gamma} . \quad (1.3)$$

This method arose from Penning-trap mass spectrometry, being a solution to the problem of the relativistic mass increase of a single trapped electron in the strong magnetic field of the Penning trap and the resulting increased measurement uncertainty. However, the determination of other g -factors to test QED theory is therefore somewhat correlated with the theory calculations in the electron mass determination. Although improvements in the calculations show no significant changes in the electron mass so far, complementary approaches are in the best interest of the science community, and recent determinations based on the extraction of the proton-electron-mass ratio from laser spectroscopy of vibrational modes in HD^+ start to reach competitive results [30].

The mass of the ion is also necessary and since the conversion factor to eV is an order of magnitude less precise than the electron mass in atomic mass units [36], it is favorable for current g -factor determinations and more precise QED tests to determine the involved ion mass also in atomic mass units. For this purpose, within this thesis the mass of $^{20}\text{Ne}^{10+}$ was measured in atomic mass units by determining the cyclotron frequency ratio of this ion to $^{12}\text{C}^{6+}$ being an almost perfect mass doublet. In a collaboration with the ALPHATRAP experiment [34], measuring Γ of the bound electron in hydrogenlike $^{20}\text{Ne}^{9+}$, an experimental g -factor could be extracted and compared to a theoretical prediction of the g -factor to the underlying QED theory [31].

Binding energy determinations As mentioned above, the binding energy difference between two charge states of an ion, can be extracted from a determined mass ratio of these ions. While the initial goal was to use the comparison to theory as a crosscheck to validate the measurement accuracy, the comparison can also be used with the motivation of QED tests in mind.

For tests of bound-state QED by comparing experimental and theoretical binding energies, the higher the charge state q the better: With increasing Z and q , the binding energy of the remaining electrons increases significantly. The bound electron in an $^{208}\text{Pb}^{81+}$ has an approximate binding energy of more than 100 keV [37]. This value is currently predicted by theory with an uncertainty of 0.3 eV, corresponding to a relative uncertainty on the full mass of the lead ion of approximately 1×10^{-12} . This kind of precision in mass measurement might be possible to achieve with the PENTATRAP experiment in the near future, but it is currently hindered by the fact that such a highly charged ion cannot be easily produced at low kinetic energy², allowing catching the ion in a Penning trap. In the future either the local HD-EBIT [38] will be upgraded to reach the necessary electron beam energies for efficient ionization to these high charge states, or its successor, the Hyper-EBIT, will take its place to provide PENTATRAP with ions up to bare lead or even heavier elements.

The binding energies extracted from the herein ytterbium ions are between the charge states of 41+, 42+ and 43+ with energies between 2 keV to 3.5 keV. Although direct QED contributions to the binding energy cannot be tested on a significant level, the electron-correlation effects due to the interaction between the bound electrons can possibly be tested given a relative measurement precision of approximately 5 ppt.

²These ions are easily produced in accelerator facilities using stripper foils. However, the corresponding kinetic energy of a few hundred MeV/u is not easily reduced to a level of few eV.

1.2 Mass-ratios for the search of new physics

The search for new physics with atomic physics experiments is a rather new field and tries to set limits on potential new forces and particles by performing high-precision experiments [39]. These low-energy precision physics experiments can be seen as complementary to high-energy physics tests at lower precision [40, 41]. Several models for possible dark matter candidates exist and so far no dark matter particles have been directly observed. However, several candidates have been constraint in the possible mass and interaction strengths [42, 43]. One beyond SM theory proposes the existence of a *5th force* mediated by a light boson with masses in the keV/c^2 to MeV/c^2 range that couples electrons and neutrons [39, 44, 45].

Isotope-shift (IS) spectroscopy can be used as a sensitive probe for the proposed fifth force by performing a so-called King plot analysis [46–48]. The isotope shift is the difference in frequency (energy) of the same transition in different isotopes $\nu_\alpha^{A,A'} = \nu_\alpha^A - \nu_\alpha^{A'}$. The theoretical description of the isotope shift from the SM perspective consists to first-order of two contributions: The mass shift and the field shift. Adding an additional term for the possible new interaction via the fifth force dependent on the number of neutrons, results in the following description of the IS between isotope A and A' :

$$\nu_\alpha^{A,A'} = F_\alpha \delta \langle r^2 \rangle_{A,A'} + K_\alpha \mu_{A,A'} + \frac{\alpha_{\text{NP}}}{\alpha_{\text{EM}}} D_\alpha \mathbf{h}_{A,A'} + \dots \quad (1.4)$$

The coefficients F , K , and D are transition-dependent factors and quantify the electronic contribution to the field shift, mass shift and a shift induced by a new boson, respectively. The mass contribution is given in the inverse mass difference $\mu_{A,A'} = 1/m_A - 1/m_{A'}$ and the field shift is proportional to the difference in the second order moment of the nuclear charge distribution $\delta \langle r^2 \rangle^{A,A'} = \langle r^2 \rangle^A - \langle r^2 \rangle^{A'}$. For the new interaction $\mathbf{h}_{A,A'} = A - A'$ represents the linear scaling of this contribution with the number of neutrons.

The King plot analysis is the comparison of two *mass normalized*³ transitions, measured in an atom or ion of multiple isotopes of one element, which is, in respect to the SM contributions, linear in first order [48, 49]:

$$\mu_{A,A'}^{-1} \nu_\gamma^{A,A'} = F_{\gamma\alpha} \mu_{A,A'}^{-1} \nu_\alpha^{A,A'} + K_{\gamma\alpha} + \frac{\alpha_{\text{NP}}}{\alpha_{\text{EM}}} D_{\gamma\alpha} \mathbf{h}_{A,A'}. \quad (1.5)$$

An illustration of such a King plot performed with transitions measured in ytterbium is given in Figure 1.1. With recent improvements in the precision of IS spectroscopy, the uncertainties of the inverse mass differences started to limit the precision at which the linearity could be tested [48, 50]. Improving the needed mass values is the motivation behind the ytterbium mass ratio measurements in this thesis. Masses in atomic mass units are actually not necessary here, the mass ratios between isotopes are sufficient, which is beneficial since determining the mass ratios between isotopes with rather small mass differences is not as difficult as measuring the isotopes against a reference in atomic mass units with largely different mass.

Considering the interpretation, the easy case is if the linearity of the respective King plot can be confirmed since it directly agrees with the SM and the parameter space for a fifth force interaction strength and mediator mass can be constraint⁴, see the exclusion plot Figure 1.2 with predictions of limits set by IS spectroscopy given

³Also frequency normalization is possible. Then the inverse mass difference takes the place of one of the transitions.

⁴With a small possibility that an actual new physics contribution exists that is by chance canceled with a higher order SM effect. This problem is dealt with by testing the linearity in different atomic systems (elements).

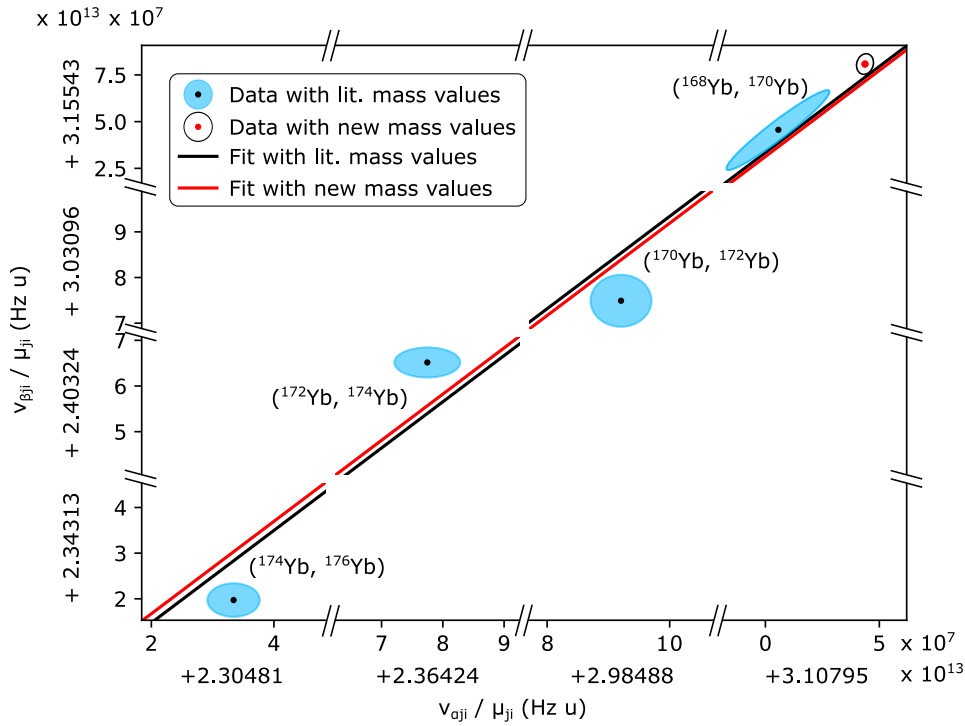


Figure 1.1: Example King plot created with the *current literature mass values* published in Reference [51]. Each axis corresponds to the differences in energy of a specific electronic transition determined between all even and stable ytterbium isotopes ($\nu_{\alpha}^{j,i}$ and $\nu_{\beta}^{j,i}$) and normalized by the respective inverse mass ratio ($\mu_{j,i}$). If the linearity of the King plot can be confirmed with higher precision, the interactions strength and mass of a fifth force mediator can be further constrained. In this publication, the mass value of the isotope ^{168}Yb was improved to increase the precision, at which the linearity could be tested.

different measurement uncertainties and a linear King plot. Increasing the precision of the experimental data, the resulting sensitivity of the linearity test is also improved and a larger parameter space can be constrained.

If a non-linearity is observed, the next-order SM effects have to be identified (rather it is a dominant non-linearity created by a higher-order mass shift or field shift and the respective order) and corrected to allow to extract stronger limits on new-physics contributions. Unfortunately, this has proven to be difficult because of insufficient precision in the necessary atomic and nuclear structure calculations [52]. On the other hand, this gives rise to the possibility of recasting the King plot analysis into a method for the extraction of higher-order nuclear structure parameters, as was done by our theory colleagues in a collaborative publication that included IS spectroscopy and our mass-ratio data [53]. This is in some way a full circle, since the King plot analysis was initially developed to extract the nuclear charge radius.

King plot analysis using isotope chains of other elements are of great interest, especially systems with lesser or at least significantly different impact of higher-order SM effects. For this purpose additional isotope mass ratios will be measured at PENTATRAP, e.g. the stable even isotopes of Ca, Sn and Sr.

1.3 Structure of this thesis

Building on the developments of many PhD students working on and with the PENTATRAP experiment before me, this thesis tries to give an overview (with many references to theses and publications of former colleagues for additional details, especially on exper-

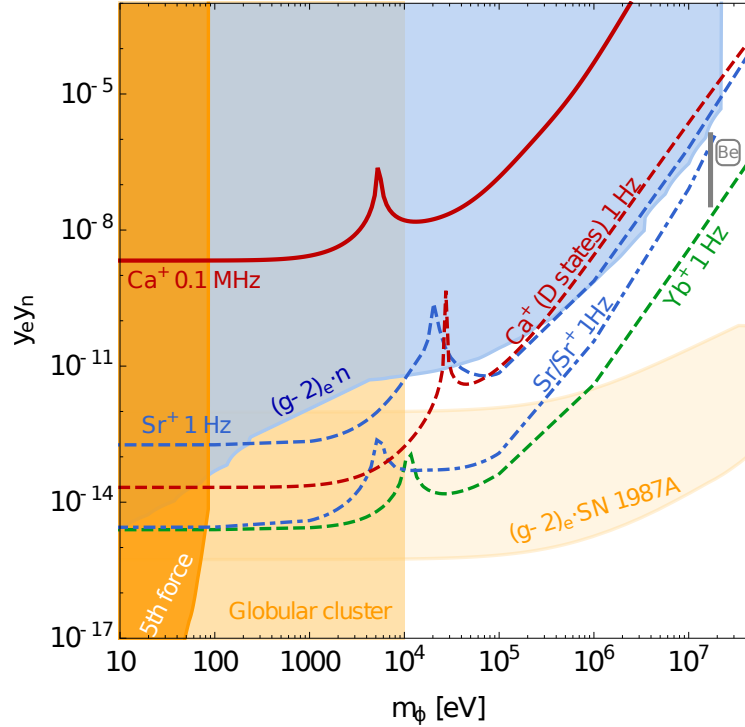


Figure 1.2: Example *exclusion plot* taken from ref. [47] showing limits on the electron and neutron couplings ($\gamma_e \gamma_n = 4\pi\alpha_{\text{NP}}/(-1)^s$) of a new boson of mass m_ϕ . The solid line shows a limit from actual IS data in calcium. The dashed lines show the prospects of possible limits achieved given the annotated precision of IS spectroscopy in the given system. The shaded areas are constraints from other sources than IS spectroscopy. For more details see [47].

iment design and construction) of the high-precision Penning-trap mass spectrometer PENTATRAP (in its current state), the systematic shifts that need to be considered, and also to provide most of the software for simulation and data analysis used. The mass and mass-ratio measurements presented are in that respect perfect examples, since combined they require to discuss and characterize nearly every known systematic effect for mass determinations in our Penning traps.

This thesis starts in Chapter 2 with a description of the theory behind Penning-trap mass spectrometry, the systematic effects involved and limitations, the detection system, and measurement techniques. This is followed in Chapters 3 and 4 by an overview of the setup and a description of the data analysis.

The next sections (Chapters 5 and 6) will describe the measurements made: (i) The mass of ^{20}Ne measured against ^{12}C , resulting in a precise mass in atomic mass units that has been used for stringent tests of bound-state QED. (ii) The four mass ratios of stable even ytterbium isotopes relative to ^{172}Yb . (iii) And finally, the binding energy determinations of the valence electron of Yb^{41+} and Yb^{42+} .

The thesis is concluded in Chapter 7 with a summary of the results and their impact, as well as some prospects of future measurements and an improved modified setup.

Chapter 2

Penning Trap Theory

Considering different ion trapping methods, Penning traps [54] are, in regard to the basic physics behind them, one of the most simple storage devices for charged particles. With a strong static magnetic field and a superimposed weak electrostatic field, ions can be stored on stable motional modes. The description of the Penning trap, particle motion, frequency shifts, different geometries, and detection principles have been discussed in many papers, review articles, books, and theses. For some nice general reference books, I would recommend [55, 56] and the original *geonium theory* paper [57]. Still, this chapter will give an overview of the theory of storing charged particles in a Penning trap and nondestructive measurement methods for the determination of its eigenfrequencies. This summary is not at all to improve on the mentioned existing literature, but with the goal of providing the necessary theory in a consistent notation within this thesis and to occasionally link the given theory with examples within the parameters of our experiment.

The chapter will begin with a brief introduction to the theory of charged particles in a Penning trap in section 2.1 and the connection to high-precision mass spectrometry section 2.2. This is then followed by descriptions of common Penning trap imperfections and their resulting frequency shifts in section 2.3. Furthermore, the description on how to drive and couple eigenmodes as well as the fundamental principles of the detection systems used for nondestructive measurements are given in section 2.4 and section 2.5.

2.1 The ideal Penning trap

A strong homogeneous magnetic field

$$B(\rho, z) = B_0 \hat{z} \quad (2.1)$$

confines an impulse carrying charged particle on a circular motion (Figure 2.1) due to the inward facing Lorentz force $\vec{F} = q(\vec{v} \times \vec{B})$ and the counteracting centripetal force $\vec{F} = \frac{m\vec{v}^2}{r}$. Depending on the charge, mass and magnetic field strength, the particle performs the *free cyclotron motion* with a radial frequency:

$$\omega_c = \frac{q}{m} B, \quad (2.2)$$

where $q = N \cdot e$ is the charge of the particle in multiples of the elementary charge e and m is its mass. This relation shows already how a measured cyclotron frequency can be used to determine the mass of a charged particle, but more on that in section 2.2.

In order to confine the charged particle also in the direction parallel to the magnetic field lines, a weak quadrupolar electrostatic potential is superimposed:

$$\phi(x, y, z) = c_2 U_0 \left(z^2 - \frac{x^2 + y^2}{2} \right) = c_2 U_0 \left(z^2 - \frac{\rho^2}{2} \right), \quad (2.3)$$

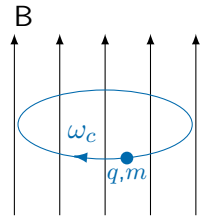


Figure 2.1: Cyclotron motion in a homogeneous magnetic field.

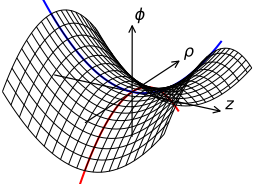


Figure 2.2: Quadrupolar electrostatic trapping potential in cylindrical coordinates. The blue curve in the z direction and the red curve in the ρ direction emphasize the confining and divergent nature of the potential.

where U_0 is the voltage applied between suitable trap electrodes, ρ, z are cylindrical coordinates, and c_2^1 is a coefficient that reflects the strength of the potential for a given electrode geometry. As shown in Figure 2.2 the potential is confining in the axial direction but repelling in the radial direction. The combination with the radial confinement resulting from the magnetic field results in a modified radial movement, explained below. This combination of static fields is the basic definition of a Penning trap. The derivation of this quadrupolar potential, which is based on a stable solution of the Laplace equation, is described in [61, 62].

The canonical way to create such a quadrupolar potential is a hyperbolic electrode geometry [54, 63] that mimes the equipotential surfaces of equation (2.3). This trap geometry is mostly considered deprecated in the context of precision experiments and replaced by open-endcap cylindrical Penning traps because of simpler manufacturing and easier access for ion beams or lasers. An introduction to this design and details on how to calculate the trap potentials expansion coefficients c_i are given in [60, 64] and explicitly for our trap geometry in [58, 59]. The frequency shifts due to nonzero higher-order c_i coefficients are described in section 2.3, here only the ideal case with $c_i = 0 \forall i \neq 2$ is considered.

Using the potential from (2.3) the electric field can be derived

$$\vec{E}(x, y, z) = -\nabla\phi(x, y, z) = c_2U_0(x\hat{x} + y\hat{y} - 2z\hat{z}). \quad (2.4)$$

With the electric field included, the Lorentz force on the trapped particle is given by:

$$\vec{F} = q(\vec{E} + \dot{\vec{r}} \times \vec{B}) = m\ddot{\vec{r}} \quad (2.5)$$

$$\Rightarrow qc_2U_0 \begin{pmatrix} x \\ y \\ -2z \end{pmatrix} + qB \begin{pmatrix} \dot{y} \\ -\dot{x} \\ 0 \end{pmatrix} = m \begin{pmatrix} \ddot{x} \\ \ddot{y} \\ \ddot{z} \end{pmatrix}. \quad (2.6)$$

The ordinary differential equation in the z component (axial direction) can be solved with the typical ansatz for a harmonic oscillator:

$$z(t) = z_0 \cos(\omega_z t + \phi_z), \quad (2.7)$$

where z_0 is the amplitude and ω_z is the axial eigenfrequency of the oscillator, see Figure 2.3. By differentiation and coefficients equating the relation for the axial eigenfrequency of the trapped particle is extracted:

$$\omega_z = \sqrt{\frac{2qc_2U_0}{m}}. \quad (2.8)$$

The axial frequency is independent on the magnetic field B but directly dependent on the applied trapping voltage U_0 . This voltage dependence can be used in the experiment to tune the axial frequency on resonance with the detection system².

Being a simple harmonic oscillator, the maximal potential energy of the axial mode is given by $E_z = q\phi(z) = qc_2U_0z_0^2$ and is equal to the maximal kinetic energy $E_z =$

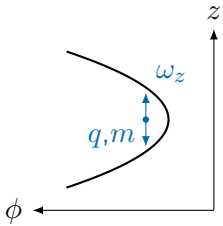


Figure 2.3: Axial movement in the quadratic trapping potential in z -direction.

¹The c_i parameters, with lower case letter, used in this thesis are in compliance with the tower design paper and thesis of C. Roux [58, 59] and assimilate the often-used characteristic trap length d . The conversion from the unit-less parameter is $c_i = C_i/(2d^i)$, therefore having the units of $1/\text{mm}^i$. The definition of the characteristic length of an open-endcap cylindrical Penning trap is given in [60].

²Do not directly associate the potential depth with the change in axial frequency. Increasing the trapping voltage U_0 causes the potential to *squeeze* and this change in the effective quadratic dependency causes the axial frequency to change.

$\frac{1}{2}m(z_0\omega_z)^2$. With this, the energy-dependent axial amplitude can also be extracted:

$$z_0 = \sqrt{\frac{E_z}{qc_2U_0}} = \sqrt{\frac{2E_z}{\omega_z^2 m}}. \quad (2.9)$$

The equations of the radial motion can be extracted by transforming the coupled variables x and y to one complex variable:

$$u \mapsto x + iy. \quad (2.10)$$

This transformation simplifies equation (2.6) to:

$$m\ddot{u} = -iqB\dot{u} + qc_2U_0u \quad (2.11)$$

$$\Leftrightarrow \ddot{u} = -i\omega_c\dot{u} + \frac{1}{2}\omega_z^2u \quad (2.12)$$

$$\Rightarrow \omega^2 = \omega_c\omega - \frac{1}{2}\omega_z^2, \quad (2.13)$$

where in the last step the ansatz³ $u(t) = A \cdot \exp(-i\omega t)$ was used. Equation (2.13) is easily solved and reveal the frequencies of the radial eigenmotions:

$$\omega_{\pm} = \frac{\omega_c}{2} \pm \sqrt{\left(\frac{\omega_c}{2}\right)^2 - \frac{\omega_z^2}{2}} \quad (2.14)$$

$$= \frac{1}{2} \left(\omega_c \pm \sqrt{\omega_c^2 - 2\omega_z^2} \right). \quad (2.15)$$

Given these two solutions the radial motion is a superposition of two independent oscillations: the slower *magnetron motion* with frequency ω_- and the faster *cyclotron motion* with the trap modified cyclotron frequency ω_+ . The oscillation amplitudes are ρ_- and ρ_+ , respectively. The slower *magnetron motion* originates from the perpendicular electric and magnetic field as a $\vec{E} \times \vec{B}$ drift. Converting the exponential ansatz to trigonometric functions and transforming back to Cartesian coordinates results in the equations of motion in the xy -plane:

$$\begin{pmatrix} x(t) \\ y(t) \end{pmatrix} = \rho_+ \begin{pmatrix} \cos(\omega_+t + \phi_+) \\ -\sin(\omega_+t + \phi_+) \end{pmatrix} + \rho_- \begin{pmatrix} \cos(\omega_-t + \phi_-) \\ -\sin(\omega_-t + \phi_-) \end{pmatrix}. \quad (2.16)$$

The resulting radial motion is plotted in Figure 2.4 and the full ion motion of a charged particle in a Penning trap is plotted in Figure 2.5. Requiring *real* solutions for the eigenfrequencies, two conditions follow from Equations (2.8) and (2.14):

$$qc_2U_0 > 0; \quad (2.17)$$

$$\omega_c^2 > 2\omega_z^2 \Rightarrow \frac{q}{m} \frac{B^2}{4} > c_2U_0. \quad (2.18)$$

The first stability condition reflects that for a positive charge q the product of c_2U_0 has to be a positive voltage barrier and vice versa. The second condition arises from the repulsive nature of the electrostatic potential in the radial direction, which has to be counteracted by the magnetic field. The motional frequencies are, in case of a typically strong magnetic field (like 7 T) and weak electric field (like a few 10 V), hierarchically ordered: $\omega_+ \gg \omega_z \gg \omega_-$.

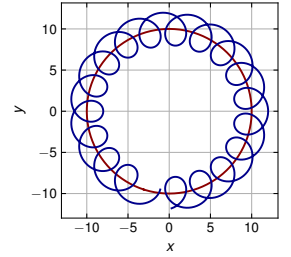


Figure 2.4: Radial ion motion in the xy -plane. The red curve shows the slow magnetron motion, and the blue curve includes the faster cyclotron motion. $\omega_+/\omega_- = 20$ and $\rho_+/\rho_- = 0.2$ for better visualization.

³The minus here seems arbitrary, but it defines in which direction your magnetic field is pointing, outward or inward of the x - y -plane (see Equation 2.16). As defined here, the magnetic field points up (towards you) from the shown plane for positively charged ions.

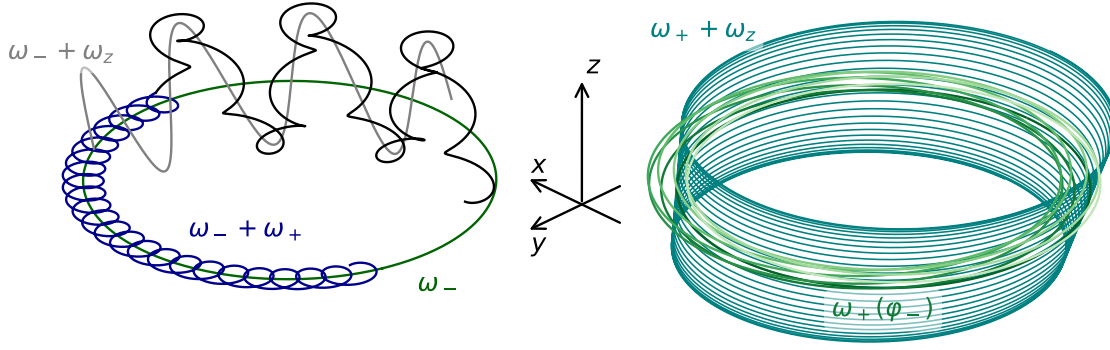


Figure 2.5: Illustration of the trajectory of a charged particle in an ideal Penning trap. The left trajectories show the ion motion with frequency ratios $\omega_+ = 5\omega_z = 50\omega_-$ and amplitude ratios $\rho_- = 2z = 10\rho_+$ for an intuitive visualization of the frequency hierarchy. The colored lines show single or combined eigenmotions, annotated with their respective eigenfrequency, and the black line shows the full ion motion, combining all eigenmotions. The right trajectories show the combined axial and cyclotron motion over half an axial period with frequency ratios $\omega_+ = 50\omega_z = 2500\omega_-$ and amplitude ratios $\rho_+ = 2z = 10\rho_-$, which better represent the actual conditions when conducting measurements at PENTATRAP. The effect of the small magnetron orbit in this case is depicted in the green cycles, showing the cyclotron orbit at different phases φ_- of the magnetron motion, resulting in a *wobbling* or eccentric motion around the trap center.

The following useful relations can be deduced from equation (2.15):

$$\omega_c = \omega_+ + \omega_- , \quad (2.19)$$

$$\omega_c^2 = \omega_+^2 + \omega_z^2 + \omega_-^2 , \quad (2.20)$$

$$\omega_z^2 = 2\omega_+\omega_- . \quad (2.21)$$

Using either equation (2.19) or (2.20), the free cyclotron frequency can be derived from the eigenfrequencies of an ion in the trap. While equation (2.19) holds only for ideal traps⁴, equation (2.20), called the *Brown-Gabrielse invariance theorem* [65], is more robust against misalignment of the trapping potential axis and magnetic field axis, and possible ellipticity of the electric potential, see subsection 2.3.4.

Given the strong frequency hierarchy $2\omega_z^2 \ll \omega_c^2$ and approximating using first-order Taylor series of $\sqrt{1-x} \approx (1 - \frac{x}{2})$ with $x \ll 1$, Equation (2.15) can be approximated:

$$\omega_+ \approx \omega_c - \frac{c_2 U_0}{B} \quad (2.22)$$

$$\omega_- \approx \frac{c_2 U_0}{B} . \quad (2.23)$$

This reveals that in *first-order* approximation the magnetron frequency is a function of only the static fields and independent of the charge and mass of the trapped particle.

⁴In case of online Penning-trap mass spectrometry experiments using ToF-ICR or PI-ICR measurement techniques this relation is also used as it allows to determine the mass ratio without measuring the axial frequency and is still accurate enough in respect to the lower measurement precision.

The total energy of a stored ion is given by the sum of energies in the individual eigenmotions [66, 67]:

$$E_z = \frac{m}{2} \omega_z^2 z_0^2 \quad (2.24)$$

$$E_+ = \frac{m}{2} \omega_+^2 \rho_+^2 - \frac{m}{2} \omega_+ \omega_- \rho_+^2 = \frac{m}{2} \rho_+^2 \omega_+ (\omega_+ - \omega_-) \quad (2.25)$$

$$E_- = \underbrace{\frac{m}{2} \omega_-^2 \rho_-^2}_{E_{kin}} - \underbrace{\frac{m}{2} \omega_+ \omega_- \rho_-^2}_{E_{pot}} = -\frac{m}{2} \rho_-^2 \omega_- (\omega_+ - \omega_-) . \quad (2.26)$$

The first terms are the respective kinetic energies and the second are the respective potential energies calculated via $E_{pot} = q\phi(\rho)$. Given the frequency hierarchy we see that the energy of the cyclotron mode is dominated by the kinetic energy, and the energy in the magnetron mode is dominated by the potential energy. This results also in the negative sign of the magnetron energy and consequently to a meta-stable behavior: With decreasing energy, the radius increases⁵.

To justify the fact that a classical treatment is sufficient, one can estimate some values in the quantum-mechanical picture of the three eigenmodes. Since the eigenmodes are (in the ideal trap) independent harmonic oscillators, the simple quantum mechanical description of the (spinless) particles sum of energies is:

$$E_{total} = \hbar\omega_+ \left(n_+ + \frac{1}{2} \right) + \hbar\omega_z \left(n_z + \frac{1}{2} \right) - \hbar\omega_- \left(n_- + \frac{1}{2} \right) , \quad (2.27)$$

with n_i being the corresponding quantum numbers for each eigenmode. A classical harmonic oscillator has the mean energy $\langle E \rangle = k_b T$, with the Boltzmann constant k_b and the temperature T . Given our cooling method, see section 2.5, the temperature of the axial mode is at least 4.2 K, which results in a mean energy of $E = 345 \mu\text{eV}$. Given equation (2.27) and an axial frequency of about $2\pi \cdot 500 \text{ kHz}$ one reaches a quantum number of $n_z \approx 170000$. Within section 2.5 it will also become clear that the mean quantum numbers are the same for all modes after sideband cooling of the radial modes. These high quantum numbers justify the validity of the classical treatment above.

2.2 Mass spectrometry with Penning traps

The state-of-the-art method for determining mass ratios, mass differences, or absolute masses in atomic mass units is the measurement of the ratio of the cyclotron frequencies of two ions [21, 22]. This ratio is beneficial because the magnetic field and the elementary charge⁶ drop out in first order:

$$R' = \frac{\omega_{c,B}}{\omega_{c,A}} = \frac{q_B e m'_A B(t_B)}{q_A e m'_B B(t_A)} = \frac{q_B m'_A}{q_A m'_B} \quad \text{for } B(t_A) = B(t_B) , \quad (2.28)$$

where m'_i is here explicitly marked being the *ion* mass and its charge given as multiples of the elementary charge $q_i \cdot e$. The frequency ratio as a unitless measurement result is always published to be able to recalculate the actual value of interest in the event

⁵This often leads to confusion when talking about cooling the magnetron motion: Cooling is normally associated with the reduction of the energy of an eigenmode, and this would result in the increase of the magnetron radius until the particle is lost due to interaction with the trap electrodes. This is not the case and a simplified explanation for this is that cooling will reduce the kinetic energy E_{kin} of the particle and consequently reduce the magnetron radius. That change in radius will result in a higher potential energy E_{pot} and since this is the dominant energy contribution, the total magnetron energy E_- will effectively increase when cooled.

⁶The elementary charge e would not contribute to the uncertainty budget even when not reduced in the equation, because it is an *exact* fundamental constant since the SI redefinition of 2019 [68].

that more precise reference masses or binding energies are available (see below). The requirement $B(t_A) = B(t_B)$ represents the stability of the magnetic field and is therefore an important parameter for precision mass measurements⁷. This is a time-dependent effect, relevant due to the sequential measurements, and will be discussed in chapter 4 about the data analysis. The frequency ratio is completely insensitive to a common proportionality factor on both frequencies, e. g. the *accuracy* of the frequency reference used to lock the measurement equipment (described in detail in the setup description in section 3.2.3). Furthermore, a correlated systematic offset of the two frequencies due to a common source has also reduced impact on the ratio, discussed at the end of this section.

In order to calculate the neutral atomic mass of one of the ions, one has to correct for the missing electron masses $q_i m_e$ and the binding energy E_i of these electrons:

$$\begin{aligned} m_A &= m'_A + q_A m_e - E_A = R' \frac{q_A}{q_B} m'_B + q_A m_e - E_A \\ &= \underbrace{R' \frac{q_A}{q_B}}_{\approx m_A/m_B} m_B + \underbrace{(1 - R') q_A m_e}_{\approx 4 \times 10^{-3}} + R' \frac{q_A}{q_B} E_B - E_A, \end{aligned} \quad (2.29)$$

where equation (2.28) was used to substitute m'_A . One is typically interested in the absolute mass expressed in atomic mass units, and therefore carbon is the preferred reference mass m_B with zero uncertainty as it defines the unit. When using another reference mass, its uncertainty will contribute with approximately the mass ratio as a prefaktor. The electron mass is currently known with a relative uncertainty of 3×10^{-11} [36] but its impact is reduced due to the prefaktor (which is approximately the given value for both measurements presented). The uncertainties of the binding energies enter directly, and this also includes the conversion factor from the unit eV/c^2 to atomic mass units, which itself currently has an uncertainty of 3×10^{-10} [36]⁸. Since the binding energies are much smaller than the determined mass and the conversion from eV to u can be applied on the even smaller difference, the uncertainty of the conversion factor will not have a significant impact. For the light masses investigated within this thesis, being $m(^{20}\text{Ne})$ and $m(^9\text{Be})$, the uncertainties of the binding energies are known to few meV from the literature [37] and therefore do not limit the mass determination.

Ultimately, the uncertainty budget for most determinations of light masses is dominated by statistical and systematic uncertainty of the measured cyclotron frequency ratio. For heavier masses, the determination of an absolute mass will often be limited by the uncertainties of the binding energies of the highly charged ions (even when precisely calculated from theory) or by the uncertainty of the heavier reference masses⁹, e.g. [74]. For a neutral mass ratio, equation (2.29) can obviously simply be divided by m_B . This is not relevant here for the physics cases, but useful for comparing with the values in the literature, e.g. the Atomic Mass Evaluation [75], and the measurement results of other experiments. For access to the AME database via python, the module (`fticr_toolkit/ame.py`) can be used, which also includes a copy of the NIST binding energy tables [37] to calculate precise ion masses.

⁷The effect of magnetic field stability can be strongly suppressed by using the two-ion-balance measurement technique [18, 69–71]. Although it may seem superior at first glance, it has its own restrictions and limitations with regard to possible measurement candidates and systematic effects.

⁸CODATA describes the connections in detail in the given reference and I highly recommend reading it. Essentially, the origin of the conversion factor and its uncertainty is the measurement of the fine structure constant [72, 73].

⁹Heavier reference masses can still be the better choice here due to systematic effects that depend on the difference in mass or charge to the ion of interest.

The determination of the ratio \hat{R} of the nuclear masses $\hat{m}_i = m_i - Z_i m_e + E_i^{0+ \rightarrow Z+}$ is done as follows:

$$\begin{aligned}\hat{R} &= \frac{\hat{m}_A}{\hat{m}_B} = \left[m'_A - (Z_A - q_A) m_e + E_A^{q+ \rightarrow Z+} \right] \hat{m}_B^{-1} \\ &= R' \frac{q_A}{q_B} + \left[R' \frac{q_A}{q_B} \left((Z_B - q_B) m_e - E_B^{q+ \rightarrow Z+} \right) - (Z_A - q_A) m_e + E_A^{q+ \rightarrow Z+} \right] \hat{m}_B^{-1} \\ &= R' \frac{q_A}{q_B} + \left[m_e \left(R' \frac{q_A}{q_B} (Z_B - q_B) - (Z_A - q_A) \right) - R' \frac{q_A}{q_B} E_B^{q+ \rightarrow Z+} + E_A^{q+ \rightarrow Z+} \right] \hat{m}_B^{-1}.\end{aligned}\quad (2.30)$$

For the ytterbium campaign, we can simplify this with $Z_A = Z_B$ and (for most measurements) $q_A = q_B$, resulting in:

$$\hat{R} = R' + \left[(R' - 1) \left(m_e (Z - q) - E_B^{q+ \rightarrow Z+} \right) - \Delta E_{B-A}^{q+ \rightarrow Z+} \right] \hat{m}_B^{-1}, \quad (2.31)$$

where $\Delta E_{A-B}^{q+ \rightarrow Z+}$ is the difference of the calculated total binding energies for the two ions. Since the literature values for the used highly charge ytterbium ions are not nearly precise enough, they are calculated from theory by the group of Zoltán Harman at the MPIK. The binding energy difference is, because of the atomic structure similarities of two isotopes of the same element, calculated with much higher precision than the individual total binding energies. Using the binding energy isotope shift value and the impact of other input parameters reduced, the nuclear ratio is also uncertainty-dominated by the measured cyclotron frequency ratio.

For the determination of the binding energies $\Delta E^{q_A+ \rightarrow q_B+}$ between different charge states, one measures ideally the cyclotron frequency ratio of ions of the same isotope in different charge states [11], which allows to extract the binding energy difference as follows:

$$\Delta E^{q_A+ \rightarrow q_B+} = \left(1 - R' \frac{q_A}{q_B} \right) (m_B - m_e q_B + E_B) - m_e (q_A - q_B). \quad (2.32)$$

For ytterbium mass ratios and binding energy determinations, it could be beneficial to choose *not* the same charge state or the same isotopes, in order to better match the charge-to-mass ratios of the two measured ions and reduce systematic effects. However, this in turn requires a higher precision in the binding energy differences between the picked charged states, or for the binding energy determination, a precise mass ratio of the involved isotopes. Using the same charge state allows one to choose the charge state based on a simpler atomic structure for easier calculation of binding energies, avoid charge states with predicted low-energy metastable electronically excited states [13] and maximize the charge state to the technical limit for higher cyclotron frequencies, resulting in higher relative measurement precision. Since the precision of the theoretical binding energies was not certain at the time the measurement campaign began, the same charge state was used.

Using the invariance theorem (2.20) the error propagation (neglecting correlation and assuming independent variables¹⁰) of the relative uncertainties of the measured

¹⁰Independent uncertainties of the determined eigenfrequencies are most likely if the measurement precision is limited by the measurement method, like for the magnetron frequency using the double dip technique, see section 2.5. On the other hand, for measurement fluctuations dominated by trapping field changes, for example, a correlation is highly probable, and most dominant in simultaneous measurements.

eigenfrequencies results in:

$$\underbrace{\frac{\delta\omega_c}{\omega_c}}_{\approx 1 \dots 5 \times 10^{-11}} = \left[\underbrace{\left(\frac{\omega_+^2}{\omega_c^2} \frac{\delta\omega_+}{\omega_+} \right)^2}_{\approx 1} + \underbrace{\left(\frac{\omega_z^2}{\omega_c^2} \frac{\delta\omega_z}{\omega_z} \right)^2}_{\approx 1 \dots 4 \times 10^{-4}} + \underbrace{\left(\frac{\omega_-^2}{\omega_c^2} \frac{\delta\omega_-}{\omega_-} \right)^2}_{\approx 1 \dots 10 \times 10^{-8}} \right]^{\frac{1}{2}}. \quad (2.33)$$

The number below on the left gives the aimed at shot-to-shot measurement precision, the *statistical* error of a single cyclotron frequency measurement. This precision enables us to reach a few 10^{-12} measurement uncertainty after averaging a few hundred single ratios, which typically takes one to two weeks. Details on this stability will be given in the data analysis section chapter 4. The numbers on the right show the approximate suppression factors for the measurement cases in this thesis. An increased charge state will increase ω_+ and reduce these suppression factors, since the axial frequency is fixed with the detection systems and the increased charge state will be compensated with a lower trapping voltage (which will further decrease ω_- and also its suppression factor). Given these numbers and the aimed at uncertainty, the relative uncertainty of the axial frequency measurement has to be better than 1×10^{-7} and for the magnetron frequency measurement better than 1×10^{-4} .

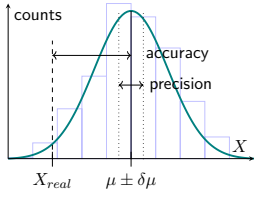


Figure 2.6: Statistical uncertainty (δ , *precision*) and systematic deviation (Δ , *accuracy*).

As these measurement uncertainties can be dominated by field fluctuations, it is important to realize that after applying the invariance theorem, in theory, the stability of the electric field no longer plays a role. The determined free cyclotron frequency is not a function of the trap voltage. This, on the other hand, means that the eigenfrequencies either have to be measured simultaneously or have to be corrected for possible temporal changes before applying the invariance theorem. It also shows that the electric field must be most stable in the time scale of the measurements performed before calculating the free cyclotron frequency. This will be discussed in detail in subsection 4.1.3.

The difference between statistical uncertainties and systematic deviations is the same as the difference between precision and accuracy, see Figure 2.6: The more often the measurement is performed, the more precise the mean value can be determined. Compared to this, systematic deviations do not average down. A respective shift stays constant as long as the experimental conditions involved do not change. The determination or rather estimation of a systematic shift is always done via theoretical models and the respective quantities of trapping conditions or other parameters that result in frequency shifts. The shifts themselves do not propagate with the quadratic sum as with statistical uncertainties. In case of the invariance theorem, the impact of shifts $\Delta\omega_i$ on the free cyclotron frequency is given by:

$$\frac{\Delta\omega_c}{\omega_c} = \frac{\omega_+^2}{\omega_c^2} \frac{\Delta\omega_+}{\omega_+} + \frac{\omega_z^2}{\omega_c^2} \frac{\Delta\omega_z}{\omega_z} + \frac{\omega_-^2}{\omega_c^2} \frac{\Delta\omega_-}{\omega_-}. \quad (2.34)$$

That being said, the estimation of the shifts is mostly based on measurement results, e. g. the determined trap parameters or motional amplitudes. Therefore, these parameters have statistical uncertainties themselves, which are propagated quadratically. The shifts of the cyclotron frequency or finally the cyclotron frequency ratio can be much higher than the statistical uncertainty, but the uncertainty of the estimated shifts must be on the order of the aimed at accuracy, in our case a few 10^{-12} . To our advantage, the uncertainties of systematic shifts can be smaller in the frequency ratio than in the individual frequency because of correlated parameters. This becomes clear when deriving

an expression for the ratio shift:

$$\begin{aligned}
 R'_{\text{ideal}} &= \frac{\omega_{c,B,\text{ideal}}}{\omega_{c,A,\text{ideal}}} = \frac{\omega_{c,B,\text{meas}} - \Delta\omega_{c,B}}{\omega_{c,A,\text{meas}} - \Delta\omega_{c,A}} \\
 &= \frac{R'_{\text{meas}}\omega_{c,A,\text{meas}} - \Delta\omega_{c,B} + R'_{\text{meas}}\Delta\omega_{c,A} - R'_{\text{meas}}\Delta\omega_{c,A}}{\omega_{c,A,\text{meas}} - \Delta\omega_{c,A}} \\
 &= R'_{\text{meas}} - \frac{\Delta\omega_{c,B} - R'_{\text{meas}}\Delta\omega_{c,A}}{\omega_{c,A,\text{meas}} - \Delta\omega_{c,A}} = R'_{\text{meas}} - \Delta R'.
 \end{aligned} \tag{2.35}$$

Expanding the first numerator part of $\Delta R'$ with $\omega_{c,B}$ and approximating in the second numerator $R'_{\text{meas}} \approx R'_{\text{ideal}}$, which can be justified given $\Delta R \cdot \Delta\omega_{c,A}/\omega_{c,A} \ll 10^{-12}$, this can be simplified to:

$$\Delta R' \approx R'_{\text{meas}} \left[\frac{\Delta\omega_{c,B}}{\omega_{c,B}} - \frac{\Delta\omega_{c,A}}{\omega_{c,A}} \right]. \tag{2.36}$$

The frequency shifts are typically depended on the ions motional amplitudes, eigenfrequencies and one or more trap specific parameters. If such a trap parameter is common for both ions, it can be extracted from the subtraction, and its uncertainty contribution is reduced by the difference of the remaining terms.

Still, the requirements on the frequency determination are quite high: With cyclotron frequencies of 10 60 MHz, the statistical precision of the averaged frequency-ratio measurement, as well as the accuracy of the mean absolute frequency ratio, must be on the order of 10 μ Hz to 60 μ Hz for a measurement goal of 1×10^{-12} relative uncertainty.

2.3 The real Penning trap

In this section, the *real* systematic frequency shifts due to field imperfections and other sources are discussed. With real frequency shift, I mean that these shifts are real disturbances of the actual oscillation frequencies of the trapped ion, compared to possible systematic measurement errors originating in the detection system or analysis¹¹. The expressions of the frequency shifts are mostly taken from other sources as referenced and not derived from scratch in this thesis. The *real* Penning trap discussed here is PENTATRAP's five-pole cylindrical open-endcap Penning trap as shown in Figure 2.7.

All shifts $\Delta\omega_i$ are given as deviations from the eigenfrequencies in an ideal Penning trap, i. e.:

$$\omega_{i,\text{meas}} = \omega_{i,\text{ideal}} + \Delta\omega_i. \tag{2.37}$$

The correction of a measured eigenfrequency to the ideal one is therefore made by subtracting a calculated systematic shift. The cyclotron frequency ratio needs to be calculated from the ideal frequencies, and therefore all systematic frequency shifts have to be estimated to either correct the measured frequency or, more beneficially, correct the determined cyclotron frequency ratio. The impact of these shifts on the determined cyclotron frequency ratio R_{cf} will be discussed in section 4.1.

During this section, remember that nearly all the parameters used to calculate these shifts must be determined experimentally. This is done mostly by varying one parameter, measuring the resulting relative shifts, and fitting the respective theoretical model to extract another parameter. Except for one (the image charge shift), all of these shifts are dependent on the motional amplitudes, and this will be the handle to probe the



Figure 2.7: Rendering of PENTATRAP's five-pole Penning trap with gold-plated copper electrodes and sapphire rings as high-impedance spacers between electrodes.

¹¹This is mainly the nonlinear phase transfer function, the dip lineshape error and calculated instead of measured magnetron or axial frequencies.

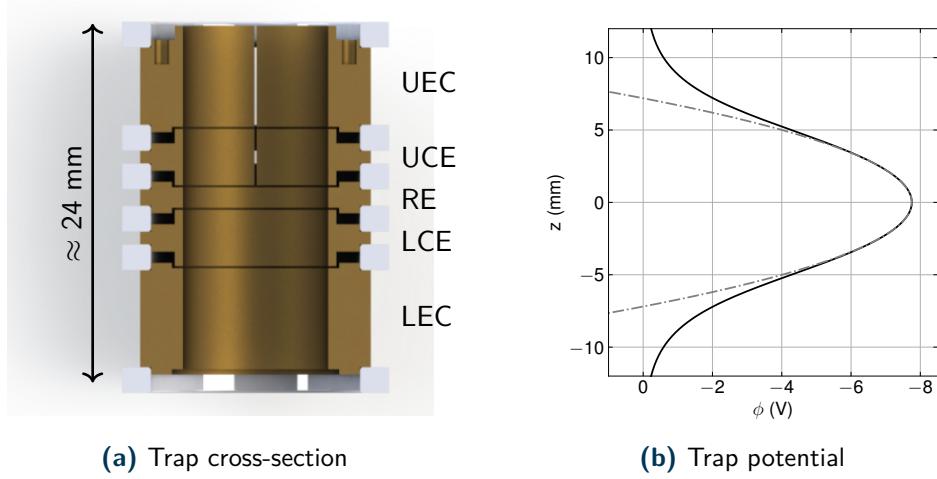


Figure 2.8: (a) Sectional view of PENTATRAP’s cylindrical open-end-cap Penning trap consisting of five electrodes: upper and lower end cap (UEC/LEC), upper and lower correction electrodes (UCE/LCE) and the central ring electrode (RE). In the current setup, one of the end caps and one of the correction electrodes are split in half for efficient creation of quadrupol RF fields. The effective trap voltage U_0 is the difference between the potential of the ring electrode and the end caps. The correction electrodes are supplied with a potential in between, optimized to reduce anharmonicities. (b) Resulting potential with a trap voltage of $U_0 = 10$ V and optimal correction electrode voltages (by numerical optimization of the calculated potential). The dashed gray line is a fit of a second order polynomial around the center position.

individual pre-factors. The experimental details will be given in the chapter on data analysis and characterization chapter 4.

2.3.1 Electrostatic field imperfections

In addition to the desired electrostatic quadrupole potential given in equation (2.3), higher-order electrostatic anharmonicities c_i with $i \neq 2$ are generally present. Using the rotational symmetry and axial mirror symmetry of the trap, the electrostatic potential can be expressed as a Taylor expansion near the trap center $z = 0$, which is explained in detail in [62, 76], resulting in the following series with only the even-order coefficients for now:

$$\begin{aligned}
 \phi(\rho, z)/U_0 = & c_0 + c_2 \left(z^2 - \frac{1}{2}\rho^2 \right) \\
 & + c_4 \left(z^4 - 3\rho^2 z^2 + \frac{3}{8}\rho^4 \right) \\
 & + c_6 \left(z^6 - \frac{15}{2}\rho^2 z^4 + \frac{45}{8}\rho^4 z^2 + \frac{5}{16}\rho^6 \right) \\
 & + \dots
 \end{aligned} \tag{2.38}$$

With U_0 being the voltage difference between the end-cap electrodes (UEC/LEC) and the central ring electrode (RE), see Figure 2.8. The depth of the potential is dominated by the applied voltage U_0 and the geometry defined c_2 . The next higher-order symmetric shape around the minimum, defined by c_4 and c_6 , is dominated by the voltage applied on the correction electrodes (UCE/LCE). Since the trap structure is mirror-symmetric to the radial plane at $z = 0$, voltages on the endcaps and correction electrodes are usually also applied symmetrically.

As mentioned in section 2.1, the cylindrical Penning trap has the advantage over the hyperbolic trap due to its simpler construction (manufacturing and assembly), as well as

easier ion loading and transport between adjacent traps. For a nearly ideal hyperbolic potential, symmetric voltages on the correction electrodes of a five-pole cylindrical Penning trap are used to tune the higher-order even coefficients of the central potential, ideally minimizing them for the best measurement conditions¹². The *tuning ratio* $\text{TR} = U_{ce}/U_0$ is the common term for the ratio of applied voltages on the correction electrodes and the ring electrode. The even potential coefficients in relation to the tuning ratio are (near the optimal tuning ratio) defined by:

$$c_i = d_i \text{TR} + e_i. \quad (2.39)$$

Minimizing both higher order even trap coefficients, the c_4 and c_6 terms, at the same time is possible by optimization of the trap geometry: With the right combination of trap radius and electrode lengths, it is possible to find a geometry with a tuning ratio where $c_4 = 0$ and at the same time have a near-zero c_6 . A trap that meets this condition is often referred to as *compensated*. Furthermore, the objective is to minimize d_2 , which means that a change in the tuning ratio does not affect the c_2 parameter. This condition is often referred to as an *orthogonal* trap design. The trap design of PENTATRAP and the geometric optimization involved, e. g. the trap radius, the electrode lengths, and the gap sizes are described in the thesis of C. Roux [59], and some of the resulting design parameters of our trap are also given in section 3.2.2.

The anharmonicities of the trapping potential described by $c_i, i \in [4, 6, \dots]$ will cause amplitude dependent frequency shifts on the eigenmotions [77]:

$$\begin{aligned} \frac{\Delta\omega_z}{\omega_z} = & \frac{3}{4} \frac{c_4}{c_2} (z_0^2 - 2\rho_+^2 - 2\rho_-^2) \\ & + \frac{15}{16} \frac{c_6}{c_2} (z_0^4 + 3\rho_+^4 + 3\rho_-^4 - 6\rho_+^2 z_0^2 - 6\rho_-^2 z_0^2 + 12\rho_+^2 \rho_-^2). \end{aligned} \quad (2.40)$$

$$\begin{aligned} \frac{\Delta\omega_{\pm}}{\omega_{\pm}} = & \mp \frac{3}{2} \frac{c_4}{c_2} \frac{\omega_{\mp}}{\omega_+ - \omega_-} (2z_0^2 - \rho_{\pm}^2 - 2\rho_{\mp}^2) \\ & \mp \frac{15}{8} \frac{c_6}{c_2} \frac{\omega_{\mp}}{\omega_+ - \omega_-} (3z_0^4 + \rho_{\pm}^4 + 3\rho_{\mp}^4 - 6\rho_{\pm}^2 z_0^2 - 12\rho_{\mp}^2 z_0^2 + 6\rho_{\pm}^2 \rho_{\mp}^2). \end{aligned} \quad (2.41)$$

The process of minimizing anharmonicities for a measurement campaign with the applied correction electrode voltages is described in subsection 4.2.1.

Odd c_i terms can appear due to geometric errors that break the mirror symmetry and in the presence of patch potentials on the trap electrodes. A linear potential gradient c_1 would result in an additional force on the charged particle, effectively changing the minimum of the potential to [62]:

$$\Delta z = -\frac{c_1}{2c_2}. \quad (2.42)$$

Despite the fact that a non-zero c_1 does not cause any direct frequency shift, it is still not negligible: The parameter c_1 is generally dependent on the trap depth (e. g. static patch potentials have less impact on a deeper trap and vice versa) and thereby cause a trap-depth-dependent axial position shift. This can be relevant for cyclotron frequency ratio measurements in where the trap voltage is different for the two ions to match the detection system resonance. Such change in U_0 will cause different axial positions and possibly different magnetic field strengths probed by the particle.

One should be cautious when calculating (or simulating for that matter) the higher order coefficients in the presence of a c_1 to perform a series expansion (or shift the z-axis) around the new minimum position of the potential to get the effective coefficients

¹²Also hyperbolic traps often have correction electrodes for the exact same purpose.

c_i for the trapped particle. From the perspective of the trapped particle, c_1 is always zero.

The next odd-order c_3 parameter will cause both: A position shift and a direct frequency shift, the derivation of these shifts is well described in ref. [78]:

$$\Delta z = \frac{3}{4} \frac{c_3}{c_2} \left(-z^2 + \rho_-^2 + \rho_+^2 \right) \quad (2.43)$$

$$\frac{\Delta \omega_z}{\omega_z} = -\frac{c_3^2}{16c_2^2} \left(-15z^2 + 18 \left(\rho_-^2 + \rho_+^2 \right) \right) \quad (2.44)$$

The axial frequency shift caused by c_3 is proportional, like the shift for c_4 , to ρ_{\pm}^2 . This is problematic for the standard method to optimize the tuning ratio, and will be discussed in subsection 4.2.1. The parameter c_3 is also considered to depend on the depth of the trap, such as c_1 .

There is an additional shift of the axial frequency which is proportional to $c_1 \times c_3$, but is actually a change in the effective c_2 seen by the ion, see reference [79]. This *shift* is typically very dominant in the axial frequency and can also be used to measure the product of $c_1 \times c_3$ and estimate the size of patch potentials or to minimize c_3 . However, while the frequency shifts and position shifts described so far are causing subsequent systematic shifts on ω_c , a modified c_2 does not result in a modified ω_c , meaning that this shift does not have to be corrected in the final values. Shifts due to higher-order odd and even coefficients are considered negligible.

2.3.2 Magnetic field imperfections

The magnetic field also shows inhomogeneous terms that may stem from magnetic materials inside or near the magnet or an imperfect magnet shimming. Similar to the series expansion of the electric field the same is done for the magnetic field [77]:

$$\begin{aligned} \vec{B}(\rho, z) = & B_0 \vec{e}_z + B_1 \left(z \vec{e}_z - \frac{1}{2} \rho \vec{e}_\rho \right) \\ & + B_2 \left(\left(z^2 - \frac{1}{2} \rho^2 \right) \vec{e}_z - z \rho \vec{e}_\rho \right) \\ & + \dots \end{aligned} \quad (2.45)$$

When averaged over the full motional path of an ion, the contribution of the linear field dependency B_1 term cancels out in first order [62]. Still, this linear gradient can cause a change of the eigenfrequencies due to the interaction with the magnetic moment of the trapped particle. A charged particle on a circular motion has a magnetic moment perpendicular to its motion, see Figure 2.9. The two radial eigenmotions therefore have a magnetic moment in the direction of the magnetic field [62]

$$\mu_{z\pm} = -\frac{q}{2} \omega_{\pm} \rho_{\pm}^2. \quad (2.46)$$

In combination with a linear magnetic field gradient, a magnetic moment causes an additional force on the trapped ion in axial direction

$$F_z = \mu_z \frac{\partial B_z}{\partial z} = \mu_z B_1, \quad (2.47)$$

which will shift the axial equilibrium position [62, 78]:

$$\Delta z = -\frac{B_1}{2B_0} \frac{\omega_c}{\omega_z^2} \left(\omega_+ \rho_+^2 + \omega_- \rho_-^2 \right). \quad (2.48)$$

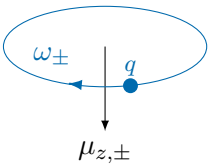


Figure 2.9: Magnetic moment perpendicular to the circular motion of trapped ion.

This position shift and the B_1 itself cause a change of the effective magnetic field probed of $\Delta z B_1$. This is no systematic shift for a single ion, since just like the change in equilibrium position due to c_1 , the eigenfrequencies are correct with respect to that new position. The shift on the free cyclotron frequency can still be defined as

$$\frac{\Delta\omega_c}{\omega_c} \approx -\frac{B_1^2 \omega_+}{B_0^2 \omega_z^2} (\omega_+ \rho_+^2 + \omega_- \rho_-^2) \approx -\frac{B_1^2 \omega_+^2 \rho_+^2}{B_0^2 \omega_z^2}, \quad (2.49)$$

and is mostly relevant for characterization measurements in our case. The magnetic field gradient has been measured at PENTATRAN several times, e. g. [79], and so far complied with $B_1 = 1.4(3) \mu\text{T mm}^{-1}$ and $+1.5(2) \mu\text{T mm}^{-1}$ for traps 2 and 3, respectively, even after modification of the setup and reinsertion in the magnets' bore. This B_1^2 shift estimated using (high) typical values of $\nu_c = 54 \text{ MHz}$, $\rho_+ = 100 \mu\text{m}$ and $\nu_z = 600 \text{ kHz}$, results in a relative cyclotron frequency shift of the order of 1×10^{-12} .

The shift in the ratio however, see Equation 2.36, is not sensitive to the absolute Δz , but to the difference:

$$\begin{aligned} \Delta R' &\approx R'_{\text{meas}} \left[\frac{\Delta\omega_{c,B}}{\omega_{c,B}} - \frac{\Delta\omega_{c,A}}{\omega_{c,A}} \right] \\ &= R'_{\text{meas}} \left[\frac{B_1 \omega_{+,A} \rho_{+,A}}{B_0 \omega_{z,A}} \right]^2 \left[1 - \left(\frac{\omega_{z,B} R'_{\text{meas}} \rho_{+,B}}{\omega_{z,A} \rho_{+,A}} \right)^2 \right]. \end{aligned} \quad (2.50)$$

Note that the first [...] is equal to the shift of the cyclotron frequency given in Equation 2.49. As long as the part (...) is $\approx 1.0(1)$ on a level of 10%, which is usually the case¹³, this systematic shift does not play a role in determining mass ratios and can be safely neglected for the measurements performed.

The shifts of the eigenfrequencies due to B_2 , also in combination with the magnetic moment $\mu_{z,\pm}$, are given by [77]

$$\frac{\Delta\omega_z}{\omega_z} = \frac{B_2}{4B_0} \frac{\omega_+ + \omega_-}{\omega_+ \omega_-} (\rho_-^2 \omega_- + \rho_+^2 \omega_+), \quad (2.51)$$

$$\frac{\Delta\omega_{\pm}}{\omega_{\pm}} = \pm \frac{B_2}{2B_0} \frac{\omega_+ + \omega_-}{\omega_+ - \omega_-} \left(z^2 - \rho_{\pm}^2 - \rho_{\mp}^2 \left[1 + \frac{\omega_{\mp}}{\omega_{\pm}} \right] \right). \quad (2.52)$$

Note here that the shift of the axial frequency is independent of the axial amplitude and that the magnetron amplitude has a much smaller effect than the cyclotron amplitude. Due to this, magnetron excitation is typically used for tuning ratio optimization.

The shift of the axial frequency due to B_2 in combination with the spin magnetic moment of an electron or the nucleus is used as a spin state detection method in Penning trap experiments determining electron or nuclear g -factors [34]. In these experiments, B_2 is deliberately increased to six orders of magnitude or more compared to our experiment, in order to create a measurable change in the axial frequency due to a performed spin-flip. This not directly part of this thesis, but to the motivations behind the Neon and Beryllium mass measurement.

2.3.3 Combined field imperfections

In addition to the effect of B_1^2 mentioned before, the shift of the axial equilibrium position Δz due to the electric field coefficient c_1 and c_3 must be treated in combination with the

¹³In the special case of extrapolation of measured ratios with different PnP excitation strengths to zero excitation, the radius ratio becomes the thermal radius ratio. For very different masses, this can easily be $\ll 1$. However, due to the typical thermal amplitudes in the radial direction of only a few $1 \mu\text{m}$, the relative shift of the cyclotron frequency is drastically reduced and therefore the shift is still insignificant.

magnetic field gradient B_1 . For the parameter c_1 , the shift of the cyclotron frequency is given by

$$\frac{\Delta\omega_c}{\omega_c} = -\frac{B_1 c_1}{2B_0 c_2}. \quad (2.53)$$

Since there is no dependence on any ion parameter, this shift is constant for all ions as long as none of the trapping field parameters change. Unfortunately, as mentioned before, the parameter c_1 does change when the trap voltage U_0 is adjusted (in order to match the ions axial frequency to the resonator frequency). This was a source of error in the past for PENTATRAN [11], and is also discussed later in the context of the neon mass measurement. In the future, and for most other measurements presented in this thesis, this whole shift will be circumvented by tuning the detection systems resonance instead, see section 3.2.2.

Due to the dependency on the motional amplitudes, this upgrade does not immediately resolve the issue for the axial displacement due to c_3 (Equation 2.43):

$$\frac{\Delta\omega_c}{\omega_c} \approx -\frac{3B_1 c_3}{4B_0 c_2} (-z^2 + \rho_-^2 + \rho_+^2), \quad (2.54)$$

This shift is especially important for measurements of ions with very different thermal amplitudes after cooling.

Additionally, as described in ref. [80], the force in axial direction due to B_1 and the magnetic moment cause a change of the equilibrium position of the ion or, in more detail, result in a modified effective potential. Performing a series expansion in the new equilibrium position reveals a modified c_2 , which effects the axial frequency [78]:

$$\frac{\Delta\omega_z}{\omega_z} = -\frac{3B_1 c_3 \omega_c}{4B_0 c_2 \omega_z^2} (\omega_+ \rho_+^2 + \omega_- \rho_-^2). \quad (2.55)$$

This again, like the change in c_2 due to the combination of $c_1 c_3$, does not effect the resulting ω_c .

Further higher order shifts due to imperfect trapping potentials are ignored in the opinion that they are not relevant on the given measurement precision.

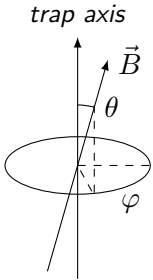


Figure 2.10: Misalignment of the static trapping fields.

2.3.4 Tilt, ellipticity and the invariance theorem

A tilt of the trap relative to the magnetic field, as shown in 2.10, shifts the ion's eigenfrequencies due to an inhomogeneous magnetic field probed by the ion. In addition, an ellipticity of the radial electrostatic potential, which can occur due to patch potentials on electrodes, can also induce shifts. The magnetic field in the coordinate system of the trap including the misalignment angles θ and ϕ and the potential including a harmonic distortion factor ϵ are given in first order by [81]:

$$\vec{B} = B \begin{pmatrix} \sin(\theta) \cos(\phi) \\ \sin(\theta) \sin(\phi) \\ \cos(\theta) \end{pmatrix} \text{ and} \quad (2.56)$$

$$\phi(x, y, z) = c_2 U_0 \left(z^2 - \frac{x^2 + y^2}{2} - \epsilon \frac{x^2 + y^2}{2} \right). \quad (2.57)$$

According to [65] the resulting frequency shifts will cancel each other in Equation 2.20 (*Brown-Gabrielse invariance theorem*), so the free cyclotron frequency can still be measured accurately:

$$\omega_c^2 = \bar{\omega}_+^2(\epsilon, \theta, \phi) + \bar{\omega}_z^2(\epsilon, \theta, \phi) + \bar{\omega}_-^2(\epsilon, \theta, \phi). \quad (2.58)$$

Since the simple side-band relation (Equation 2.19) for the determination of the cyclotron frequency is not invariant under these tilts and distortions, the difference to ω_c determined with the invariance theorem can be used to estimate the tilt angle θ and the ellipticity factor ϵ [82]:

$$\frac{9}{4}\theta^2 - \frac{1}{2}\epsilon^2 \approx \frac{\omega_- + \omega_+ - \omega_{c,inv}}{\omega_-}. \quad (2.59)$$

By assuming either zero tilt or zero ellipticity, the maximum values possible can be estimated. Typically, the ellipticity is assumed to be small from geometric considerations [83]. Since the system is radially symmetric, the angle ϕ should not alter the eigenfrequencies.

For some of the characterization measurements, it is still relevant to be aware of the individual frequency shifts originating from a tilt or ellipticity. For small imperfections $\theta \ll 1^\circ$ and $\epsilon \ll 1$, the following shifts occur [83]:

$$\frac{\Delta\omega_+}{\omega_+} = \frac{\omega_z^2}{\omega_+^2} \frac{3\theta^2}{4} \left(1 + \frac{\epsilon}{3} \cos 2\pi\right) + \frac{\omega_-^2}{\omega_+^2} \frac{\epsilon^2}{2} \quad (2.60)$$

$$\frac{\Delta\omega_z}{\omega_z} = -\frac{3\theta^2}{4} \left(1 + \frac{\epsilon}{3} \cos 2\pi\right) \quad (2.61)$$

$$\frac{\Delta\omega_-}{\omega_-} = \frac{3\theta^2}{4} \left(1 + \frac{\epsilon}{3} \cos 2\pi\right) + \frac{\epsilon^2}{2}. \quad (2.62)$$

Important to note here, is that the relative shift of the axial and magnetron motion do not depend on the charge-to-mass ratio of the ion. Subsequently, if two ions are stored at the same trapping potential, their magnetron frequencies are equal to the first-order approximation, see Equation 2.23, and therefore the absolute shifts will be approximately equal. This is important in the case of a precision comparison of magnetron frequencies of two ions ($\omega_{-,A} - \omega_{-,B}$) in order to measure the image charge shift, as it was done in ref. [84] and recently at PENTATRAP in ref. [85].

2.3.5 Relativistic shift

Due to the aimed at precision, even at comparably small velocities and energies, relativistic effects have to be considered as sources of shifts of the eigenfrequencies. This effect was studied in [77] and resulted in the following expressions for relative shifts on the respective eigenmotions:

$$\frac{\Delta\omega_{\pm}}{\omega_{\pm}} = \mp \frac{\omega_{\pm}}{\omega_+ - \omega_-} \frac{(\omega_{\pm}\rho_{\pm})^2 + 2(\omega_{\mp}\rho_{\mp})^2 + 0.5(\omega_z z)^2}{2c^2} \approx -\frac{\omega_+^2 \rho_+^2}{2c^2}. \quad (2.63)$$

$$\frac{\Delta\omega_z}{\omega_z} = -\frac{(\omega_+\rho_+)^2 + (\omega_-\rho_-)^2 + 0.75(\omega_z z)^2}{4c^2} \approx -\frac{\omega_+^2 \rho_+^2}{4c^2}. \quad (2.64)$$

The approximations are based on the strong frequency hierarchy and typical motional amplitudes¹⁴. The order of magnitude for the *relative* shift is the same for all eigenmotions. The relative shift in the trap-modified cyclotron frequency is even for a charge-to-mass ratio of $0.5 e u^{-1}$ and excitation radii of $\rho_+ = 100 \mu\text{m}$ *only* on the order of a few 10^{-10} (in our 7 T magnetic field). Such a relative shift on the axial frequency is negligible when applying the invariance theorem; see equation (2.34).

The relativistic shift is a prime example of a source of phase jitter in phase-sensitive measurement techniques (see section 2.5) to determine the trap-modified cyclotron mo-

¹⁴It might be surprising that the magnetron radius is not relevant, since it is in the same plain as the cyclotron motion. They are still independent motions and due to the low magnetron frequency this partial mass increase is insignificant. Visually, this is easy to spot in the right part of Figure 2.5.

tion of light highly charged ions. In this context, the *absolute* frequency shift (phase jitter) of ω_+ is approximately proportional to B_0^2 (using sideband cooling via the axial frequency $\sigma(\rho_{+,exc}) = \rho_{+,th}^2 \sim \omega_+^{-1}$), and the relative frequency shot-to-shot uncertainty increases linearly with B_0 . In high magnetic fields (like PENTATRAP) a high charge state might therefore not be beneficial for higher precision.

2.3.6 Image charge shift

An charged particle in a Penning trap produces image charges on the trap electrodes. These image charges are used to detect the ion's motional frequencies, see section 2.5, but they also generate an extra electric field. In our cylindrical traps, this phenomenon is mainly observed in the radial direction. As a positively charged ion moves radially, it induces negative image charges on the surfaces, resulting in an additional outward electrical force. This causes the modified cyclotron frequency to decrease and the magnetron frequency to increase by the same amount.

An analytical derivation of the resulting shifts on the radial modes in a cylindrical penning trap can be found in [84] and references therein (sign adjusted):

$$\Delta\omega_{\pm} = \mp \frac{q^2}{4\pi\epsilon_0 m \rho_0^3 \omega_c} = \mp \frac{q}{4\pi\epsilon_0 \rho_0^3 B_0}, \quad (2.65)$$

with ρ_0 and B_0 being the trap radius and absolute magnetic field strength, q and m the ions charge and mass and ϵ_0 the vacuum permittivity. With our trap radius of 5 mm and $B_0 \approx 7$ T the shift per charge is approximately $\Delta\nu_{\pm,ICS}/|q| = \mp 0.265$ mHz q^{-1} . This analytical solution is based on an infinitely long uniform hollow cylinder as a trap and therefore lacks the gaps between electrodes as well as electrode splittings. Also, the trap radius is prone to manufacturing errors, by design specification of individual electrodes already ± 5 μ m for PENTATRAP and additional deviations of the effective radius are possible after stacking the electrodes. However, this analytical relation has been experimentally verified with a precision of approximately 5% [84], which is sufficient for the mass and mass ratio determinations within this thesis. There is also no reason to assume higher than this mechanical errors. For some of PENTATRAP's future measurement campaigns, e. g. the determination of the mass of ^{87}Rb in atomic mass units, this shift has to be corrected with higher precision, and a method for the measurement of the effective trap radius is described in chapter 4.

For the determination of the free cyclotron frequency ω_c the image charge shift vanishes in the sideband relation (2.19) due to the opposite sign and equal amplitude. In the invariance theorem however, this shift does not vanish, but can be approximated: Since the shift size ($\Delta\nu_{\pm}$) is at most on the order of a few 10 mHz it can be estimated that the shift on the magnetron frequency in combination with the suppression factors in equation (2.33) will not be a significant contribution on the free cyclotron frequency (less than 1 ppt). Only considering the shift of the trap modified cyclotron frequency, the relative shift¹⁵ will be:

$$\frac{\Delta\omega_c}{\omega_c} \approx - \frac{q^2}{4\pi\epsilon_0 m \rho_0^3 \omega_c^2} = - \frac{m}{4\pi\epsilon_0 \rho_0^3 B_0^2}. \quad (2.66)$$

Within this approximation it becomes clear that the relative shift is actually not depended on the charge but on the mass of the ion. By inserting equation (2.66) into equation (2.36), the measured cyclotron frequency ratio will be shifted proportional to the mass

¹⁵Already anticipating confusion regarding the direction of this shift Ref. [62] not only has a detailed description of the origin of this effect but also explicitly states that the measured modified trap cyclotron frequency will always be smaller than the unaffected trap modified cyclotron frequency. This is then also true for the cyclotron frequency determined by the invariance theorem.

difference of the two ions investigated, $\Delta R' \sim m_A - m_B$. As an example: Given $R' = \omega_{c,B}/\omega_{c,A}$ and $m_A > m_B$ (e.g. m_B being a lighter reference mass), then the real (ideal) ratio is smaller than the measured one. In order to reduce this ratio shift (and the corresponding uncertainty), mass doublets are favorable, but also increasing the trap radius has significant impact, with the drawback of lower signal strength in the detection system. Inversely, for probing this effect and characterizing it to higher precision, a larger difference in masses is beneficial.

2.3.7 Image current shift

The image current shift is a shift of an eigenfrequency due to the interaction between the ion and another resonance. Although this is in most cases related to the interaction with the resonance circuit of the detection system, it can also be any other resonance connected to the measurement electrode. With respect to the most common origin in the interaction of the ion with the detection system, this shift is *automatically* corrected in the determination of the axial frequency by the dip-fit method (because it is essentially part of the fit model). Still, it makes sense to briefly discuss this *real* shift of the eigenfrequency within the description of the detection system, which is done in section 2.5.

2.4 Driving and coupling modes

The manipulation of eigenmotions is possible using resonant RF-signals (with frequency $\nu_{\text{rf}} = \omega_i/2/\pi$), coupled capacitively to suitable trap electrodes to superimpose dipolar or quadrupolar RF fields:

$$\vec{E}_z(t) = E_0 \sin(\omega_{\text{rf}}t + \varphi_{\text{rf}}) \hat{e}_i \stackrel{\text{e.g.}}{=} E_0 \sin(\omega_{\text{rf}}t + \varphi_{\text{rf}}) \begin{pmatrix} 0 \\ 0 \\ z \end{pmatrix} \quad (2.67)$$

$$\vec{E}_{xz}(t) = E_0 \sin(\omega_{\text{rf}}t + \varphi_{\text{rf}}) (r_i \hat{e}_j + r_j \hat{e}_i) \stackrel{\text{e.g.}}{=} E_0 \sin(\omega_{\text{rf}}t + \varphi_{\text{rf}}) \begin{pmatrix} z \\ 0 \\ x \end{pmatrix}. \quad (2.68)$$

For a dominantly dipolar RF field (Equation 2.67) in the direction of the axial motion (D_z), an end cap or correction electrode can be used. This is equivalent to a resonant drive of a harmonic oscillator, which amplitude evolution is depicted in Figure 2.11. The resonant drive of the motion will increase the amplitude and also imprint the phase of the drive on the motion¹⁶. The final amplitude after a resonant excitation over duration T depends on the initial amplitude z_0 , the strength of the excitation field at the position of the ion, which is proportional to the RF amplitude U_{exc} and a *transfer* constant κ_z , and the phase relation between the motion of the ion and the excitation $\Delta\phi$ [83]:

$$z_{\text{exc}}^2 = (\kappa_z T U_{\text{exc}})^2 + z_0^2 + (2\kappa_z T U_{\text{exc}} z_0 \cos(\Delta\phi + \phi_0)). \quad (2.69)$$

The κ_z factor is dependent on the respective effective electrode distance (here D_z), the charge-to-mass ratio q/m , but also inversely depended on ω_z^2 , resulting in no q/m dependence in first order [77]. This is also true for the radial dipole excitation.

¹⁶While the dipole excitation is the only one relevant for the presented measurements, the parametric excitation is worth mentioning, which can be realized by modulating the trap depth. This excitation will result in one of two phase values with a spacing of π and an increase in amplitude depending on the initial phase relation. In a phase space view, the projection on the phase axis decreases while the projection on the radius axis increases.

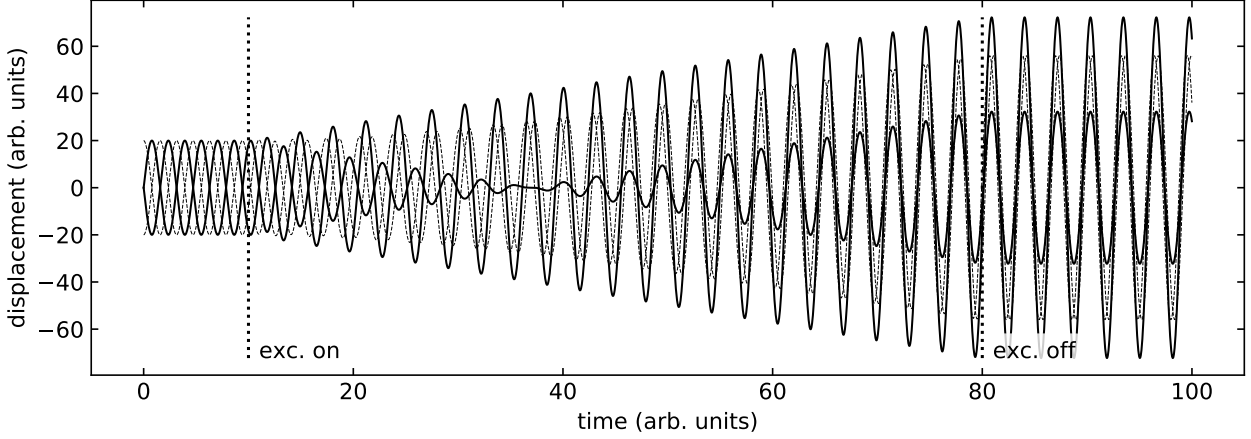


Figure 2.11: Simulation of the amplitude of an undamped harmonic oscillator under the influence of a resonant drive (e. g. resonant dipolar excitation of one of the eigenmotions). The initial phase of the oscillator is varied: The solid lines have an initial phase difference between the oscillator amplitude $z(t)$ and the excitation $E(t)$ of π and $-\pi$, while the dashed lines are 0 and 2π . The final amplitude depends on the initial phase difference between the oscillator and excitation, with the initial amplitude defining the spread of final amplitudes. While the final phase is set to the phase of the drive signal, a slight phase jitter is still present, which is reduced with increasing excitation amplitude (or reduced initial amplitude). The reason for this is more apparent in the description of the PnP method.

For a dominantly quadrupolar RF field (Q_{xz}), to couple the x (or y) and z direction (radial with axial), a half or quarter electrode is used. Split electrodes are often used for dipolar excitation in both the axial and radial directions as well because the respective field coefficients (D_z or D_x) are still sufficiently large for a reasonable excitation strength κ_z . Examining the example coupling field in Equation 2.68 reveals the coupling mechanism quite well: The field strength, and therefore the force on the charged particle, in the x direction depends on the amplitude in z and vice versa, equivalent to two pendulums coupled with a spring.

For a resonant coupling of eigenmotions, ω_{rf} has to be a frequency near the sum or the difference of two eigenfrequencies, i. e. the red or blue sideband of these frequencies. Such a quadrupolar RF-drive will transfer motional energy bi-directionally between the two coupled modes periodically, including the phase information. The conversion frequency is given by a modified Rabi-frequency [86, 87]:

$$\Omega = \sqrt{\Omega_0^2 + \delta^2}, \quad (2.70)$$

with the Rabi-frequency Ω_0 , which depends on the coupling strength and therefor on the amplitude of the applied RF signal, and the absolute detuning δ of the RF-signal from the true coupling frequency. Ω_0 is on the order a few 1 Hz to 10 Hz in our case.

To couple the axial motion with the magnetron motion, the upper (blue) sideband of the two frequencies ($\omega_{rf} = \omega_z + \omega_-$) has to be used, for coupling to the modified cyclotron motion the lower (red) sideband ($\omega_{rf} = \omega_+ - \omega_z$). Due to the coupling, the eigenfrequency of the axial mode will degenerate into two new eigenfrequencies:

$$\omega_{l,r} = \omega_z + \epsilon_{l,r} = \omega_z - \frac{1}{2} \left(\delta \pm \sqrt{4\Omega_0^2 + \delta^2} \right). \quad (2.71)$$

With vanishing detuning $\delta \rightarrow 0$, the splitting is symmetric around the former axial frequency $\pm\Omega_0$, and therefore a difference between the two frequencies of 2Ω . This splitting can be used (see the next section) to determine the radial frequencies and

prepare the π -pulse for the phase-sensitive frequency measurements of radial modes with the axial detection system.

2.5 Detection methods

All frequency measurements at PENTATRAP are performed with axial detection systems, which are also used to dampen / cool the motional amplitudes. Radial frequencies are determined and cooled indirectly via the sideband coupling described above. The following sections will give an overview of the principles and measurement techniques.

2.5.1 Axial detection system

The detection system is based on the non-destructive *Fourier-transform ion-cyclotron resonance technique* [88, 89]. A detailed description can be found in ref. [59].

This measurement method is based on image current detection, as sketched in Figure 2.12. An oscillating particle with charge q between two conducting plates (for simplicity of infinite size) creates image charges within the conductor and, given a suitable impedance is connected, an image current [90].

In case of our Penning trap this is also possible if a suitable electrode is used, and for an axial detection system, anything other than the central ring electrode can be used. The varying image charge creates an image current $I(t)$ and consequently a voltage drop $V(t)$ over the connected impedance $Z(\nu)$ to ground [57]:

$$I_{\text{ion}}(t) = \frac{q}{D_z} \dot{z}(t) = -\frac{q}{D_z} \omega_z z_0 \sin(\omega_z t), \quad (2.72)$$

where $z(t)$ is the position of the oscillating charged particle and D_z the effective electrode distance for a plate capacitor. As a reference: For an endcap of our trap, the effective electrode distance is $D_{z,\text{EC}} = 32.5$ mm and for a correction electrode $D_{z,\text{CE}} = 11.1$ mm [59]. A rough estimate for the correction electrode using $\omega_z \approx 2\pi \cdot 500$ kHz and $z_0 \approx 10$ μm results in an induced current of ≈ 0.5 fA per charge q .

Due to parasitic capacitance between trap electrodes and also cabling and other parts of the detection system, the induced radio frequency (RF) current would be short-circuited past a simple ohmic resistance. To avoid this, a high-quality superconducting coil is added instead, which results in a parallel LCR resonance circuit. A simplified sketch of the detection system is shown in Figure 2.13. The signal is amplified using a chain of cryogenic and room-temperature amplifiers and digitized with an analog-to-digital converter, more of which is given in section 3.2.2.

A perfect parallel LC circuit has an infinite resistance at the resonance frequency:

$$\nu_{LC} = \frac{1}{2\pi\sqrt{LC}}. \quad (2.73)$$

The resistance shown in the sketch is *caused* by resistive and dielectric losses and purely parasitic. The *effective* resistance at the resonance frequency can be determined experimentally by measuring the *quality factor* (Q -factor) of the resonance circuit:

$$R = 2\pi\nu_{LC}LQ \quad (2.74)$$

$$Q = \frac{\nu_{LC}}{\Delta\nu}, \quad (2.75)$$

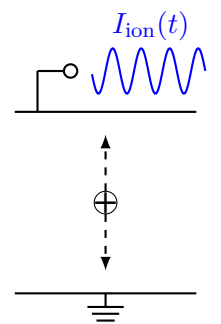


Figure 2.12: Image current induced by an oscillating charged particle.

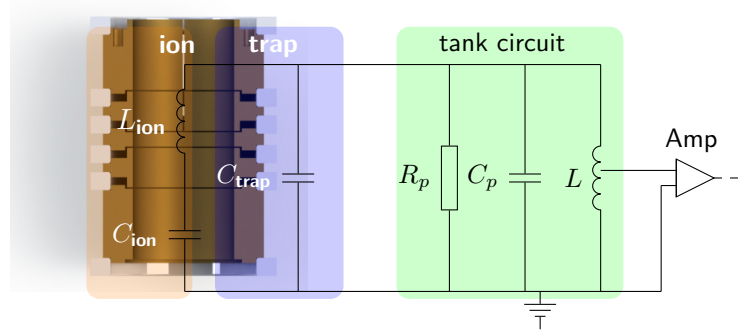


Figure 2.13: Sketch of the detection system for the axial motion of an ion in a Penning trap. The detection system consists of a high- Q resonant circuit (LCR or *tank circuit*) connected to the trap and a cryogenic amplifier. A hot ion (not shown here) would act as an AC current source, while a thermalized ion would act like a series LC circuit (sketched here) with low impedance at the ions axial frequency.

where $\Delta\nu$ is the resonance width at -3 dB below the maximum. The total impedance of the tank circuit is given by:

$$Z_{LC}(\nu) = \frac{1}{\frac{1}{R} + i\left(2\pi\nu C - \frac{1}{2\pi\nu L}\right)}. \quad (2.76)$$

The amplitude and phase response are given by the magnitude and angle of the complex impedance and plotted for an example resonator with $L = 3.5$ mH, $C = 30$ pF and $R = 130$ M Ω in Figure 2.14. The amplitude response will be visible using a spectrum analyser with sufficient amplification even at cryogenic temperatures due to the thermal (≥ 4.2 K¹⁷) current noise (Johnson-Nyquist noise) [91, 92] of the circuit creating a voltage drop over the impedance of the tank circuit. The root mean square (rms) voltage $u_{LC, th}$ of a bandwidth $\Delta\nu$ is given by:

$$u_{LC, th} = \sqrt{4k_b T_z \operatorname{Re}(Z_{LC}) \Delta\nu}. \quad (2.77)$$

The thermal phase response will not be only noise in a Fourier transform due to the fact that the phase of the thermal current noise is random and the response of the resonator will seem random as well. A phase-stable signal (such as the image current of an ion) will follow the theoretical phase response shown in Figure 2.14. Although this is rarely significant, an unstable resonance frequency of the detection system would cause the phase of a peak signal on the resonator to jitter. The size of the phase jitter in relation to the frequency jitter is demonstrated by the linear fit of the central region of the phase response of the resonator in Figure 2.14 and depends on the Q -value of the resonator.

As mentioned above, the induced image current of a trapped *hot* ion with large axial amplitude creates a detectable voltage drop if its axial frequency is close to the resonance of the detection circuit. If the amplitude of the induced current signal is exceeding the thermal noise level, it shows as a peak on top of the noise of the resonator. By varying the trap voltage, the axial frequency can be tuned (see Equation 2.8) to the resonance frequency of the tank circuit. In resonance, the voltage response of the resonator on the induced image current will feedback on the electrode and damp the ions' axial motion.

¹⁷The detection circuit is like the rest of the Penning-trap setup submerged in liquid helium. The temperature of the setup is near the boiling point of helium, but due to heat flow via the beamline and cabling, the temperature can be a few Kelvin higher. In addition, the effective temperature of the resonator can be higher due to unintentional positive feedback from the connected amplifier.

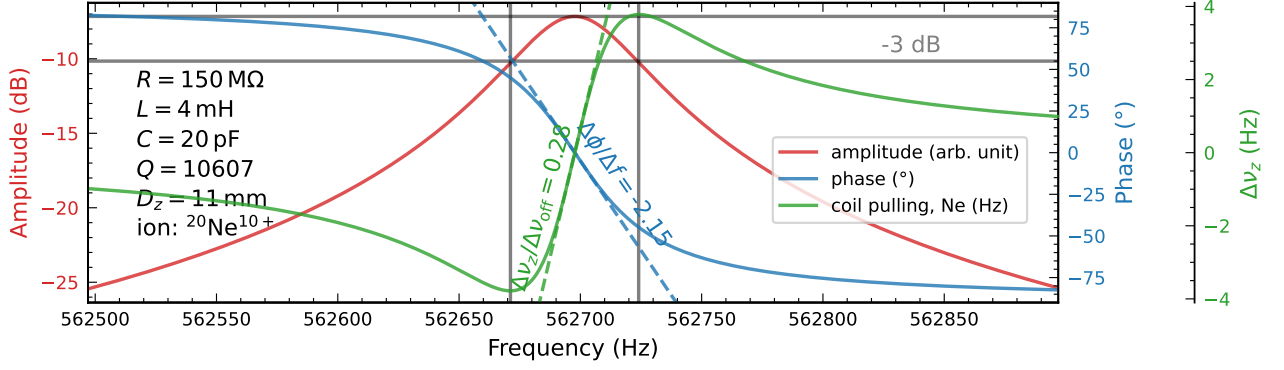


Figure 2.14: Calculated amplitude and phase response of an RLC circuit with the given parameters in decibel, comparable to a sweep measurement with a vector analyzer. Near the resonance frequency, the slope of the phase response is fitted with a linear function, demonstrating a possible source of phase jitter. In addition, the corresponding image current shift (coil pulling) for a $^{20}\text{Ne}^{10+}$ ion caused by the interaction with this resonator is plotted. More details in the text.

This damping force is given by [59]:

$$F_{\text{damp}} = \frac{q}{D_z} \text{Re}(Z_{LC}) I_{\text{ion}}. \quad (2.78)$$

Adding this force to Equation 2.5, the damping constant γ and an axial frequency shift can be determined [83]:

$$\gamma = \frac{q^2 \text{Re}(Z_{LC})}{2mD_z^2} = \frac{1}{2\tau}, \quad (2.79)$$

$$\Delta\omega_z \approx -\frac{q^2 \text{Im}(Z_{LC})}{2mD_z^2}, \quad (2.80)$$

where τ is the cooling time constant of the exponential decay of the ions energy loss. At resonance, the damping is maximal and the cooling time is minimal with $\text{Re}(Z_{LC})(\omega_{\text{res}}) = R$. The frequency shift is termed the *image current shift*¹⁸. The image current shift vanishes for $\omega_z = \omega_{\text{res}}$, and a visualization of this shift is given in Figure 2.14.

This *resistive cooling* is the only method of direct motional cooling in our experiment, and is limited by the thermal noise current of the detection system. When the ion reaches thermal equilibrium with the detection circuit, the Johnson-Nyquist noise keeps the ion at the temperature of the detection circuit. Since this thermal energy is then dissipated into the axial motion of the ion, which now effectively acts as a series LC circuit [93] as shown in Figure 2.13, with a low-impedance resonance at the axial frequency of the ion. This narrow band *short circuit* creates a *dip*-signal in the resonators noise spectrum, shown in Figure 2.15, with a minimum at the current axial frequency of the trapped ion. An off-resonant axial frequency will be visible as a dispersive dip/peak.

The dip signal and the resonator can be described by an analytical function [93, 94], which includes the physical description of the parallel RLC circuit and the parallel ion as an LC series circuit:

$$A_{\text{dip}}(\omega) = \frac{A_0}{1 + \frac{1}{\tau} \frac{\omega}{\omega^2 - \omega_z^2} - Q \left(\frac{\omega}{\omega_{\text{res}}} - \frac{\omega_{\text{res}}}{\omega} \right)^2}, \quad (2.81)$$

¹⁸There are a few other names for this shift used in the literature, e. g. coil pulling shift, coil pushing shift or frequency pushing shift.

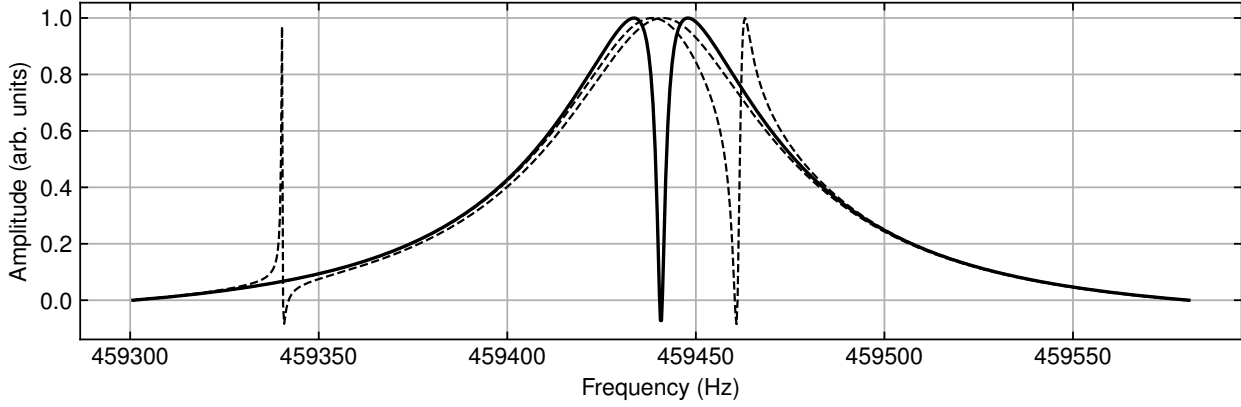


Figure 2.15: Dip-Fit function with axial frequency in perfect resonance (thick line), and 20 Hz and -100 Hz off resonance (dashed lines).

where ω_z is the axial frequency of the ion, ω_{res} is the resonance frequency of the tank circuit, A_0 is the amplitude and $\tau = 1/(2\pi \cdot \gamma)$ defines the dip width γ . The fit function for a decibel scale (typically used in spectrum analyzer for convenience) including a noise offset A_{offset} originating from the amplifier and a first order approximation of a frequency depended transfer function, is given by:

$$A_{FFT} = 10 \log_{10}(A_{dip}(\omega) + A_{offset}) + th(\omega - \omega_{res}), \quad (2.82)$$

where the $th(\omega - \omega_{res})$ term acts as an approximate transfer function of the amplifier with th typically $\ll 1$ [93]. As this fit function includes the interaction between the ion and the tank circuit, it also includes the frequency shift given in Equation 2.80, which means that ω_z extracted from a fit represents the unperturbed axial frequency.

The dip-width (-3 dB) of the dip signal is proportional to the cooling time constant and number of ions N [83]:

$$\Delta\nu_z = \frac{N}{2\pi} \frac{1}{\tau} = \frac{N\gamma}{\pi}. \quad (2.83)$$

With $1/\tau$ proportional to q^2/m , the dip gets wider with higher charge states and smaller masses. Because of the squared charge dependence, lowly charged ions can suffer from very narrow dips, which require longer measurement times to resolve these. Also, the dip should ideally reach the noise level of the background noise around the resonator. If this is not the case, this is a sign of an unstable or inharmonic trapping potential, resulting in frequency variations and a smeared-out dip.

When a dip signal is visible, the ion reached thermal equilibrium with the resonator at temperature T_z and the ions amplitude can be calculated using Equation 2.24 [83]:

$$E_z = k_b T_z = \frac{m}{2} \omega_z^2 z_0^2 \quad (2.84)$$

$$\Leftrightarrow z_0 = \sqrt{\frac{2k_b T_z}{m\omega_z^2}}. \quad (2.85)$$

When Monte Carlo simulations are performed to determine distributions of radii or frequency shifts, the thermal energy has to be Boltzmann distributed.

2.5.2 Radial frequency determination

The determination of radial frequencies is conducted indirectly via the axial detection system. Either by the classic double-dip method [95] or by a phase-sensitive detection method [86], both based on the coupling of a radial mode to the axial mode. As the coupling between radial and axial frequencies will cause a degeneration of the axial frequency, see Equation 2.71. This will be visible as two axial signals, initially even two peak signals. If the axial frequency is on resonance, it will be resistively cooled, and with that indirectly also the radial mode. If the motion is cooled two dip signals will be visible on the resonator. The magnetron and cyclotron frequencies can be extracted from the two dip positions, the applied RF signal and the actual axial frequency:

$$\text{magnetron double dip: } \omega_l + \omega_r = \omega_z + \omega_{rf} - \omega_- \quad (2.86)$$

$$\text{cyclotron double dip: } \omega_l + \omega_r = \omega_z + \omega_+ - \omega_{rf} . \quad (2.87)$$

Such a double-dip signal is fitted using the following analytical function [93, 94]:

$$A_{\text{double dip}}(\omega) = A_0 \cdot \text{Re} \left(-\frac{A}{B + C} \right) , \quad (2.88)$$

where A , B and C are,

$$A = i\tau_l\tau_r\omega\omega_{res}(\omega - \omega_l)(\omega + \omega_l)(\omega - \omega_r)(\omega + \omega_r) \quad (2.89)$$

$$B = \omega\omega_{res}(\tau_r\omega(-\omega^2 + \omega_r^2) - i\tau_l(\omega - \omega_l)(\omega + \omega_l)(\omega(-i + \tau_r\omega) - \tau_r\omega_r^2)) \quad (2.90)$$

$$C = Q\tau_l\tau_r(\omega - \omega_l)(\omega + \omega_l)(\omega - \omega_r)(\omega + \omega_r)(\omega - \omega_{res})(\omega + \omega_{res}) . \quad (2.91)$$

The extracted ω_l and ω_r from the fit are then used in combination with the applied RF at ω_{rf} and the previously measured ω_z to determine the respective radial frequency. This also works for slightly asymmetric double dips that result in a roughly correct ω_{\pm} , allowing an easy method to optimize the coupling frequency.

As mentioned above, if the axial frequency is thermally coupled to the detection system, it will be permanently cooled down to the temperature of the detection system. The energy that is transported from a radial to the axial motion will be gradually cooled away, and, therefore, the radial modes can be cooled even without a directly coupled detection system. The final mean temperature in the radial modes depends on the frequency hierarchy [83]:

$$T_{\pm} = \frac{\omega_{\pm}}{\omega_z} T_z . \quad (2.92)$$

This results in the following thermal radial amplitudes [96]:

$$\rho_{0,+} = \sqrt{\frac{\omega_z}{\omega_+}} z_0 = \rho_{0,-} = \sqrt{\frac{2\omega_-}{\omega_z}} z_0 . \quad (2.93)$$

Noteworthy here is that the thermal radial amplitudes reached with sideband cooling via the axial detection system are equal.

2.5.3 Phase sensitive measurement methods

Phase-sensitive methods are very common to increase the precision of frequency measurements in precision experiments¹⁹. The Ramsey-type measurement scheme applied here, named appropriately *Pulse 'N' Phase* (PnP) method, was already developed in the early 1990s at the MIT precision Penning-trap mass spectrometer of the group of David Pritchard [86]. Phase sensitive measurements are about one order of magnitude more

¹⁹In interferometer experiments a distance is varied instead of time but the principle is the same.

precise than the incoherent double-dip method mentioned above given the same measurement time²⁰ [93]. Since the precision for measuring the reduced cyclotron frequency ν_+ has the highest impact on the final results, this phase-sensitive method is applied dominantly for this frequency measurement.

I will not go into much detail here, since the main principle is easily explained and build-up from the description of excitation and mode-coupling above. For more details, see the original publications, but also the two thesis in ref. [78, 93] give great detail into this method and the similar PnA method as well.

For radial frequency measurements the Ramsey-type measurement is based on two interaction *events* with the radial motion, see Figure 2.16 and the actual data acquisition using the axial detection system:

- 1: The radial motion is excited using a dipole excitation pulse with the goal of imprinting the phase ϕ_0 of the RF pulse on the ions radial motion. In order to successfully imprint a phase, the excitation strength has to be sufficiently strong, which can easily be seen in Figure 2.11. The resulting motional amplitude *will be larger* than the initial thermal amplitude. This increase in amplitude can be beneficial for better signal-to-noise ratio (SNR) later, but is avoided as much as possible at our experiment, due to the high sensitivity (small D_z and high resonator Q -factor) and possible systematic shifts proportional to the motional amplitude.
- 2: With a starting phase ϕ_0 defined, the motion is now interaction-free and accumulates phase:

$$\phi(T) = 2\pi\nu_+T + \phi_0 = 2\pi N_T + \varphi \dots \quad (2.94)$$

where N_T is the number of full revolutions and φ is the partial revolution after the given *evolution time* T . In our setup, the evolution time must be a multiple of 1 ms due to technical reasons explained in section 2.5.

- 2.5: This is a bonus step. Since there can still be a direct interaction of the axial motion with the detection system²¹, a dip can be recorded, allowing the simultaneous measurement of two eigenfrequencies.
- 3: After the evolution time, a π -pulse is applied: The radial mode is coupled with the axial mode using the quadrupole coupling mentioned above. Given a fixed amplitude of the applied RF-pulse, the correct pulse duration t_π must be found to ensure complete inversion of the energies between the two modes. This time can be easily determined from the Rabi-frequency Ω , and therefore from the double-dip splitting $2\Omega = 2\pi/t_\pi$ (with the same RF-amplitude)²². With the π -pulse, not only the amplitude but also the evolved phase of the radial frequency at the time of the conversion pulse is exchanged.
- 4: Given sufficiently increased amplitude by the excitation at the beginning, the axial motion is now visible as a peak signal on the resonator. Until the peak is not cooled in due to the interaction with the resonator, the signal can be recorded

²⁰Depending on frequency (field) stability, this advantage can shrink for very long measurement times.

²¹And should be! It is actually often beneficial for the resolution of the radial frequency measurement, since the axial amplitude fluctuates around the mean amplitude given by the cooling limit of the detection system, but the fluctuation averages down to the mean over the measurement time. A *pick* of an amplitude and removing the interaction can cause a much larger (not averaged) axial amplitude distribution that can increase the distribution of systematic shifts in the radial frequency, resulting in higher phase jitter.

²²The requirement of the precision of t_π is actually not that high, the amplitude conversion is rather flat at the maximum. A detailed investigation of this can be found in ref. [97].

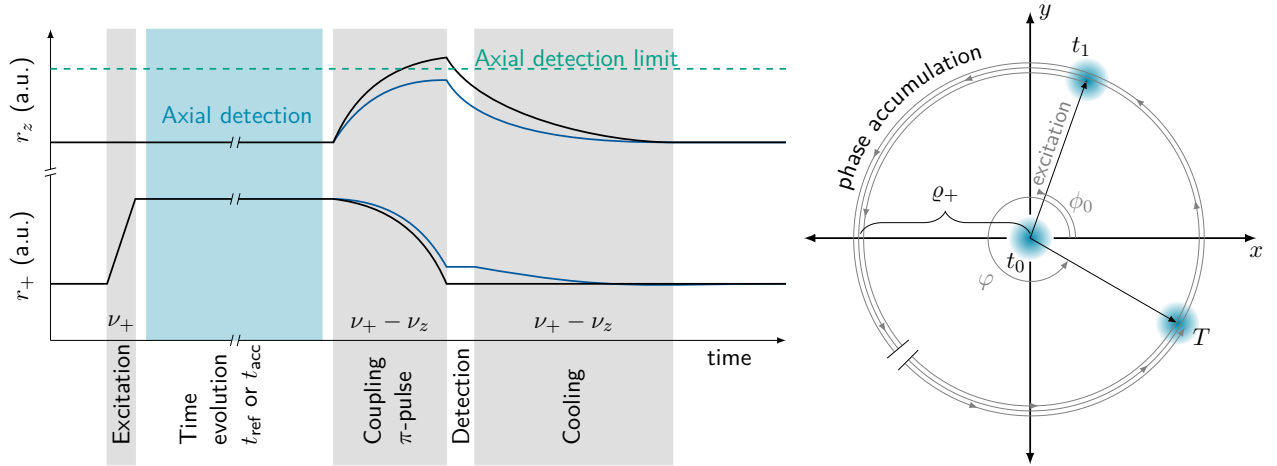


Figure 2.16: An overview of the measurement scheme and changes in motional amplitudes during a PnP-measurement (left) as well as an illustration of excitation and phase evolution of the radial motion (right), modified from [97]. Each gray area represents an active RF signal, annotated with the purpose and the frequency used. The blue section marks the simultaneously performed axial frequency determination during the PnP phase evolution time by recording a dip-spectrum. During the time annotated with *Detection*, the signal from the axial detection system is recorded, which is then Fourier transformed for phase extraction. The right plot exemplary describes the phase imprint and phase evolution in the radial, here modified cyclotron, mode. At time T_{evol} the π -pulse is applied and the current motional phase is exchanged with the random phase in the axial motion. For more details, see text.

and the phase of the axial frequency can be determined using a Fourier transform of the signal (or by a *ring-down-fit*, though not particularly recommended because of the coil pulling shift). As a general rule of thumb, twice the cooling time τ is a good starting point for the duration of the FFT window [82]. The typical duration of the signal used for this phase measurement is between 10 and a few 100 ms. Zero padding is applied to an effective 10 s FFT window in order to interpolate the phase spectrum to a resolution of 0.1 Hz.

- 5: Already mentioned above, at the end the axial amplitude is cooled by the resonator and also continuous sideband cooling of the respective radial mode is applied to *reset* to thermal amplitudes in case of an imperfect π -pulse before.

With a single phase measurement, no frequency determination is possible since, examining Equation 2.94 and rearranging:

$$\nu_+ = \frac{2\pi N_T + \varphi - \phi_0}{2\pi T}, \quad (2.95)$$

shows that only φ is measured and N_T as well as ϕ_0 are unknown. Eliminating ϕ_0 is the first step and possible by subtracting two phase measurements at different evolution times T_{short} and T_{long} :

$$\begin{aligned} \Delta\varphi &= \varphi_{\text{long}} - \varphi_{\text{short}} \\ &= 2\pi\nu_+ T_{\text{long}} + \phi_0 - 2\pi N_{\text{long}} - (2\pi\nu_+ T_{\text{short}} + \phi_0 - 2\pi N_{\text{short}}) \\ &= 2\pi\nu_+ \Delta T - 2\pi\Delta N. \end{aligned} \quad (2.96)$$

This difference of two measured phases is now effectively a phase measurement with the duration of ΔT . Eliminating ϕ_0 this way eliminates not only the phase offset by the excitation, but also the possible phase offsets added in the axial frequency after coupling and or added by the axial detection system.

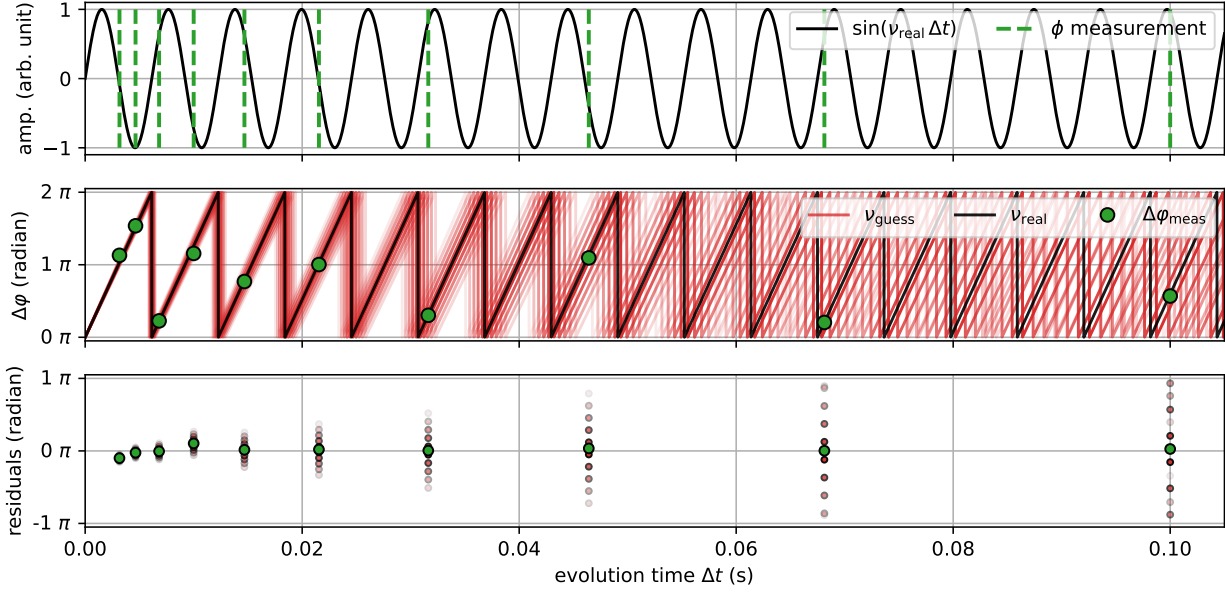


Figure 2.17: Visualization of the N determination principle. In the top plot, a sinusoidal signal at a frequency of $\nu = 1024$ Hz is shown with green markings for the evolution time differences Δt at which the phase is measured (plus the reference time). In the middle plot, the green points are the measured phases (+10 degree white noise). The red lines show the phase evolution of the guessed frequencies with a $[-5, -4, \dots, 4, 5]\%$ deviation to the real frequency, fading with higher frequency distance. The lower plot shows the residuals of the guessed phases compared to the measured phases. The residuals clearly show how the signals with deviating frequency increasingly *dephase* with longer evolution time — the resolution of the frequency determination (or the *sensitivity* on deviating guessed frequencies) increases with higher evolution time.

The determination of the number of full revolutions ΔN requires several measurements: The modified cyclotron frequency is determined first by the double-dip method since it can give an absolute frequency value. Now several phase measurements are performed, e.g. starting with an evolution time of $T_{\text{short}} = 0.1$ s and finishing with an evolution time $T_{\text{long}} = 20$ s. To ensure a successful frequency determination, it is recommended to choose evolution times in between which comply with $T_{i+1} \leq 2 \cdot T_i$. The measurement with the shortest evolution time is used as a reference phase and is subtracted from all other measurements $\Delta\varphi_i$ including the adjustment of the respective evolution time to ΔT_i . The value of $\nu_{+, \text{dd}}$ determined by the double dip is now used as a first estimate, and the following least square optimization on ν_+ is performed by minimizing the following function:

$$\text{RRS}_{\Delta\Delta\varphi} = \sum_i (\Delta\varphi_i - (T_i \nu_+) \% (2\pi))^2, \quad (2.97)$$

with $\%$ being the modulo operator. The function is essentially used in a least square linear fit (ν_+ being the slope and $f(T_i = 0) = 0$ due to elimination of the phase offset ϕ_0), minimizing the residual sum of squares (RSS), with a slight modification aiding the fact that only fractional revolutions are actually measured. A visualization of this N determination principle is show in Figure 2.17.

The resulting ν_+ is now the precisely determined value, with, given a phase jitter of $\delta\varphi$ on the longest evolution time (or ratios, an uncertainty of $\delta\nu_+ = \delta\varphi / (2\pi T_{\text{long}})$). As a quick example, with reasonable phase stability, this results in $\delta\nu_+ = (36^\circ / (2\pi \cdot 20)) = 0.1/20$ s = 5 mHz measurement resolution, and the resolution improves with longer

evolution times and better phase (frequency) stability. This N-determination method is explained in great detail in the thesis of R. X. Schüssler [97].

Given a sufficiently stable magnetic field, it is sufficient to measure the double dip once, followed by the described N-determination with multiple phase evolution times, and afterwards only the longest phase is measured. Every long phase, and the respective difference to the phase measured before, can be used to determine a change in the reduced cyclotron frequency starting from the N-determination, and by continuously unwrapping the phase, this change can be monitored up until the next N-determination.

In our experiment we also always measure the shortest phase between long-phase measurements as a monitoring value since given its low frequency resolution it should remain stable over all times. If the short phase loses stability, its a strong indication for some disturbance in the measurement or a faulty measurement routine.

Multiple parameters of this measurement sequence can and must be optimized when performing actual measurements. First, the excitation amplitude (the reached radial amplitude) needs to be minimized to a level where the measured phase of consecutive measurements is still stable. This can be done rather rapidly with short phase evolution times, as we are only interested in phase jitter due to insufficient SNR²³ and do not need high-frequency resolution. The π -pulse is essentially fixed, but with pulse shaping, the pulse duration extracted from the double dip will be too short. The π -pulse duration has to be multiplied by the ratio between the integral of a rectangular window and the window function used. In a running experiment, it can also be optimized by maximizing the amplitude in the axial mode after the π -pulse. As mentioned above, the duration of the measurement in the axial motion can be optimized to increase the resolution of the measurement of the axial phase. Given a stable axial frequency, the window length is limited only by the cooling time (resonator damping). If the axial frequency is drifting during the measurement, which can happen due to either field inharmonics and the strongly changing axial amplitude or due to voltage variation on the electrode potential due to technical reasons, the phase jitter will increase. Although every step should be taken to minimize the origin of a drift, a shorter measurement window might also improve the phase stability because the range over which the axial frequency drifts is reduced.

For an estimation of phase jitter, caused by field instabilities, systematic shifts in combination with the amplitude distribution caused by the cooling method or time instabilities, a Monte-Carlo type simulation is available in a Jupyter Notebook `ft-icr_toolkit\JupyterNotebooks\simulations\PhaseJitter_PnA.ipynb`. The scripts included allow one to create polar plots to visualize the phase evolution and, with some examples included, can be used to scan parameters and show their impact on the phase stability.

²³SNR of the peak over the detection systems resonator or SNR of the excitation phase imprint is basically the same here due to the cooling mechanism.

Chapter 3

The Pentatrap Mass Spectrometer

The PENTATRAP experiment is, as the name suggests, equipped with five Penning traps. The idea behind the five traps is described in detail in section 3.3 and again later in the data analysis section 4.1. In the following chapter I will give a brief overview of the setup, with some details on parts that have changed compared to previous publications [11, 13, 14, 20, 58, 74, 98] and theses [59, 79, 81, 94, 97, 99–101] and some maybe interesting details that were either not described elsewhere or are of specific interest within this thesis. In the same chronological order as the real experiment, the first section 3.1 will describe the ion production, transport and catching, followed by section 3.2 describing the complete Penning trap apparatus. The chapter is concluded with the description of the measurement procedure in section 3.3.

3.1 Ion production and transport

EBITs The highly charged ions used in our measurements are produced in electron beam ion traps (EBITs). A schematic of the basic working principles of an EBIT are given in Figure 3.1. These devices use an electrode structure similar to cylindrical Penning traps to store charged particles axially, while the radial confinement is realized by a combination of a (focusing) static magnetic field and the space charge of the focused electron beam with a current of up to approximately 30 mA in our EBITs. The few keV electron beam also provides the ionization mechanism: electron impact ionization of the elements and molecules in its path. The spatial confinement of charged particles in the trap region then allows for further ionization of trapped ions. Without disturbance this continuous ionization combined with recombination processes of free electrons in the created plasma and other plasma processes will evolve in an equilibrium state after not much longer than a second.

The maximum of the charge state distribution depends on multiple parameters, first of all the kinetic energy of the electron beam in the trap region, typically 3 keV to 10 keV. The beam energy is defined by the negative potential of 1 kV to 3 kV of the electron gun/cathode and the positive potential of 2.5 kV to 7 kV of the central trap electrodes. Typically, at least twice the ionization energy is needed in electron beam energy to efficiently produce the respective charge state.

To extract the produced ions, the *breeding* process is disrupted by opening the axial confinement potential by pulsing down the beamline facing electrode. In practice, the extraction electrode is pulsed repeatedly, with the time between extractions defining the breeding time. High extraction frequency results in short breeding times, moving the charge distribution of the extracted ion bunch to lower charge states and vice versa. With our room temperature, permanent magnet EBITs charge states of up to 50+ in case of heavy elements or even fully ionized lighter elements can easily be reached. A detailed description of the working principles of an EBIT can be found in [101, 102]. As a short summary of a few rules regarding the extracted charge distribution: The highest

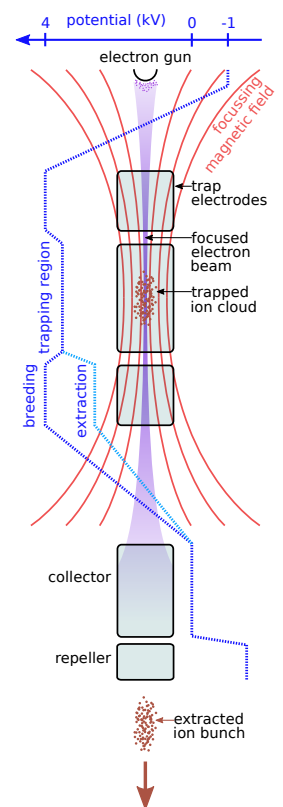


Figure 3.1: Simplified schematic of an EBIT ion source.

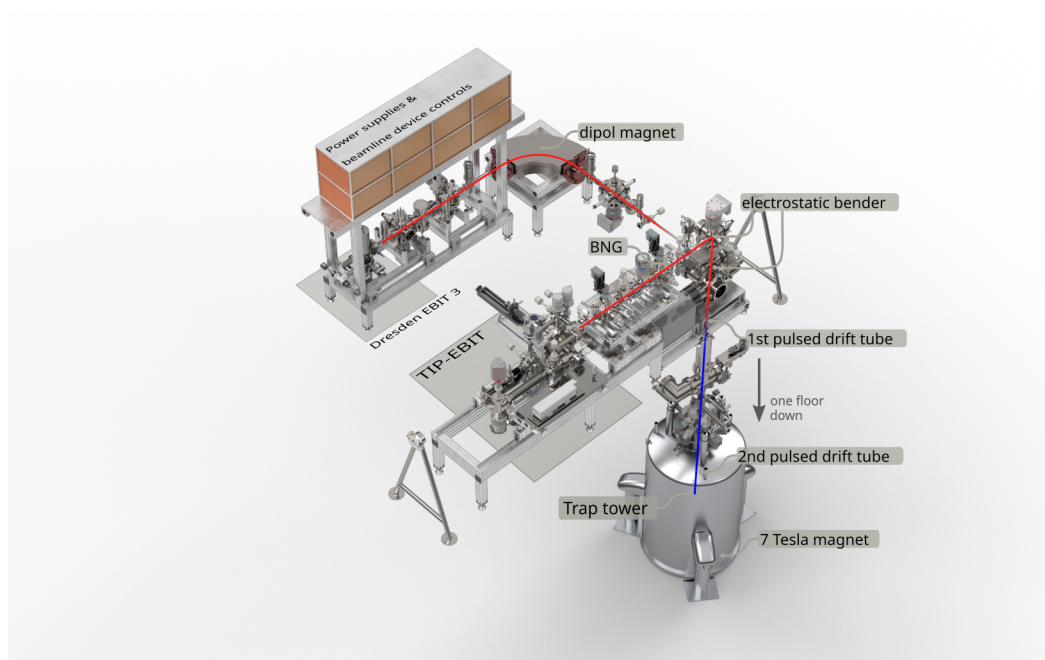


Figure 3.2: Overview of the beamline with major parts labeled. The red line indicates the ion beam after extraction from the ion sources, fading to blue at the position of the pulsed drift tube indicates the reduction of kinetic energy. The acronym *BNG* stands for Bradbury-Nielson gate, which is used as a rough charge-to-mass filter via the time-of-flight separation of the ion bunch extracted from the TIP-EBIT [104]. The dipole magnet acts as a charge-to-mass filter for the ion bunch from the Dresden EBIT 3 [105] via velocity separation. There are several ion optic and diagnostic elements to control and optimize the ion beam for successful transport to the trap tower which are detailed in [81, 94]

charge states are reached with highest electron beam energy and current¹, long breeding time, high trap depth (difference of outer and inner drift tube potentials), low residual pressure and a low amount of contamination elements/isotopes with much higher masses than the desired one (because of evaporative cooling lighter ions escape faster [103]).

In order to produce ions of a specific element or isotope, they have to be introduced into the trapping region of an EBIT. In the most simple case, the element is gaseous at room temperature, so it can be introduced using a capillary and a suitable vacuum inlet system. The next best solution could be to use a molecular compound that includes the element or isotope of interest and is either gaseous or has a sufficiently high vacuum pressure. This method is described in detail for our setup in [101], including the description of a remote-controlled inlet system used in our setup. So far, these methods are rather wasteful in the sense that most of the atoms introduced are pumped away and lost. For several of our measurement campaigns, the amount of isotopes is limited, because they are not naturally abundant enough and enriched samples are needed². For these cases, the novel TIP-EBIT was developed within our group [104]. This specialized EBIT allows us to efficiently produce highly charged ions from small samples using laser-ablation from a target directly beside the electron beam in the trap region with minimal consumption of sample material. For the production of ytterbium ions using the TIP-EBIT a long breeding time of typically one second was used, also because this is the

¹Actually the electron beam density, but that parameter also depends strongly on the focusing ability of the magnetic field as well as the electron gun / cathode size and position which is not trivial to manipulate in an existing EBIT setup. The electron beam current is the far more accessible parameter.

²In case of the measurement of the Q -value of the electron capture in ^{163}Ho the sample is bred in a nuclear reactor facility and only a few μg are reserved for the mass measurements[17].

default repetition rate of our ablation laser. In combination with a trap depth of a few 10 Volts, low residual gas pressure of few 10^{-9} mbar and no significant contamination ions, charge states of up to 45+ have been efficiently produced. The charge state 42+ was chosen for the actual measurements because its the nearest closed electron shell configuration, which is beneficial for the binding energy calculations. For the production of neon and carbon ions the breeding time was significantly reduced to a few 10 ms, since with longer breeding times highly charged ions from heavier contaminants dominated over the light neon and carbon ions in the extracted ion distribution.

An overview of the current beamline, starting with one of our two EBITs and ending with the superconducting magnet and the Penning traps within, is given in Figure 3.2. The former workhorse for the production of highly charged ions at PENTATRAP was the commercially available Dresden EBIT 3 [105]. The capabilities of this ion source and the followed beamline section with the dipole magnet for charge-to-mass separation are described in [101]. This beamline arm was used to produce highly charged ions for commissioning measurements using highly charged xenon isotopes [11, 79, 94, 98], as well as the first Q -value and meta stable state energy determinations using highly charged rhenium and osmium ions [13, 14]. For these measurements, gaseous or high vapor-pressure compounds could be used.

Beamline In the new TIP-EBIT beamline arm, a rough charge-to-mass selection is performed with a Bradbury-Nielsen gate [106], controlled with ultra-fast high-voltage switches, again designed in-house and described in detail in [107]. The *filtered* ion bunch is at the end of both arms bend downwards, where they enter the vertical beamline connecting the upper beamline level with the magnet room in the cellar. The kinetic energy of the ions at this point is a few thousand volt per charge, defined by the potential difference of the EBITs central electrodes to the beamline potential, which can be considered ground potential. To catch the ions in the trap tower with trapping potentials of up to 100 V, the extracted ion bunch has to be slowed down. This is done using a pulsed drift tube, which is just a long tube with a switchable potential. The ions slow down when entering the tube because of the initial high potential. Timed correctly, the tubes' potential is then switched down to ground and the ions are not accelerated again on exit. The first pulsed drift tube in the upper part of the vertical beamline is about 1 m long and reduces the kinetic energy down to 100 V to 200 V. With this kinetic energy, the ion bunch enters the stray magnetic field of the superconducting magnet, which also acts as a focus. The next drift tube located right on top of the trap tower in the cryogenic region of the experiment is only 10 cm long, has an inner diameter of 3 mm and slows the bunch down to a few V. A more detailed description of the vertical beamline as well as details on beam diagnostics can be found in the thesis of A. Doerr [81].

This low kinetic energy is sufficient to catch the ions with the most upper trap of the trap tower. A detailed description of the ion catching procedure is given in the thesis of R. Schüssler [97]. Although the whole process seems straight forward, optimizing the beamline settings for successful ion loading is cumbersome and requires successive tuning of the ion optics and timings. To that end, the beamline is equipped with multiple diagnostic elements, like Micro Channel Plates (MCP) and Faraday cups, to get feedback and visualization on the beam position and intensity. We made some progress in the automation of this process, see [108], but an initial signal is necessary to optimize and local maxima are numerous, so *simple* minimizer/maximizer algorithms can be stuck in false optimal settings³.

³Beam alignment and transfer optimization is an art, but since humans improve with practise, automation is not a thing of impossibility.

3.2 Penning trap apparatus

The Penning trap mass spectrometer can be divided into a few essential sub-parts: The superconducting magnet, which provides a strong homogeneous magnetic field and, as a byproduct in cold-bore magnets, also provides the cryostat for the experiment. The electrodes forming the traps and the cryogenic detection system and the electronics attached to them. The room-temperature electronics and devices creating stable potentials for trapping and completing the detection chain. The next section will give an overview on the details of these individual parts.

3.2.1 Superconducting magnet and stabilization system

The superconducting magnet built by Varian (which is now a Siemens company and has stopped building magnets) is built for a most stable and homogeneous field of around 7 T. It is a vertical cold-bore magnet with two capillary connections between the inner (bore) and outer (magnet coils) liquid helium cryostats. In addition to the main coils, the magnet is equipped with shimming and shielding coils. The shielding factor has been measured to be around 70 [109]. Shimming was performed after the last magnet warm-up and recharge in 2015⁴, using a magnetic field probe. Additional shimming with the actual measurement setup inside the magnet and using ions as sensors was not done.

With the first measurements performed with this magnet, magnetic field fluctuations were one dominant source of statistical uncertainty, see [79]. To minimize one possible origin of these fluctuations, the magnet was equipped with a two-parameter liquid helium stabilization system. The pressure inside the magnet's hole is stabilized by regulating the gas flow out of the inner bore. Since the outer and inner helium reservoirs are connected via capillaries at the bottom, the level inside the magnet's bore is effectively stabilized by regulating the pressure in the outer helium reservoir also via regulation of the gas flow of evaporated helium [109, 110]. Two PID-loops are used: Both output values are flow rates set on mass flow controllers (*Bronkhorst Low- Δp mass flow controller F-201EV* [111]). The input values originate from a precision pressure transducer (*Paroscientific, Inc., 6000-23A Absolute Pressure Transducer* [112]) connected near the bore exhaust and an in-house designed liquid helium level measurement system based on the change of the resonance frequency of an LC-circuit. The LC-circuit uses a 10 cm long cylindrical capacitor which is open on both ends and changes its capacity corresponding to the liquid-helium level due to the different relative permittivity of liquid and gaseous helium. The capacitance is placed above the prevacuum chamber.

The current performance of this system allows to stabilize to approximately 100 μm and 2 μbar to 5 μbar depending on the time scale, see Figure 3.3. An essential addition to achieve this stability in pressure was to attach a buffer volume to the magnet's bore, in our case 200 L. With the stabilization system active the cyclotron frequency fluctuations over time are reduced to mostly a slow negative drift of the magnetic field on the order of 1 nT h⁻¹. However, the short-term stability, relevant for phase-sensitive measurement techniques, appears to have not improved much. The magnetic field stability and possible other sources of phase jitter will be discussed later with respect to the mass ratio measurements performed within this thesis.

The quality of the stabilization system is always limited by the measurement precision and stability of the pressure and level sensors. The level sensor's measurement of the resonance frequency is currently done with a network analyzer. The simple minimum of the minimum in the spectrum is not precise enough and is now fitted with a polynomial

⁴The capillaries on the bottom of the bore connecting the inner cryostat for the experiment with the outer cryostat for the magnet coils was frozen shut so the magnet had to be discharged before it could be warmed up and consequently newly charged afterwards.

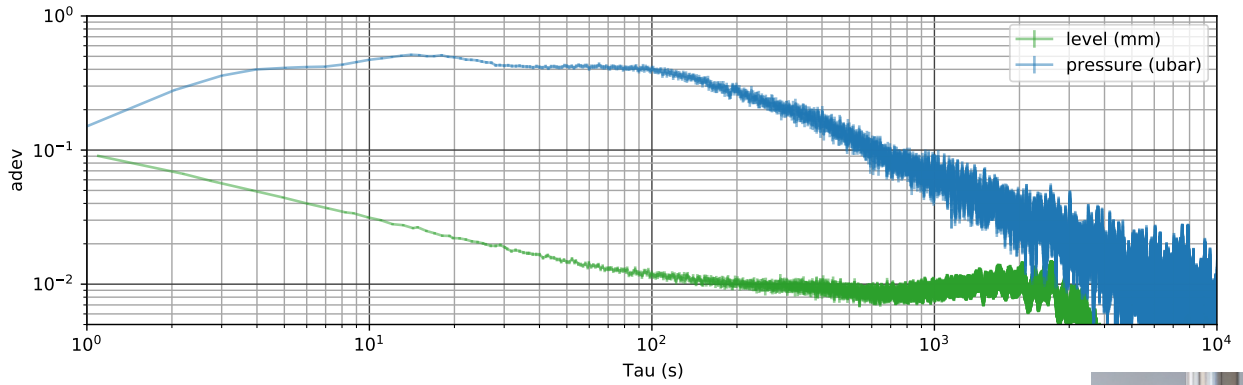


Figure 3.3: Allan deviation of the stabilized pressure and liquid helium level in the magnets bore over approximately 2.8 hours ($= 10^4$ s) during the neon mass measurement campaign. The pressure is given in units of μbar and the level in mm. The behaviour suggests that the level sensors output might be limited by measurement noise, while the pressure sensor is still resolving fluctuations.

to achieve higher precision. Still, the resulting level stability seems to be limited by measurement noise. The precision of the pressure sensor seems to be currently sufficient given the fluctuations that can still be resolved. However, this also shows that the PID controller can possibly be further improved. Without additional sensors to cross-check the measurement values at higher or similar precision, the seemingly perfect long-term stability is possibly not real, since the pressure sensor might be drifting. The same is true for the level sensor. For further optimization of this system, additional sensors have to be installed, and the cross-correlation between pressure and level stabilization has to be properly considered in the PID controller.

3.2.2 Cryogenic insert - traps and electronics

An overview of the cryogenic insert is given in Figure 3.4. Great detail about the current iteration of this setup regarding the mechanical, electronics and detections system design can be found in the theses of A. Rischka [94] and R. Schüssler [97]. Details about the Penning trap tower design and manufacturing of the trap electrodes are generally extracted from and can be found in the theses of C. Roux [59] and J. Repp [99]. Here I will give just a few details to give the necessary information for this thesis and details on some modifications.

Trap tower The trap tower consists of five identical Penning traps with an inner radius $\rho = 5$ mm stacked on top of each other; see Figure 3.5. All electrodes are produced from highly pure $> 99.999\%$ OFHC copper and have been galvanically gold plated with a layer thickness of $20 \mu\text{m}$. Including gold plating and thermal shrinking, the machining precision is $\approx 5 \mu\text{m}$. For electrical isolation between the electrodes, sapphire rings are used. These have even lower manufacturing tolerances of $\approx 0.5 \mu\text{m}$. Each of the three central traps has one split correction and one split endcap electrode to achieve stronger Q_{xz} values at the center of the trap for more efficient sideband coupling. A summary of the trap geometry parameters and the ideal trapping parameters is given in Table 3.1. The d_i factors describing the dependence of the even-order field coefficients c_i on the tuning ratio according to Equation 2.39 are given in Table 3.2.

A nice way to familiarize yourself with the effects of applied potentials, manufacturing errors, and patch potentials is to simulate the trapping potential. One approach is to use some of the symmetry considerations and apply analytical solutions of the



Figure 3.4: Photo of the cryogenic insert without outer prevacuum chamber.

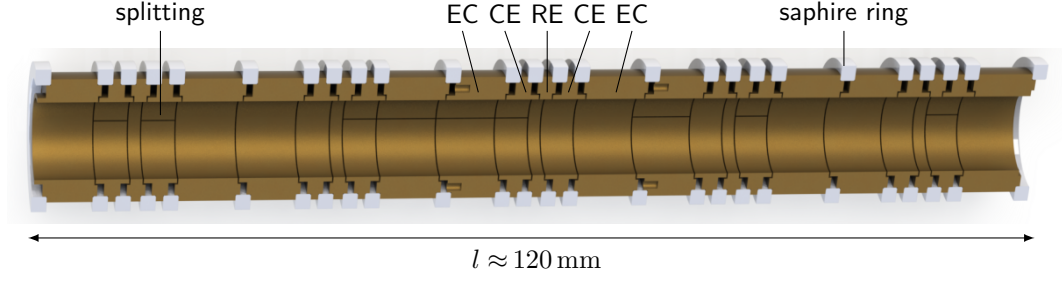


Figure 3.5: Rendering of a cross-section of PENTATRAP's trap tower, with the first (top) trap on the left. All actual electrode splittings are visible. The central trap is annotated with labels marking the endcap electrodes (EC), correction electrodes (CE) and ring electrode (RE).

Table 3.1: Geometric parameters of PENTATRAP's 5-pole Penning traps (in mm) and the resulting c_2 and ideal tuning ratio TR for minimized c_4 as well as the difference Δ_{TR} to a minimized c_6 [59]. All values here are determined from simulation.

ρ	l_{gap}	l_r	l_{ce}	l_{ec}	c_2 (1/mm ²)	$TR _{c_4=0}$	$\Delta_{TR} _{c_6=0}$
5	0.15	1.457	3.932	7.040	-1.496×10^{-2}	0.881032	22.9×10^{-6}

trapping potential on the central axis, as was done in [59] for the geometry optimization. In the python package included in this thesis is an implementation of this (`fticr_toolkit/displacement.py`), for arbitrary electrodes with equal inner radius, as well as some specifically tailored methods for our case of stacked 5-pole Penning traps and to use the actual configurations datasets we use in the measurement scripts. This method was also used to estimate the impact of the machining precision on the potential coefficients, as well as the impact of patch potentials.

A multitude of DC inputs and RF in- and output are necessary to operate the experiment, interact with the trapped ions, and get the measurement signals out. All DC potentials for trapping are filtered with simple RC filters ($R = 40 \text{ k}\Omega$, $C = 22 \text{ nF}$ ⁵) corresponding to a cutoff frequency of $f_c \approx 180 \text{ Hz}$. The RF signals for excitation and coupling are capacitively coupled to the DC potential. Before coupling, semiconductor switches (*MACOM SW-239*) are placed that connect the RF lines to ground to reduce the amount of external noise coupled in the trap. These switches are opened (high impedance) when an RF signal is supposed to be coupled into the trap. Short RF-pulses can be distorted and might be followed by slow degrading DC offset on the trap electrode. This directly effects the static trapping potential and adds possible systematic shifts that are additionally time dependent. This DC offset is circumvented via pulse shaping of the RF pulse (e. g. with a Hann or Tukey window functions), see Figure 3.6, due to the gradually increasing and decreasing RF signal. The shaped pulse does not excite an ion to the same radius as a normal pulse with the same length and amplitude and also the length or the amplitude of a π -pulse needs to be longer for shaped pulses. Therefore

⁵And an additional 100 pF to reduce resonance conditions.

Table 3.2: Leading order even electrostatic coefficients c_i from simulation with ideal tuning ratio $TR|_{c_4=0}$ and the corresponding trap parameters d_i [59]. All coefficients are given in 1/mm^{*i*}. The given uncertainties correspond to the given machining precision for the electrodes.

j	c_j	d_j
2	$-1.496(0.007) \times 10^{-2}$	$-0.025(1.241) \times 10^{-4}$
4	$0.000(4.199) \times 10^{-6}$	$-8.406(0.001) \times 10^{-4}$
6	$-0.008(1.892) \times 10^{-7}$	$3.579(0.019) \times 10^{-5}$

all preparation measurements to optimize the PnP settings have to be conducted with shaped pulses.

All semiconductors used in the cryogenic region (transistors, switches, and diodes) are generally GaAs based because of the high electron mobility that allows them to still perform at these low temperatures. Also, only NPO-type (equally COG-type) multi-layer ceramic capacitors are used, as these proved to be the most reliable at these low temperatures.

Axial detection system The detection system consists of two stages: The first stage is placed near the trap inside the prevacuum chamber submerged in liquid helium in the magnet's bore. It consists mainly of the LCR circuit described above (section 2.5) and a cryogenic amplifier. The second stage is outside the magnet: The signal is further amplified and Fourier transformed for spectral analysis of the signal. While this is mostly sufficient for the topics within this thesis and some modifications will be introduced later on in section 3.2.2, much more detailed descriptions of PENTATRAP's detection systems can be found in [59, 81, 94, 99, 113].

For redundancy reasons, each trap is equipped with two axial detection systems. One is connected on a split correction electrode, and the other on a full correction electrode. During the measurements presented here, only the resonators connected to the full electrodes were used, mostly because their quality factors were higher. The design of our toroidal superconducting NbTi-resonators is described in detail in ref. [113]. The inductance of these resonators is approximately $L \approx 2 \text{ mH}$ to 5 mH and they are wound as auto-transformers with a *tap* to connected the amplifier to. This reduces the impact of the amplifier input capacity and input resistance on the RLC circuit, but also reduces the signal strength⁶. The amplifiers for the axial detection systems are based on a design by S. Sturm [93] and are described in ref. [97]. A simplified schematic of the detection system is (also) shown in Figure 3.8.

Varactor upgrade Adjusting the trap voltage to tune the ions axial frequency on the detection systems resonance frequency can result in significant measurement systematic due to different axial equilibrium positions for different ions. In order to circumvent this (especially for the Ytterbium campaign), the detection systems were upgraded with a tuning mechanism based on voltage controlled varactor diodes. The schematic is shown in Figure 3.8 and an image of one of the add-on boards in shown in Figure 3.7.

This type of resonance adjustment is not uncommon in industrial applications, and such systems are typically referred to as voltage-controlled oscillators (VCOs). For a high capacitance tuning range and a high Q value, a *hyper abrupt* doping profile is beneficial [114]. This type of varactor is typically GaAs-based, which is also necessary for use in the cryogenic environment. The varactor diodes in use are *MACOM MA46H072* and these show a good combination of capacitance range ($C_{\text{var}} = 1 \text{ pF}$ to 7 pF) and high Q-value. In addition to a large tunable range of a single varactor diode, the use of varactors in parallel can easily increase the tunable range of the detection system resonance. The high Q-value corresponds to a low ESR⁷ and is beneficial for keeping the Q-value of the *RLC* as high as possible even with the attached varactor circuitry. Increasing the coupling capacitance ($C_{\text{couple}} \approx 4 \text{ pF}$) can increase the tunable range as well, but also compromises the Q-value of the RLC circuit. Benefiting from the full range of the variable capacity is only possible by approximately matching the size of the

⁶The signal loss can be beneficial because the Q-value increases and with that the cooling time might be significantly reduced.

⁷ESR is the equivalent series resistance, $Q = |Xc|/\text{ESR}$, with the reactance $|Xc|$

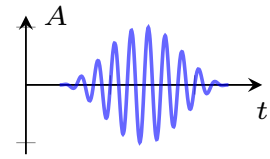


Figure 3.6: Illustration of an RF-pulse with Hann window function.



Figure 3.7: Thumbnail sized varactor add-on board.

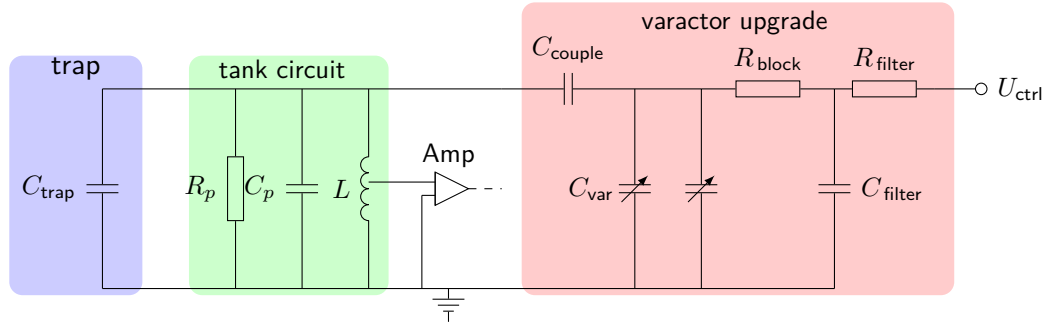


Figure 3.8: Circuit diagram of the detection system with resonance tuning via voltage controlled capacitances (varactor). The resistance R_p and capacitance C_p are parasitic elements of the circuit due to cable shielding and resistance. The trap capacity, or rather electrode capacity to ground, can be determined from simulation as done in [59] and is for our correction electrodes about $C_{\text{trap}} \approx 20$ pF. The tank circuit is strongly defined by the trap capacity. The low pass filter ($R_{\text{filter}} = 10$ M Ω , $C_{\text{filter}} \approx 22$ nF) is reducing external noise input. The blocking resistor $R_{\text{block}} = 10$ M Ω shields the tank circuit from the additional capacitances, e. g. from the filter or cable shielding. The coupling capacitance $C \approx 4$ pF is necessary to separate the DC voltage for varactor control and electrode potential. The shown ground is for simplicity and only in RF a common ground since the DC voltage for the trap electrode is supplied via the cold end of the resonator.

coupling capacity to the maximum varactor capacity:

$$C_{\text{effective}} = C_{\text{trap}} + C_p + \left(\frac{1}{NC_{\text{var}}} + \frac{1}{C_{\text{couple}}} \right)^{-1}. \quad (3.1)$$

Due to concerns regarding low RLC Q-values for the detection system, we chose a low coupling capacity and with risk a low tuning range if the trap and parasitic capacitances are higher than expected; see Figure 3.9. Since the tunability of our system is around ≈ 12 kHz, see Figure 3.10, we can assume that either the parasitic capacitance is rather high or that the trap capacitance was underestimated and/or the inductance is underestimated. For the measurements presented, the given tunable range is sufficient. For future measurements that require higher tunability, the coupling capacitance has to be increased, with corresponding loss in Q-value, which, as it turns out, can be actually favorable for reduced systematic uncertainties of the axial frequency measurement using dip-detection with this system, see subsection 4.2.5.

With the given parameters, resonator inductance and trap capacity in our setup, the Q-values of the detection systems have been reduced by approximately 20%, from 3600 to 3000 and from 12000 to 10000 for trap 2 and 3 respectively. The Q-value does vary over the tuning range, but this is mainly because of the way the Q-value is defined in respect to the resonance frequency. The actual width of the resonance does not change significantly⁸. A high resistance R_{block} is beneficial in shielding the tank circuit from additional capacitance with the drawback of a slow response to a change in the control voltage U_{ctrl} . The impact of several circuit parameters on the Q-value of the resonance, especially the ESR of the capacitances used, can be simulated using SPICE and a template for *LTspice* can be found in [fticr-toolkit/JupyterNotebooks/simulations/](https://github.com/fticr-toolkit/JupyterNotebooks/simulations/).

⁸Except the resonance is tuned on a frequency stable noise peak which will excite the resonance. These are present in our detection system, but are obviously avoided.

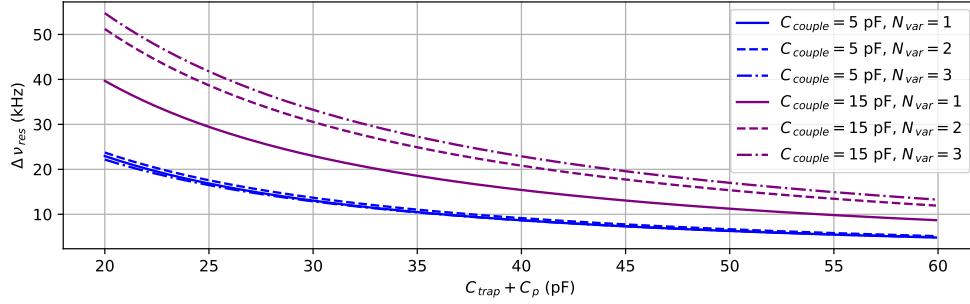


Figure 3.9: Theoretical tunability of an RLC circuits with an inductance $L = 5 \text{ mH}$ and varactors tunable from 1 pF to 7 pF . With a small coupling capacitance the tunability does not increase at all with the number of parallel varactors.

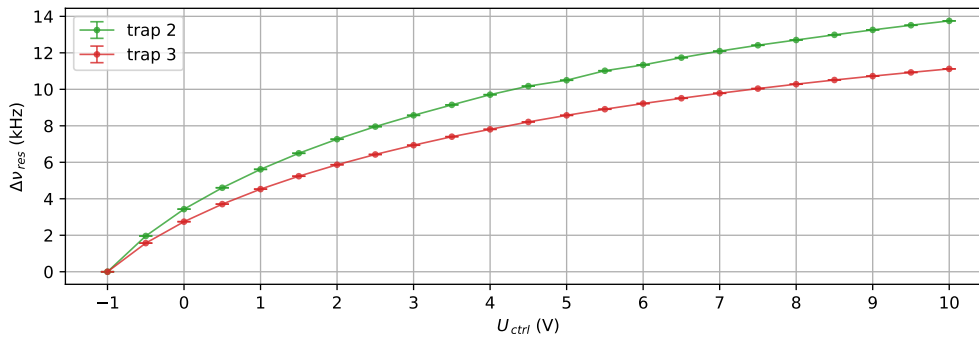


Figure 3.10: Measurement of the resonance frequency in dependence of the control voltage applied to the varactor diodes. The used varactor diodes are rated up to 18 V , but the used supply for remote control is only capable of reaching $\pm 10 \text{ V}$. Due to the given profile, higher voltage will not increase the range as much as the reversed voltage that can be applied.

3.2.3 Room temperature electronics

Voltage supply Fluctuations of the trapping potential will directly translate into fluctuations of the eigenmotions. These effects have been discussed in [81] and are summarized in the following.

Current highly stable voltage sources reach stabilities in the range of a few 1×10^{-8} [115] over the time scale of a 100 s to 10 min . A change in the voltage ΔU_0 of the electrostatic potential connected to the central electrode would result in the following frequency shifts:

$$\frac{\delta\omega_z}{\omega_z} = \frac{\Delta U_0}{2U_0} \quad (3.2)$$

$$\frac{\delta\omega_+}{\omega_+} \approx -\frac{\omega_z^2}{\omega_+^2} \frac{\Delta U_0}{2U_0} \quad (3.3)$$

$$\frac{\delta\omega_-}{\omega_-} \approx \frac{\Delta U_0}{U_0} \quad (3.4)$$

If these fluctuations occur faster than the measurement time, the dip signal would get smeared out, resulting in an increased measurement error. The accumulated phase of the reduced cyclotron motion will also be affected by such fluctuations, but dominantly white noise would average down over the phase accumulation time. If the shifts occur on a larger time scale, it will result in drifts or fluctuations of the eigenfrequencies, but the dip fit uncertainties do not increase, while for the phase measurements the uncertainty effectively increases due to the fact that this uncertainty is determined from the statistical

behavior. When taking ν_+ and ν_- phase measurements, both phase instabilities of the two motions are of the same order of magnitude. This can be a strong hint on a limitation by electrostatic field instabilities, since the frequency dependency on the magnetic field is highly different for the two radial motions.

When treated as a systematic shift (see Equation 2.34), the impact of the axial frequency shift (Equation 3.2 on the free cyclotron frequency would be approximately identical in size to the impact of the reduced cyclotron frequency (Equation 3.3) resulting in a cancellation and no change in the free cyclotron frequency. The magnetron frequency shift would make the cancellation perfect, but it is, given the measurement uncertainties and impact of all eigenfrequencies, irrelevant in size. This cancellation is also logical from the reversed point of view: The free cyclotron frequency corresponds to a particle in a magnetic field. The electrostatic trapping field is only necessary for the confinement, but should not modify the determined free cyclotron frequency in the given magnetic field. Given this situation, it is also clear that the voltage stability on a time scale longer than the time it takes to measure all necessary eigenfrequencies to determine the free cyclotron frequency is irrelevant.

However, this cancellation only works under the following circumstances:

- 1. Both eigenfrequencies ν_+ and ν_z must be measured simultaneously to be correlated in this way. This is, to great extend, implemented at PENTATRAP.
- 2. Both measurement methods for ν_+ and ν_z need sufficient resolution to resolve the fluctuations. The dip detection method for the axial frequency would be limited here (in the presented measurements) to at best 1×10^{-8} relative frequency resolution, resulting in 2×10^{-8} relative voltage resolution.
- 3. No other frequency fluctuations are more prominent than those originating from the voltage instability. This is not trivial to distinguish.

If the voltage fluctuation is not resolved in the axial frequency determination, then fluctuations on the reduced cyclotron frequency will directly impact stability. How strong depends on the specific frequency relation $(\omega_z/\omega_+)^2$ and therefore on the charge-to-mass ratio of the used ions. An overview of the impact of a white noise dominated U_0 is shown in the appendix Figure A.5.

At PENTATRAP the *StaReP* power supply [115] is used to provide the trap potentials. Although the device did undergo several modifications, details on the original design of the supply, controller, reference module (currently based on a cluster of *LTZ 1000* zener diode based ultra precise voltage references [116]) and channels can be found in the thesis of Ch. Böhm [100].

During my PhD, one of the side projects was the optimization of the stability of the trapping potential. For this, the *StaReP* was characterized with the goal of finding the main contributor to voltage fluctuation in the potential source. As an alternative supply and also as a reference voltage for the *StaReP* characterizations, a programmable Josephson voltage standard (JVS), made available by the group of Dr. Ralph Behr from the PTB Braunschweig [117], was also tested. The given programmable JVS (submerged in a separate helium cryostat) is able to produce voltages between 0 and 22 V by selecting (in a binary-system fashion) the necessary number of Josephson junctions in a series connection array. Additional fine tuning can be performed by tuning the microwave source that feeds the junctions.

The stability of the current reference module based on the LTZ, the former reference module based on the VRE 100 voltage reference IC (depricated) and an example channel are measured compared to the JVS shown in Figure 3.11. The references are in specs, reaching nearly a relative stability of 1×10^{-8} after about 10 s to 100 s. The stability

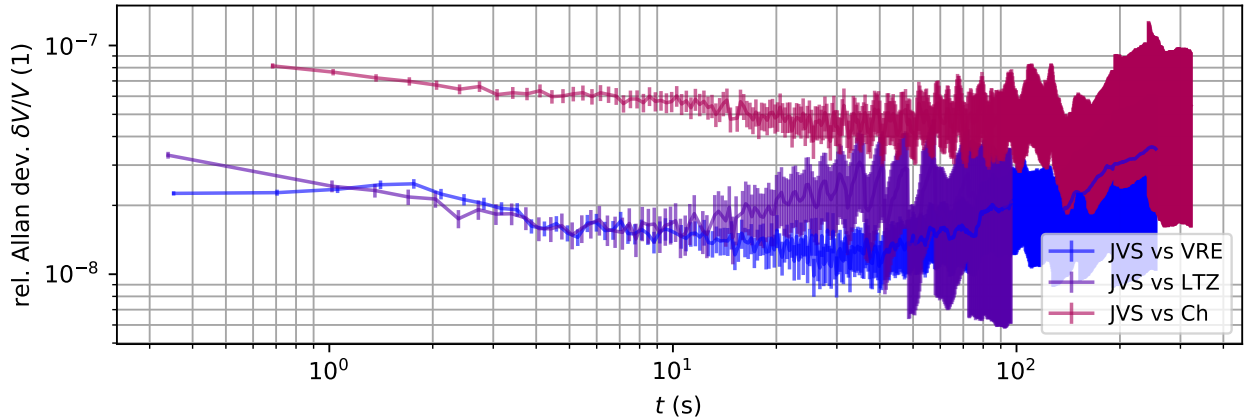


Figure 3.11: Relative Allan deviations of the voltage output of StaReP references based on LTZ 1000 and VRE 100 (both at 10 V) and a StaReP channel (at 21.7 V) compared to the same voltage created by the programmable JVS. The comparison is necessary to reach the high relative measurement precision by measuring near 0 V with mediocre resolution on the voltmeter and in turn higher measurement rate. All values are relative to the actual output of the source and the contribution of the JVS stability to the Allan deviations is assumed to be negligible.

of the channel is much less, which is very much expected since it consists of a DAC-module, a digital to analog converter based on a programmable voltage divider with the reference voltage as input, and a precision amplifier with a fixed amplification factor of 10. Due to the amplification, the stability of the reference input is therefore expected to be amplified by the given factor, but in turn the DAC module reduces the noise dependent on the programmed voltage divider. For the given output voltage of 21.7 V the voltage fluctuations of the channel output are expected to be approximately a factor of 2 larger than the reference stability. The measurements suggest a factor of 3 to 6, suggesting an additional noise contribution from the channel module or a misconception in the assumed noise propagation.

The noise contributions of the channels have been investigated in detail: The absolute noise output of the DAC module was found to be independent of the set voltage. With a noise level of approximately 150 nV to 300 nV at 10 s measurement rate. The measured relative stability of 7×10^{-8} at 10 s measurement rate for a StaReP channel set to 21.7 V corresponds to 150 nV absolute jitter on the DAC output and is therefore consistent. A measurement of channels without DAC module, basically just amplifying the reference voltage, show an approximate stability of 1 μ V, also approximately consistent. That being said, the voltage references themselves reach stability of 150 nV to 200 nV as well. This might suggest that the noise of the reference is capacitively couple to DAC output inside the channel and therefore not divided down as expected. Tests with the JVS as a voltage reference for StaReP did, unfortunately, not improve the stability of the output. This in total suggests, that there probably is a noise source on the channel module, that does couple, possibly via the common ground, to the output of the DAC or equivalently to the input of the amplifier stage.

A complete re-design of the Starep is ongoing now in the electronics workshop of the MPIK, including tests of alternatives for the DAC-ICs, new controller ICs and also grouped blocks of 5 channels per module, since highly correlated noise on the 5 channels supplying one Penning trap drastically reduce the impact on the axial frequency stability.

The use of the JVS voltage source as a direct potential supply was also investigated as the most promising configuration to improve potential stability. Since it is only on potential source, it could be used only by supplying the ring voltage for one of the traps

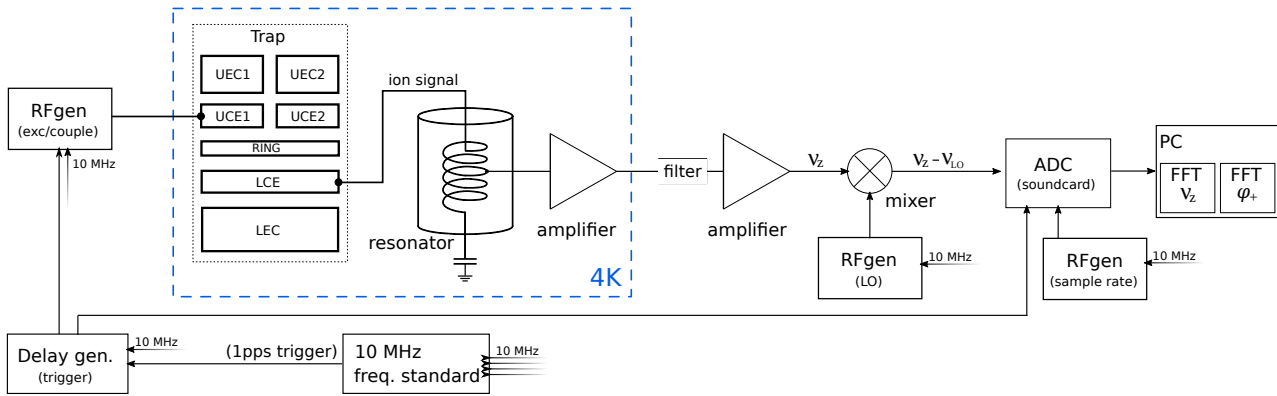


Figure 3.12: Schematic of the detection chain with all devices necessary for the axial dip and phase sensitive detection methods Pnp or PnA. The local oscillator (LO) is not trigger and therefore needs to be set to multiples of 1 kHz and consequentially delay times have to be multiples of 1 ms and additionally the measurement sequence is triggered by a 1 pps signal. The ADC samples continuously, the desired time span for FFT analysis can be defined for multiple FFT instances in relation to the trigger signal.

and keeping the other electrodes supplied by the StaReP. The correction electrodes have only reduced impact on the c_2 parameter (orthogonal trap design) and to keep them supplied by the StaReP is therefore no problem. The endcaps however have been hard-grounded for most of these test measurements. Still, unfortunately, this also did not provide any improvements for the axial frequency stability. The reason could be again coupled external noise (coupled via cables, capacitance to common ground of between trap electrodes), or just that the JVS did not perform well during the tests (optimal operation of the JVS can easily be disturbed by small voltage spikes on the input or magnetic field fluctuations).

In order to test if this is also the case at other experiments, the JVS was moved to another Penning trap experiment (μTeX), build for g -factor determinations. In this setup, it was possible to improve the stability of the axial frequency with the use of the JVS, and the results are published in ref. [118]. This suggests again an external noise contribution at the PENTATRAP-experiment.

Detection chain The detection chain consists of several devices, allowing to manipulate the ion motion with precise timings and analog-to-digital converters (ADC) to sample the output of the detection circuit. An overview of the whole detection chain is given in Figure 3.12.

For excitation and coupling we use arbitrary waveform generators (*Keysight True Waveform Generator 33600B*), where we use the arbitrary waveform feature for shaped pulses for the PnP method tailored in our measurement scripts and uploaded to the generator. This includes shaped pulses for the excitation and coupling, but also the delay is realized here as a repetition of zero amplitude arrays. Therefore, in our setup the waveform generators are fully responsible for the *precision* of the phase accumulation time. For each trap, one RF generator is used and the complete sequence comes from one channel. For each ion, an excitation pulse and coupling pulse are uploaded, which will be then used for all different phase accumulation times. This ensures a correct accumulation time even when the pulse lengths are not accurate, since errors balance out in the phase difference of a measurement phase to a reference phase. In the delay, a common offset would cancel as well, but a relative time error would not. For this reason, the function generators (and all other devices) are locked to a 10 MHz rubidium frequency standard *SRS FS725*. Since our frequency standard is not GPS-locked, the

absolute accuracy is not guaranteed, but the relative time error $\Delta t/t$ is constant over sequential measurements. Such a relative time error creates a common scaling of the measured reduced cyclotron frequencies, resulting in no significant cyclotron frequency ratio shift.

The sampling rate of the RF generators is adjustable; typically the maximum sampling rate of 660 MHz is used, resulting in a time resolution of ≈ 1.5 ns which is fully sufficient even for sampling the highest frequencies needed for measurements at PENTATRAP of about $\nu_+ \approx 54$ MHz.

The resonator signal at approximately 730 kHz and 500 kHz for trap 2 and 3 respectively is amplified and the down-mixed to some value around 10 kHz. This down-mixing is necessary due to the low sampling rate of the ADC, a commercial high-end external sound card *RME Fireface UC* [119] with 24 bit amplitude resolution, at 192 kHz. The low sampling frequency is a drawback of the desired high resolution in amplitude⁹. The local oscillator (LO) for the down mixing is not triggered. To ensure a stable phase relation with the LO, its frequency is set to multiples of 1 kHz, only phase evolution times of multiples of 1 ms are used and measurement sequences are triggered by the 1 pps signal from the frequency standard. The trigger for the RF generator for excitation and coupling pulses, as well as the trigger for the sound card, is created by a precision delay generator *SRS DG645*.

The mentioned FFT-system is an in-house designed system based on the mentioned sound card as an ADC. The sound card was characterized and slightly modified to allow for precise triggering, and an FFT software package was designed by A. Rischka and me for the spectral analysis of the signal. The details can be found in ref. [94]. The benefits of this setup are the synchronized parallel input channels with 24-bit amplitude resolution and in the end the versatile software package, allowing us to perform simultaneous measurements of the reduced cyclotron frequency and axial frequency.

3.3 Measurement scheme

The reasoning behind the five traps in the original proposal for PENTATRAP was based on the idea of exploiting common magnetic field fluctuations in two neighboring traps to improve the measurement precision compared to conventional Penning-trap mass spectrometers, which often experienced significant magnetic field fluctuations that limit the measurement uncertainty. The *cancellation* of magnetic field fluctuation is supposed to work similarly to the *two-ion balance* method [69] with the benefit of eliminating systematic shifts originating from the ion-ion interaction. So far we could not benefit from correlated magnetic-field fluctuations in the sense that these reduce the statistical uncertainty significantly. The cancellation method is applied in the analysis and therefore, as long as two traps are used simultaneously for measurements and also produce actual data¹⁰, the measurement procedure is identical to the *normal* ratio determination via sequential determination of the cyclotron frequencies of two ions. The details of the analysis using the cancellation method are given in section 4.1.

The fifth trap was intended as a monitoring trap. However, it is currently not equipped with a detection system. If desired, in principle trap 4 can be used for the same purpose by loading an ion sequence of A-A-B-A. However, the aspect of using an additional monitoring ion was to gain sensitivity to field fluctuations by picking an ion with a charge-to-mass ratio greater than the actual ions of interest, which would be

⁹The bottleneck here is in the end the transfer rate of the interface to the computer.

¹⁰Which happens if one of the outer ions experiences a charge exchange and is lost from the trap or at least not resonant with the detection system anymore.

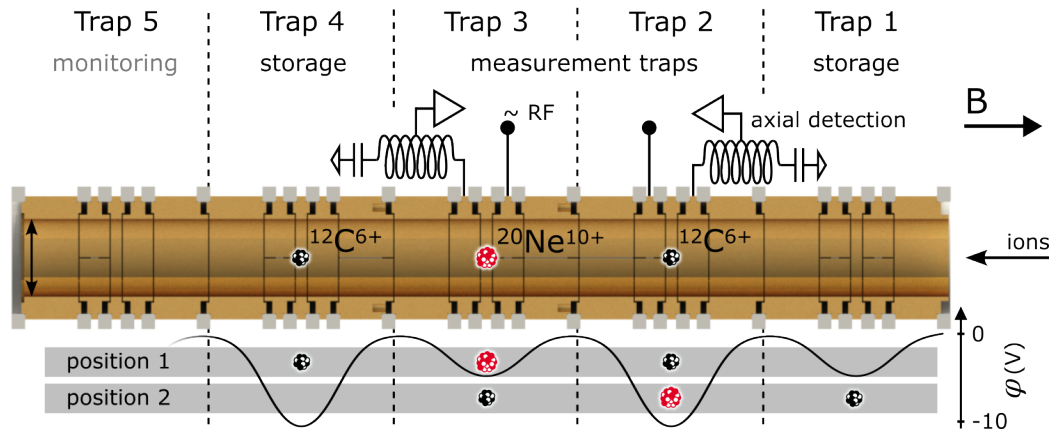


Figure 3.13: Ion configuration for the two *positions* during a measurement, here with neon and carbon ions as an example in the standard A-B-A sequence. In addition, the connections for RF signals to the trap electrodes as well as the detection systems are sketched. The applied potential is, for measurements with fixed detection system resonance, slightly different between the two positions, and, for measurements with tuned detection system resonance, identical in both positions.

impossible in that case. Since no correlated magnetic or electrostatic field fluctuations have been observed so far, there is no reason to use a monitoring trap anyway.

3.3.1 Measurement preparation

For all measurements performed within this thesis, three ions are loaded in an A-B-A sequence in the three central Penning traps (2, 3, 4), see Figure 3.13. Each ion needs to be prepared for the measurements: After an ion loading attempt, which captures the ions in trap 1, the loaded ion (bunch) is transported via potential variation to trap 2 due to the simple reason that the first trap is not equipped with a detection system. After transport, the trap voltage is adjusted to match the ions axial frequency with the resonance frequency of the detection system using the calculated mass of the ion and the design or measured c_2 of trap 2. Up to here, given the ion source is operational and an optimized beamline transport, this happens by the push of a button.

Immediately after loading, all motional amplitudes are typically large and need to be cooled. This is more a feature than a problem, because the large amplitude in the axial mode makes an ion immediately visible in the FFT spectrum of the axial detection system as a large peak. If more than one ion is simultaneously loaded, then multiple peaks appear that are typically easily distinguishable. If more than one ion signal is observed, the bunch is typically discarded, since reloading is faster than removing a contamination ion. A single ion will shortly after transport be in resonance with the detection system and cool in. A short drift of a peak is often observed which is related to the strong DC filters that slow down the adjustment of the trapping potential after transport. In case of the measurements presented here, the type of ion (A or B) is easily distinguishable by the axial frequency, which means that if the wrong species is loaded by accident, it can be discarded directly. If it fits, the ion will cool its axial motion while interacting with the detection system, and a dip signal is visible in the averaged FFT spectrum.

In the next step, the radial motions have to be cooled using sideband coupling, starting with the magnetron motion because frequency shifts due to the large radial amplitudes affect the cooling efficiency less in the magnetron motion. In the moment the RF signal for sideband coupling is enabled, the reaction should be an immediate increase in axial amplitude that disappears after one or two seconds. With the magnetron motion

cooled, the modified cyclotron motion can be cooled via sideband coupling with the same reaction. This presupposes rough knowledge of ν_- and ν_+ , which is the case if you know the magnetic field strength to sufficient precision from previous measurements, allowing to calculate the magnetron frequency to a few 10 Hz accuracy and the modified cyclotron frequency about an order of magnitude better. If there is insufficient information about the magnetic field strength, the sideband frequency can be *scanned* around a rough estimate, while monitoring the axial amplitude, which will rapidly increase if the right frequency for the quadrupole field is applied. For mass and mass-ratio measurements with very small differences in axial frequency (better charge-to-mass doublets) it can be necessary to identify the ion by creating this cyclotron cooling peak, and for metastable state detection, even phase-sensitive measurements are necessary.

With all eigenmotions cooled, and all eigenfrequencies determined as precise as possible using the dip and double-dip methods. These frequencies are used as parameters for the PnP measurements. Afterwards, the ion is transported to the next trap and the next ion of the sequence is loaded, or the trap will be exposed to magnetron noise cleaning [12]: A broadband white-noise RF signal is applied up to $2\nu_-$ and at the same time the magnetron sideband coupling is enabled using a second RF generator channel connected to another trap electrode. Due to the broadband noise, all contamination ions that have so far not been detected will slowly increase their magnetron amplitude, while the ion of interest is continuously cooled. Noise cleaning will be applied for several minutes and afterwards, given that the ion of interest is cooled axially, the trap potential is reduced to $U_0 \leq 50 \text{ mV}$. With this procedure, we can remove contamination ions to some extent, but occasionally it is not sufficient and the measurement data is later discarded on the basis of observed increased phase jitter or unstable axial frequency.

With the full A-B-A sequence loaded and all eigenfrequencies for each ion in each trap determined, a measurement script is prepared and the measurement started. For measurements with a tunable detection system, there is the slight modification of finding a trap depth U_0 that results in axial frequencies of both ions that are in the tuning range of the respective detection system. During preparation and during measurement, all trap potentials are set symmetrically as shown in Figure 3.13.

3.3.2 Main measurement sequence

The measurement sequence for the measurement of the modified cyclotron frequency and axial frequency is shown in Figure 3.14. All steps, with the exception of motional cooling, are triggered to ensure simultaneous measurements in both traps 2 and 3 and a correctly interleaved axial frequency determination via the dip method. The delay between excitation and coupling for the PnP measurement is defined by the RF generator. This measurement sequence is repeated until one of the ions is lost because of charge exchange with rest-gas atoms, and the loading process is repeated. In order to improve this situation, the next upgrade of the setup will include a cryogenic valve that disconnects the cryogenic vacuum from the room-temperature vacuum of the beamline, thus significantly improving the vacuum in the trap tower.

While the measurement is running, not only the phase and axial spectra are recorded, but also many environmental parameters, e. g. the laboratories' temperature and atmospheric pressure, magnetic field fluctuations picked up by three fluxgate sensors (*Stefan Mayer Instruments - FLC 100*), the liquid helium level and pressure inside the magnets' bore, are monitored and saved. Later, these values help identify the reasons for significant instabilities of the measured frequencies aid in the decision if data has to be disregarded.

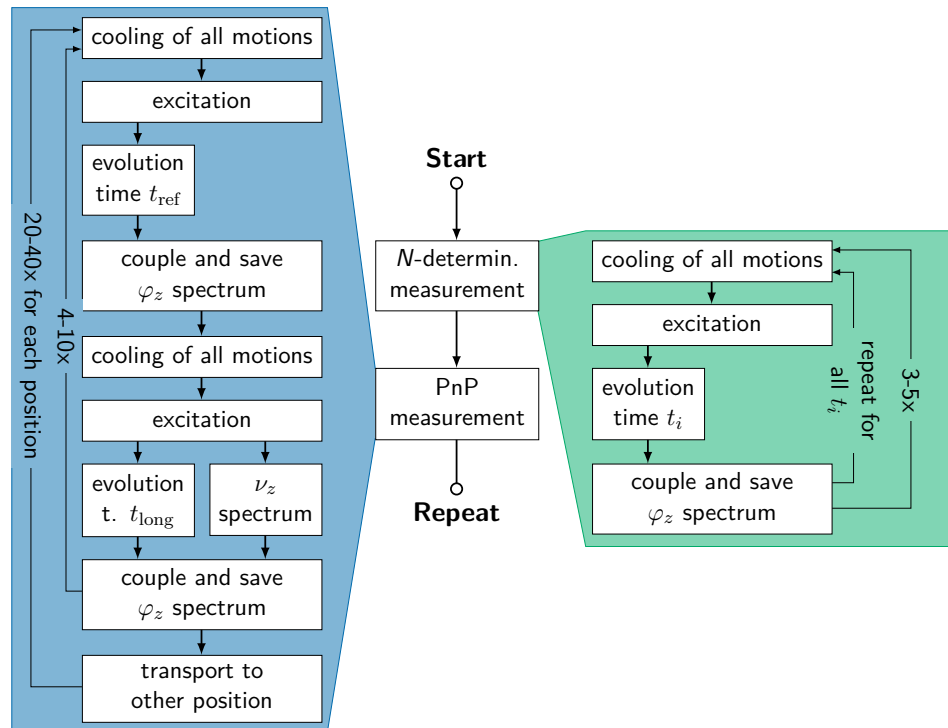


Figure 3.14: Measurement procedure of one measurement *main cycle*, modified from [97]. Each cycle starts with an N -determination to determine the absolute frequency ν_+ , followed by repeated short and long evolution time PnP-measurements to follow the change of ν_+ . Axial spectra for the determination of ν_z are recorded during the long evolution time of the PnP measurement.

Chapter 4

Data Analysis and Trap Characterization

4.1 Data analysis

In the scope of this thesis a python package was written for the analysis of measurement data and calculation of systematic shifts for measurements performed at PENTATRAN. In the next section, the different steps of the data analysis will be briefly presented.

4.1.1 Extracting axial frequencies and phases from measurement data

As explained in section 3.3, the measurement is divided into two parts: the N determination and the main cycle. The analysis starts with the extraction of axial frequencies and phase values from the recorded FFT spectra in both parts. The phases for the N determination are extracted from the frequency bin of the axial frequency given in the config file of the measurement, so the axial frequency from the preparation measurements. The phases of the main cycle can be read out at the possible more precise axial frequency that has been determined simultaneously to the phase evolution time. In any case, with the zero padding resulting in an interpolation of the real frequency bins, slight changes in the axial frequency do not cause a significant deviation in the phase determination, as visible in Figure 4.1.

While for the phase extraction, each individual FFT spectrum recorded is used to extract a phase value, the FFT spectra used for axial frequency via dip-fit are normally averaged over the measurements performed in that position and that subcycle of the measurement, which are four to ten spectra depending on the measurement. For the neon campaign for example 10 repetitions of the measurement are performed during one subcycle, since the dip widths are rather small and the averages are needed in order to properly resolve the dip signal in the resonance, especially in trap 2 due to the low

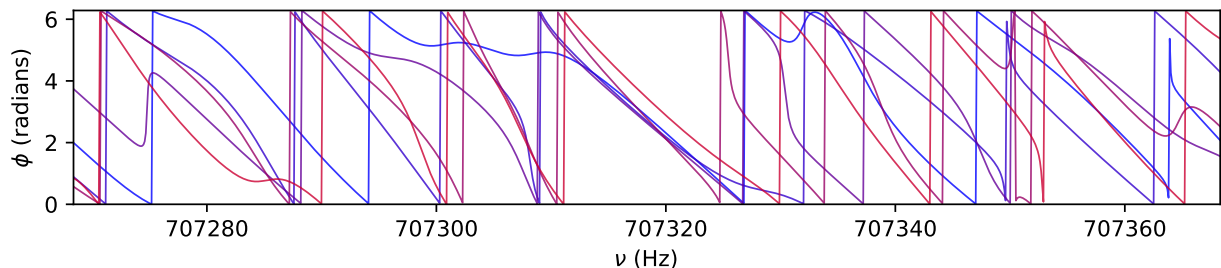


Figure 4.1: Example spectra of five sequential phase measurements with 70 s evolution time. The stable phase around the bin corresponding to the axial frequency of the ion is clearly visible.

Q value. In the ytterbium campaign, a single dip spectrum can in principle be used to extract the axial frequency due to the wider dips and also the longer measurement time of more than 70 s. A comparison of averaging the spectra first to averaging the extracted ν_z from individual spectra showed no significant difference. But this could be different with less stable trapping fields.

These steps, especially the spectra averaging and dip fits, are quite time consuming, and for that reason split from the rest of the analysis script. The ν_z and ϕ_+ values extracted in this *PART1* are saved in tables and are used in the next analysis step. though not implemented, a parallelization would be very beneficial here.

4.1.2 Phase unwrapping, N determination and ν_+ frequency

Phase unwrapping, meaning of adjusting the evolution of the measured phases to not be limited to values between 0 and 2π in order to get a continuous phase evolution, has to be performed at multiple stages in the analysis and multiple methods can be found in the analysis scripts. The first step is always to unwrap the phases of one subcycle by adding or subtracting 2π from each phase that show a difference of more than π to the phase measured before. This is fairly obvious and easy for short evolution times and corresponding low phase jitter, but for the long evolution times and high ν_+ frequencies, this can already be difficult. One solution applied is a simple iterative corrections of the linear drift by performing linear fits of a number of sequential phases to predict the next phase value and unwrap with respect to that prediction. This can be performed with increasing or decreasing time and performing these adjusted unwraps several times in alternating directions can improve the results.

For the main cycle, the phase measurements are not equally spaced: Each subcycle takes typically around 15 minutes and the single phases in each subcycle are spaced by seconds to minutes. If the subcycle phases are averaged, a simple unwrap can be performed, but the median should be used for averaging, since single wrong unwraps will affect the median value less. Another possibility is to unwrap both positions in an interleaved, connected fashion. Since the magnetic field drift is nearly always parallel in both traps, the phases can be unwrapped together by removing the initial phase offset, unwrapping all phases, and adding the initial phase offsets back. This method works with high confidence and is used most of the time without manual correction.

Each set of phases of the same evolution time is also investigated in respect of outliers after the unwrap, filtering out values that are off by 3σ compared to the median. This is also possible with an additional drift correction. The standard deviation of the filtered phase set is also assigned as an uncertainty, though for the main cycle these uncertainties are additionally averaged for the whole data set, and the averaged values assigned as the individual uncertainties as better estimation. In the end of the analysis, these uncertainties measured quantities will be effecting the so-called *inner error* of the final average. The *outer error*, based solely on the statistical variation of the determined ratios and affected by both measured frequencies and the data from both ions, can be compared to the inner error to verify the statistical behavior. For the final output, the higher error of the two is used.

A very detailed description of the N-determination can be found in the thesis of Rima X. Schüssler [97] and the process is identical in this analysis. First, each shortest evolution time phase is subtracted from all other phase with that same averaging index and the evolution time difference of the two measurements is assigned to this new phase value. Now, all phases with the same evolution time are averaged, and the least square optimization according to Equation 2.97 is performed. A plot of the resulting residual sum of squares (RSS) is shown in Figure 4.2, demonstrating the difficulty regarding numerous minima. Due to this, no *real* optimization function, e. g. Nelder-Mead, is

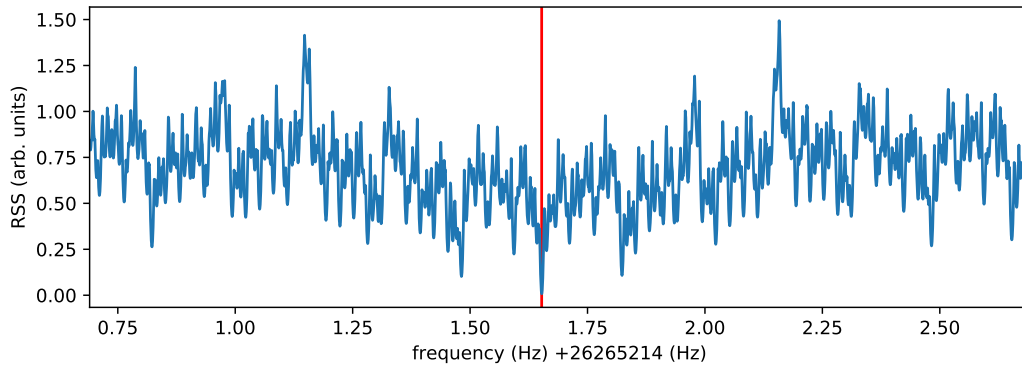


Figure 4.2: Example residual sum of squares (RSS) of an N-determination. The final extracted frequency is marked with a vertical line.

used to minimize the residuals, but instead the reduced cyclotron motion is scanned over a range of few Hz in a resolution smaller than the inverse of the evolution time $1/T_{evol}$ and the optimal (measured) frequency ν_+ is simply determined from the minimal RSS and with that also the number of full revolutions N during that evolution time.

If the cyclotron frequency ratio can be calculated from literature to sufficient precision, it can be used to automatically correct an N error of one revolution in one of the positions. This happens not very often but depending on the measurement case, being off by one revolution in one position is typically a big enough ratio shift to spotted directly.

For the determination of ν_+ over the whole main cycle, the phases of the main cycle have to be connected to the phase of the longest evolution time in the N-determination. This is also done via a linear fit of the phases of the first few cycles, giving an extrapolated phase value for the time of the N determination, which is then used to adjust the phases of the complete main cycle (the main cycle has to be properly unwrap prior to this with the methods given above). With the previous determined N and the unwrapped and *connected* main cycle phases, the respective ν_+ for each phase are calculated.

Given that the frequency values are determined for each phase, these they are not enough corresponding axial frequencies determined from the dip fit since the axial spectra have (most likely) been averaged. The uncertainty of the determined axial frequency can be increased by $\sqrt{N_{averages}}$, or all reduced cyclotron frequencies in one subcycle can be averaged as well. The latter is done for all the measurements presented here and was also tested with the ytterbium measurements if the final results differ from the non-averaged values, which turns out to be not the case. One might want to be careful here, since the two trap cancellation scheme, see below, would probably work best with non-averaged values.

4.1.3 Determining the free cyclotron frequency

The determination of the free cyclotron frequency is made using the invariance theorem (Equation 2.20). The magnetron motion is taken from the preparation measurement performed with double dip. In order to reduce systematic shifts, the magnetron frequency of one ion will typically be calculated from the magnetron frequency of the other ion and the literature mass ratio, which is sufficiently precise considering the requirements on the magnetron frequency. This ensures a precise magnetron frequency difference, which is far more relevant in the invariance theorem than the absolute frequency value.

The same can be done for the axial frequency, although only done here with the measurements using the detection system tuning, since there the equality of the trapping

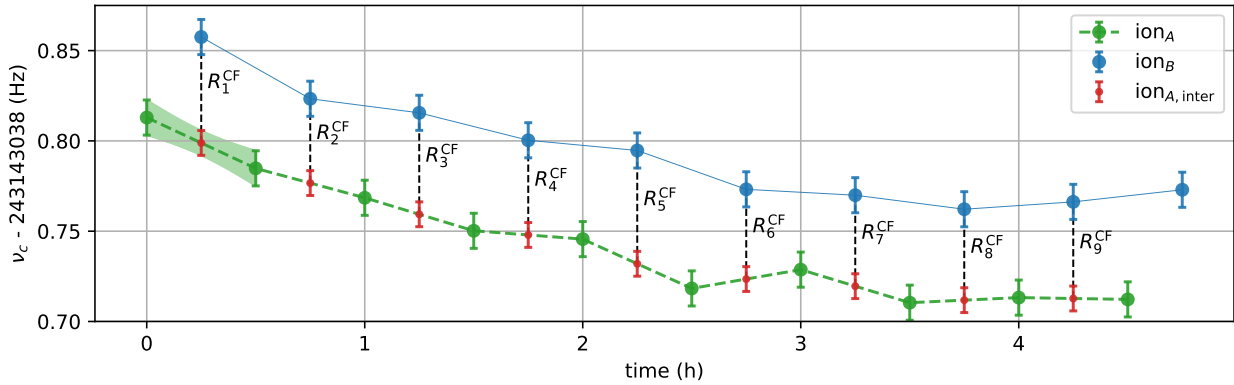


Figure 4.3: Fictional measurement data to demonstrate the principle of the interpolation method for the extraction of cyclotron frequency ratios. The error band of an interpolation is depicted in the green band on the left.

potential ensures better results than the less well-known difference in trap depth with different trapping potentials for each ion.

With all frequencies known, the free cyclotron frequency for each subcycle is calculated and, given former averaging, assigned to each subcycle with the mean time of the measurement as a time tag. These cyclotron frequencies are now also checked for outliers, with respect to a drift correction fit with at least a polynomial function of third order.

This step should also be seen as a disentanglement from the trapping potential. If the eigenfrequencies have been either measured simultaneously or properly interpolated, the resulting free cyclotron frequency is indeed free and independent of the trapping field. This also means, that voltage drifts on time scales longer than the time it takes to determine ν_c are hardly relevant in the end.

4.1.4 Ratio determination via interpolation

If the magnetic field were perfectly stable, the cyclotron frequency ratio could be directly determined of each pair of sequentially determined cyclotron frequencies of the two ions. This is most unlikely, and the reasons for magnetic field disturbances are countless, some of which are discussed in ref. [109]. With the stabilization system in use, the magnetic field of our magnet currently shows a very dominant and mostly constant drift of typically 0.5 to 2 nT h^{-1} . The cyclotron frequencies consequently follow that behavior, causing a ratio shift in a direct determination.

In order to eliminate the magnetic field drift to first order, we can interpolate the measured cyclotron frequencies of one ion to the measurement time of the cyclotron frequency of the other ion. The interpolated value and the cyclotron frequency of the other ion are then used to calculate the cyclotron frequency ratio, as visualized in Figure 4.3. Given that the higher-order magnetic field drifts are small and ideally varying around zero in a way that they average down over the full set of measurement data, this method is as accurate.

In order to at least consider higher-order effects in the analysis, the interpolation is also performed on each second data point of one ion and the average size of residuals between these interpolated values and the corresponding real data points of the same ion is added as an uncertainty to interpolated values. This additional uncertainty is typically smaller than the actual measurement uncertainty in our experiment.

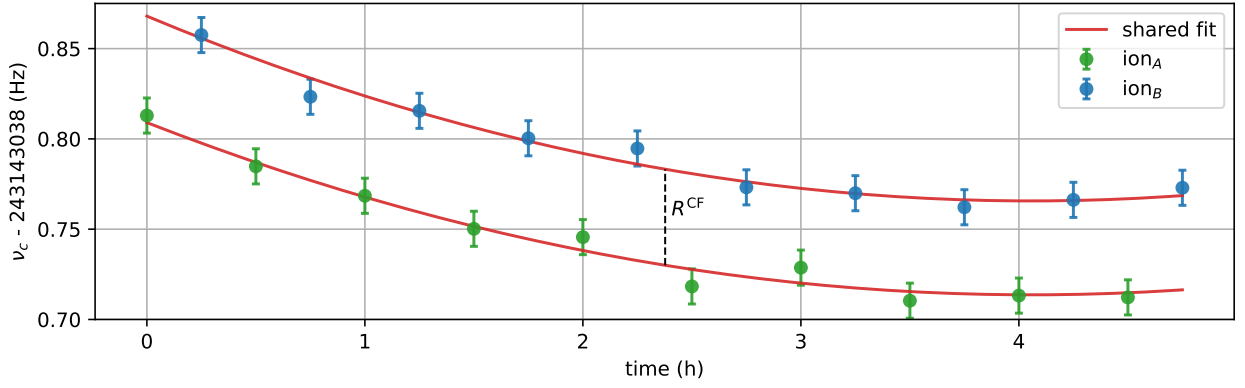


Figure 4.4: Fictional measurement data (same as above) to demonstrate the principle of the polynomial fit method for the extraction of cyclotron frequency ratios.

For the final cyclotron frequency ratio, all determined R_j^{CF} are averaged, weighted by uncertainties. As mentioned before, the larger between inner (uncertainty based) and outer (fluctuation based) error of the This method is used for all cyclotron frequency values currently determined by PENTATRAP, since our magnetic field is stable enough and the least assumptions have to be made to apply it.

4.1.5 Ratio determination via polynomial fit

Another method, previously applied at PENTATRAP, is the shared polynomial fit method. For that method, the assumption is made that the magnetic field behavior can be described by a polynomial function:

$$B(t) = \sum_{i=1} b_i t^i. \quad (4.1)$$

Both ions cyclotron frequencies should follow this polynomial behavior with a factor of R_{CF} between them. The ratio R_{CF} and the polynomial coefficients b_i can now be used as shared fitting parameters for a fit using the ion data sets ν_{c,ion_A} and ν_{c,ion_B} :

$$\nu_{c,ion_A} = C \times \sum_{i=1} b_i t_{ion_A}^i, \quad (4.2)$$

$$\nu_{c,ion_B} = R^{CF} C \times \sum_{i=1} b_i t_{ion_B}^i, \quad (4.3)$$

where C is in principle $(q/m)_A$, and just written here for clarity and to use b_i in the polynomial: In an actual fit function, C it is absorbed by the polynomial parameters b_i . These parameters are only relevant for the fit itself and the only important extracted parameter is R_{CF} . A visualization of this method is shown in Figure 4.4.

At first sight, this seems like a less restrictive assumption and even more precise than the linear interpolation above. The *Achilles heel* of this method though are sudden magnetic field jumps. While the most probable polynomial order will always be chosen using the *Akaike information criterion - corrected* (AICc) [120]¹ for a given dataset, a magnetic field jump may still be poorly described and might disturb the fit and the extracted ratio. For the interpolation method, it will be one or two *bad ratios*, that are

¹The AIC is a method to compare the quality of different models in respect to the data it is supposed to describe (like an F-test), allowing to find for example the most probable (or rather nearest to reality) polynomial describing the magnetic field behavior that produced the cyclotron frequency data. Here the AICc (*corrected*) is necessary due to the low number of data points.

more likely to average down to be negligible in comparison to hundreds of other ratios determined in the complete set of data for these two ions. The polynomial produces only a handful of ratios at much higher precision and the final average is therefore more sensitive to these *bad ratios*.

This was in earlier experiments at PENTATRAP tried to adjust for by grouping the data into smaller subsets, allowing jumps between these subsets. Since the magnetic field is more stable now, this is no longer necessary and the whole 12 h main cycle is always fitted with one polynomial to extract one cyclotron frequency ratio. Still, we use this analysis method currently only as a cross-check and the results do not differ significantly from the results of the interpolation method.

4.1.6 Cancellation method

The cancellation method was the initial motivation for the PENTATRAP experiment: Using two neighboring Penning traps for simultaneous measurements, a common magnetic field fluctuation (constant magnetic field ratio ρ_B) in both traps $B_{\text{trap } 1}(t) = \rho_B \times B_{\text{trap } 2}(t)$, can be canceled in the analysis:

$$R^{CF} = \sqrt{\frac{(q/m)_B B_{\text{trap } 1}(t_1)}{(q/m)_A B_{\text{trap } 2}(t_1)} \times \frac{(q/m)_B B_{\text{trap } 2}(t_2)}{(q/m)_A B_{\text{trap } 1}(t_2)}} \quad (4.4)$$

$$= \sqrt{\left(\frac{(q/m)_B}{(q/m)_A}\right)^2 \times \frac{\rho_B(t_1)}{\rho_B(t_2)}} = \frac{(q/m)_B}{(q/m)_A} \quad (4.5)$$

This method can be used without any additional interpolation directly on the measured data and should significantly reduce the individual jitter of the measured ratio compared to single trap analysis with the interpolation method. So far no (repeatable) improvement has been observed, which suggests that the magnetic field fluctuations are actually not correlated in the neighboring traps. The phase measurements for the reduced cyclotron frequency also do not show significant correlation, suggesting the same uncorrelated magnetic field behavior.

In the analysis for the measurements presented in this thesis, this analysis was again only used as a cross-check.

4.2 Characterization measurements

The characterization measurement often take the same or even more time than the actual measurements to reach the aimed at uncertainty in the final cyclotron frequency ratio. The aim of these measurements is, where possible, to tune out imperfections in the trapping field prior to the measurements and otherwise determine the necessary parameters and the resulting systematic shifts and uncertainties on the eigenfrequencies and ratio to sufficient precision. In general, these measurements require to scan one or more parameters, e.g. motional amplitude and tuning ratio, and the observation of the resulting shifts in one or more eigenfrequencies. For that purpose, it should be tried to optimize a characterization script to (i) measure fast to reach lower statistical uncertainty in the same time and most importantly (ii) measure and analyse in a way that reduces the effect of possible frequency drift unrelated to the intended measurement, meaning shuffle scanned values each measurement cycle and calculate results per cycle and average afterwards.

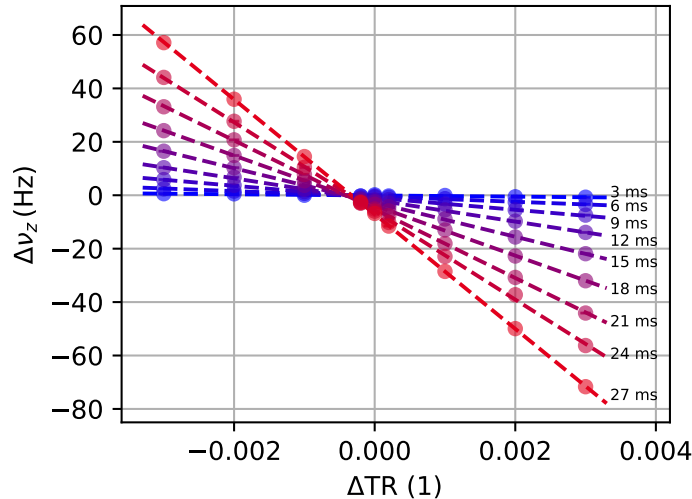


Figure 4.5: Example measurement for a simple tuning ratio optimization by determining the intersection of the different lines caused by different magnetron amplitudes. The number on the right corresponds to the duration of the excitation pulse, which results in a proportional magnetron radius. For fast tuning ratio optimization only two excitations are necessary.

4.2.1 Tuning ratio optimization

The determination of the tuning ratio (TR) is typically the first step when conditioning a new Penning trap experiment and should also be checked again after the a measurement campaign has been finished. In a poorly tuned trap, the dip signal typically does not reach the noise floor of the detection system because the ion's axial amplitude is constantly changing due to the interaction with the detection system, resulting in equally changing frequency shifts in the presence of trap imperfections, which smears out the dip.

The tuning ratio optimization tries to minimize c_4 (and c_6) by variation of the correction electrode potential, see Equation 2.39. The change in c_4 (TR) causes a linear shift in ν_z , see Equation 2.40, and with different motional amplitudes, the slope changes, see Figure 4.5. Typically, the magnetron motion is excited, since it effects the axial frequency by additional frequency shifts the least, see section 2.3. All other motional amplitudes can be considered constant.

In order to estimate and compare the trap coefficients d_4 and d_6 the same data can be used, but instead the ν_z shift dependent on the magnetron amplitude is plotted and fitted with by the function given in Equation 2.40 and c_4 and c_6 as free parameters for each set TR, see Figure 4.6. The fit results can then again be used for a fit in respect to the individual TR to extract d_4 and d_6 .

The axial shifts at high tuning ratio offsets are used to calibrate the excitation, using the d_4 from theory and the optimized tuning ratio from the simple optimization. While this is a somewhat loop-issue regarding the extraction of the d_4 and d_6 from measurements, the determination of the optimal tuning ratio is not affected by this. As an alternative, the radius calibration in the cyclotron motion can be done with the relativistic shift.

4.2.2 Odd trap potential anharmonicities

The determination of odd anharmonicities is more difficult compared to most other parameters: Modifying c_1 or c_3 can be done by applying asymmetric offset potentials, but

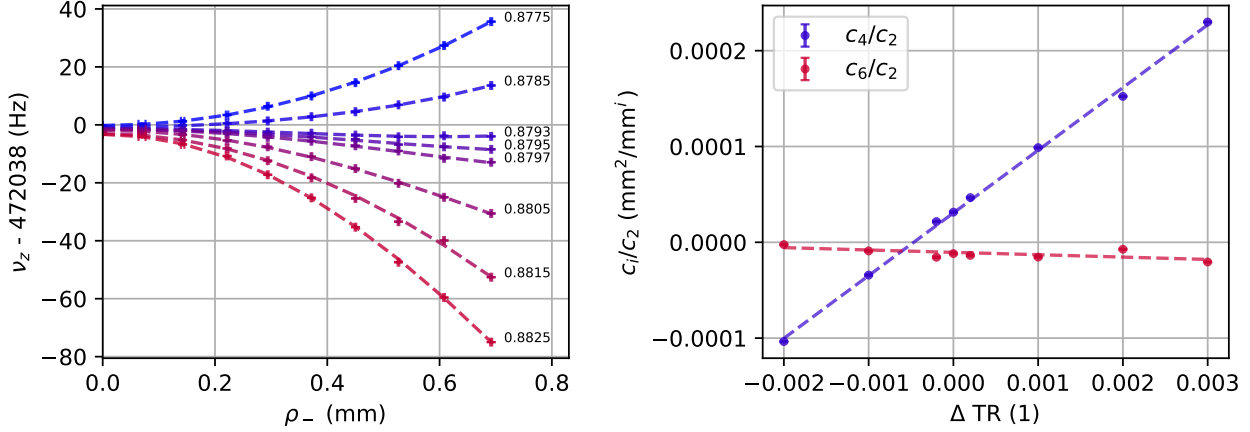


Figure 4.6: Example measurement for the determination of the optimal tuning ratio and trap parameters d_4 and d_6 . On the left the individual c_4 and c_6 are extracted for each TR. On the right, the c_4 and c_6 are compared to the used TR and the d_4 and d_6 trap parameter extracted: In this particular measurement with a $^{172}\text{Yb}^{42+}$ ion in trap 3 the results were $d_4 = -0.979(2) \cdot 10^{-3} \text{ mm}^{-4}$ and $d_6 = 37(2) \cdot 10^{-6} \text{ mm}^{-6}$ as well as a difference in optimal tuning ratios of 3.8 (25) mUnits with 0.879032 (4) and 0.87525 (25). Fortunately, the d_6 is sufficiently small even at the optimal TR for $c_4 = 0$.

their effect on the eigenfrequencies is typically too small compared to the accompanied shift by the effective c_2^2 or, in case of c_1 , do not depend on any motional amplitude.

The easiest effect to measure is the product c_3^2 , or more accurately the respective change in c_2 , which is explained in detail in ref. [79]. While this helps to optimize the trap, it cannot directly help to determine the individual parameters. On the other hand it can be used (as done in chapter 5) to estimate sizes of possible patch potentials, as well as estimate the resulting axial position changes between ions and possible magnitudes of c_1 and c_3 .

4.2.3 Magnetic field inhomogeneities

The determination of the quadratic inhomogeneity B_2 can be done with sufficient precision in a fairly simple manner: With an optimized TR and calibrated excitation radii, the shift in axial frequency is determined between a cooled ion and an ion with an excited modified cyclotron mode. In order to remove a possible shift e. g. from residual c_4 or c_6 , the resulting shift of an equal excitation of the magnetron mode should be subtracted. Ideally, this should not show any shift in axial frequency.

The determination of the linear inhomogeneity is done via shifting the ions' equilibrium position axially using asymmetric potential offsets $U_{\text{asym}} = U_{\text{LCE}} = -U_{\text{UCE}}$ on the two correction electrodes of a trap. The actual z -shift in mm is extracted from a potential simulation with the used voltages, the respective code is provided in (`fticr_toolkit/displacement.py`). For every value of U_{asym} , a reoptimization of the tuning ratio is necessary, as well as a tuning of either the trap depth or the resonance frequency to correct for the shift in axial frequency and center the dip signal again. The shift in axial frequency is predominantly caused by a change in the effective c_2 parameter and is not a systematic shift that must be corrected, since the final ν_c is not affected by it.

²As mentioned in subsection 2.3.1, these changes in c_2 do not affect the measurement results of ν_c , much in the same way as using different trap depths should not affect ν_c .

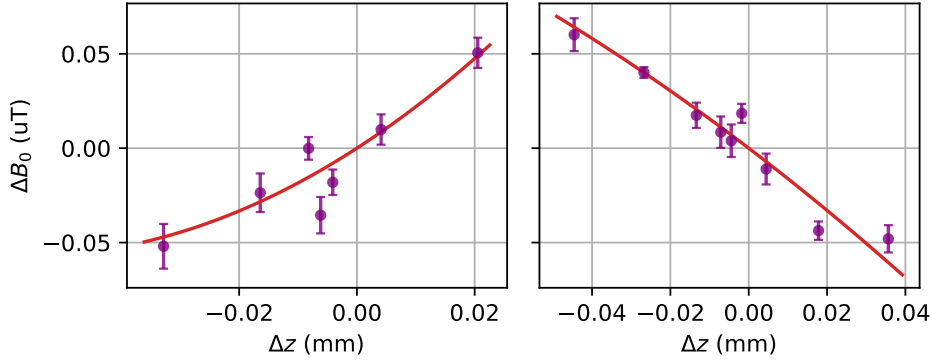


Figure 4.7: Determination of the linear magnetic field gradient B_1 by measuring the free cyclotron frequency ν_c in dependence to an axial position shift Δz in trap 2 (left) and trap 3 (right).

At each z -position (U_{asym} setting), all three eigenfrequencies are measured and ν_c determined via the invariance theorem. The resulting change $\Delta\nu_c$ in respect to Δz can be fitted with a polynom first or second order to extract the B_1 value. The B_2 from a fit can be used as an upper limit value, but is most likely of low precision compared to the method above. Two example plots are given in Figure 4.7.

These measurements have been performed occasionally over the years and the values did not change significantly for both measurement traps, even with modification of the setup in between. The last measurements resulted in $B_1 = 1.41(27) \text{ mT m}^{-1}$ and $-1.49(16) \text{ mT m}^{-1}$, for trap 2 and 3 respectively.

4.2.4 Detection system temperature

The detection system temperature T_z is in our experiment determined using the c_4 -method: A large tuning ratio offset is applied, the magnetron motion is excited and the shift in $\Delta\nu_z$ as well as the jitter $\delta(\Delta\nu_z)$ of the shift are determined. The shift is proportional to ρ_-^2 and the jitter therefore proportional to $(\delta\rho_-)\rho_-$, the amplitude distribution multiplied by the radius ρ_- . As it is shown in section 2.4, the amplitude distribution after excitation is proportional to the amplitude distribution in the cooled state. Even though the initial thermal amplitude distribution was a Maxwell-Boltzmann distribution, the excited-radius distribution can be fitted with a Gaussian to extract the width, which is due to the uniform distribution of the thermal phase in that motion.

The ρ_- can be calculated from calibration (or the measured shift here and the design d_4 and tuning ratio offset is used). With the measured $\delta(\Delta\nu_z)$ and ρ_- , the thermal ρ_- distribution can be extracted and converted to the axial amplitude distribution δz and the resonators temperature T_z , see section 2.5.

This methods and a detailed description of the calculations performed is given in ref. [94] and a detailed description of the amplitude distributions temperature determinations can also be found in ref. [96]. Another method to determine the detection systems temperature is via the relativistic shift. While it requires also a calibration, no additional detuning of the trap potential is needed. This work best with light ions and a description of this method can be found in [78] and in the soon to be published master thesis of Lucia Enzmann at PENTATRAP.

4.2.5 Axial dip measurement systematics

The ν_z fit result of the axial dip fit function is generally not independent of the other fit parameters; a discussion of this can be found in [82]. To estimate a dependence, the

fit can be performed with a specific parameter excluded from the optimization process and simply scanning it and monitoring the change in ν_z . The investigations with the measurement data presented within this thesis did not result in significant dependence on most parameters, only the ν_{res} parameter has an effect. Another possibility of characterizing this effect is now possible by actually varying the real resonator frequency in a measurement by tuning the detection system without changing the trap depth and recording numerous axial dip spectra.

With the resonator frequency known to an uncertainty of 2 Hz or better, this dip lineshape systematic [83] can still have a significant effect on the measured axial frequency. With the shifts being dependent in size to the respective ion dip widths and measurement methods, the actual investigations are made in the chapters describing the performed measurements in chapter 5 and chapter 6.

Currently in investigation is the possibility to cancel these dip-lineshape shifts, or at least suppress them stronger, by calculating the axial frequency of one ion by the axial frequency of the other using the literature mass ratio, as it is done with the magnetron frequency in the normal analysis. This could in principle transfer the dip-lineshape shift in equal strength to the other ion, allowing maximum suppression in the ratio. This should especially with the varactor tuning give solid results, since $U0$ does not change and drops out in the calculation.

4.2.6 Phase transfer function

The precision of phase-sensitive detection methods relies on a linear transfer function of the ions phase at the moment of coupling and/or readout to the measured phase $\varphi_{\text{meas}} = \varphi_{\text{ion}} + \varphi_0$. A constant offset φ_0 drops out in the phase difference (see section subsection 2.5.3). Often, this offset can depend on the ion's phase at the time of coupling: $\tilde{\varphi}_0 = \varphi_0 + \Delta\varphi_{\text{nonl.}} \sin(\varphi_{\text{ion}})$. One reason may be a partial dipole excitation of the modified cyclotron frequency when applying the (short) coupling π -pulse. The short time of the pulse, creates a rather broad signal in frequency space with potentially significant amplitude at the modified cyclotron frequency in combination with a sufficient D_z effective distance of the electrode in use [82].

In any case, the phase transfer function can be directly measured by performing a measurement much alike the N-determination measurement shown in Figure 2.17. In order to probe this effect to highest precision, one has to pick a set of short evolution times, which will result in a set of measured phase that span approximately equidistant the full 2π -range. Using only short phases below 1 s not only increases the number of measurements per time but also ensures highest phase stability and allows to predict the measured phases with low precision in the prior measured frequency. The measured phases at these evolution times are now compared to the predicted phases (both offset corrected) and the residuals can be fitted with a sinusoidal function to extract the amplitude of the nonlinearity $\Delta\varphi_{\text{nonl.}}$.

Example determinations of the phase transfer function without and with pulse shaping are shown in Figure 4.8. In this case a hanning window function is used for pulse shaping of the excitation and coupling pulses, see section 2.4.

For the calculation of the resulting frequency shift, the amplitude is considered a systematic phase uncertainty $\Delta\varphi_{\text{nonl.}}$. Since $\Delta\nu = \Delta\varphi_{\text{nonl.}}/t_{\text{evol}}$, the resulting systematic uncertainty actually reduces with higher (long) evolution time. Together with the drift of our magnetic field, the shift originating in the measured phase after the long evolution time also averages down. The same down averaging does not happen in the short evolution times phase, since there is no frequency resolution to actually resolve the change in magnetic field and the phase remains stable.

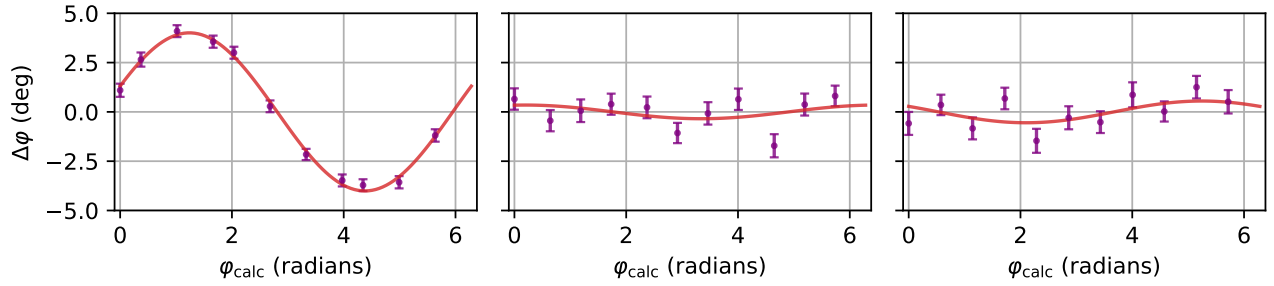


Figure 4.8: Measured phase transfer function without pulse shaping in trap 2 (left) and with pulse shaping in trap 2 (middle) and 3 (right).

Another possible shift is often actually an evolution time depended time error, also sometimes referred to as a type of phase nonlinearity because measured it looks the pretty much the same. A timing error between cyclotron excitation and coupling pulse of just 1 ns for an evolution time of 100 s is already an relative systematic shift of the measured frequency on the order of 1×10^{-11} . This offset increases with shorter evolution time. If equal for both measured ions, this effect is again suppressed in the ratio.

This effect can be mapped by performing a large amount of repeated N determination measurements up to the actual longest evolution time during the planned measurement. With sufficient number of averages, the effect might be resolved as a phase shift. Also here, a pulse shaping or a randomization of the excitation and coupling pulses might help, but technical issues should also be investigated.

4.2.7 Image charge shift

The image charge shift (ICS), see subsection 2.3.6, is in its absolute size equal for the ν_+ and ν_- frequencies, only with opposite sign. A direct determination of the magnetron frequency differences of two ions with large mass difference allows to test the estimated model behind the ICS prediction, as it was done in ref. [84] to a precision of 5%. For a more precise ICS correction of a measured cyclotron frequency ratio, the shift can be individually measured during a measurement campaign, as it was recently shown at PENTATRAN in ref. [85]. The advantage of the measurement in the magnetron frequency is, that all other systematic shifts can be calculated more precise (in a sense of an absolute frequency shift) in the slower magnetron motion than the reduced cyclotron motion. Therefore, the measured difference $\Delta\nu_-$ between two ions can be corrected without significantly increasing the uncertainty.

Still, the resolution has to be high and as it is normally used for the ν_+ determination, a phase-sensitive method has to be used for the determination of the magnetron frequencies. This was in prior measurements a difficult task, since the coupling sideband is very near to the resonance of the detection system and applying the pulse was (also in our experiment) exciting the resonator to a level that made measurements of the phase of the axial frequency hard to impossible. The test mentioned in ref. [84] circumvented this problem by using the *separated oscillating fields* method, essentially converting the phase in an amplitude signal, which was then measured by its effect on the axial frequency in the presence of a large c_4 inhomogeneity.

At PENTATRAN the mentioned effect was eliminated by using shaped coupling pulses; see section 2.4. The shaped pulse reduces the frequency width of the pulse and with that also reduces its amplitude at the resonance frequency of the detection system to a level that does not produce the prior limiting excitation.

With the magnetron difference caused by the ICS determined, an effective trap radius can be calculated as a characterization value for that specific trap and allows to correct the ICS to $< 5\%$ [85].

Chapter 5

Mass Determination of ^{20}Ne

Mass determinations in atomic mass units are ideally done with carbon as a reference, since it defines the unit. While it was planned early on to perform these kind of *absolute*¹ mass measurements at PENTATRAP [59], e. g. for the determination of the mass of ^{87}Rb for the determination of the fine structure constant [73], the measurements presented here are the first of this kind at PENTATRAP. Additionally, compared to mass-ratio determinations in the medium- to heavy-mass region, light ions will often have charge-to-mass ratios equal to or near 1/2 in order to easier match to the carbon reference ion and also to increase the signal-to-noise ratio on the detection system as much as possible with the available charge states. The increased cyclotron frequency would in principle help to improve the relative precision of the determined ratio, but systematic effects are affecting the light-mass ions typically more than the heavier ones (more to that later), making these measurements slightly more challenging regarding necessary systematic studies. Additionally, some of these systematics depend on statistically distributed parameters, such as the initial radial amplitude of an ion before PnP measurement, resulting in increased statistical uncertainty as well.

The next sections present the results of the mass determination of ^{20}Ne , contributing to the above-mentioned QED tests in collaboration with the g -factor experiment ALPHATRAP. The measurement procedure is given in section 3.3. At the time of this measurement the detection system was not yet tunable, so the axial frequencies are matched by adjusting the depth of the trap.

5.1 Ion charge state choice and production

For the determination of the mass of ^{20}Ne a near perfect doublet is available using fully ionized atoms, being $^{20}\text{Ne}^{10+}$ and $^{12}\text{C}^{6+}$. Using the current literature values [75], the charge-to-mass ratio of the two ions and therefore also the cyclotron frequency ratio is estimated to approximately $R - 1 = 3.8 \cdot 10^{-4}$. This corresponds to a fairly good charge-to-mass doublet: An equal ratio of the applied trap depths U_0 will match the axial frequencies.

Since the binding energy for the last 1s electron in neon and carbon is about 1400 eV and 500 eV [37], respectively, we can easily produce these charge states in the TIP-EBIT with a electron beam energy of 4.5 keV. The high charge-to-mass ratio of 0.5 e/u results in a cyclotron frequency of about 54 MHz in our magnetic field, which is beneficial in boosting the relative precision of the cyclotron frequency determination given constant absolute measurement precision. However, if the stability of the modified cyclotron

¹An absolute mass measurement in a sense that the result is not considered a *unit-less* mass ratios. Being perfectly accurate, the atomic mass unit is not an absolute unit, as it is defined as 1/12 of the mass of the ^{12}C atom. A *real* absolute mass measurement would be a measurement in kg or an energy unit e. g. eV.

frequency is limited by field fluctuations, this will not increase the relative statistical uncertainty.

Correction of the binding energies is in this case not a limitation to the final result: The highest uncertainties of the binding energies needed for correction are in neon and in summation over all charge states still contributes to only 0.019 eV [37], corresponding to an additional uncertainty on the final determined mass $m(^{20}\text{Ne})$ of 1×10^{-12} .

The ions are produced in the TIP-EBIT from natural neon gas and methane. One could have used carbon targets instead of methane, but the use of gaseous samples is generally preferred to solid targets and laser-ablation because of the simplicity and more stable EBIT condition: No rapid pressure increases, typically less contaminants in the ion bunch and no contamination of the EBIT surfaces and simpler and faster trigger repetitions (since the laser is designed for one pulse per second repetitions). The MIVOC inlet system [101] is used to switch between gas sources and to clean/pump the gas-inlet of the TIP-EBIT. The most efficient production / extraction of the desired ions was possible with short breeding times below 100 ms avoiding evaporative cooling, which causes the ion distribution to shift to heavier elements/isotopes from the rest gas [103].

The ion transport, catching in the trap tower, and preparation is the same for all measurements and explained in section 3.1.

5.2 Preliminary systematic considerations

The light ions present a few differences compared to our previous heavy ion measurements: The charge is comparably low with six and ten elementary charges, resulting in a reduced signal strength in the detection system. This results in smaller dip widths of the axial dip signal, which can make the fit with the dip lineshape model challenging or require longer measurement times to resolve the dip. Additionally, higher dipol excitations of the modified cyclotron motion might be necessary to obtain a sufficient signal-to-noise ratio for the phase determination using the PnP method. As a secondary effect, the thermal amplitudes after resistive cooling are larger for all eigenmotions (see Equation 2.93), again requiring stronger dipol excitation to ensure a phase imprint and also increasing the phase distribution after the dipol excitation due to the initial radius, see the PnP description in subsection 2.5.3.

The most relevant secondary effect is the relativistic shift. Due to the high cyclotron frequency and low mass, the relativistic mass increase is relatively strong, resulting (also in combination with our strong magnetic field and a B_0^2 dependence of the relativistic shift) in a dominant systematic effect.

Due to this, we decided to determine several cyclotron frequency ratios with different excitation strengths, which allows us to extrapolate to zero excitation where only the thermal radii have to be considered for the estimation of systematic effects depending on ρ_+^2 . This method has been previously introduced by the LIONTRAP experiment [21].

Since there was no varactor system at this stage of the experiment, the trapping voltage had to be adjusted for each ion to match the axial frequency with the resonance frequency of the detection system. As discussed in subsection 2.3.3, this results in a systematic shift of the determined ratio due to a shift of the axial equilibrium position z_0 caused by asymmetric patch potentials on the trap electrodes in combinations with a magnetic field gradient. The difference in the trapping voltage is approximately $\Delta U_0 = 2 - 5$ mV, depending on the resonance frequency of the detection system, which is small enough to estimate the respective uncertainty using a determined c_3 and resulting estimation of the size of the patch potentials. The varactor system provides a much easier solution for this issue for future measurement. The details of this estimate will

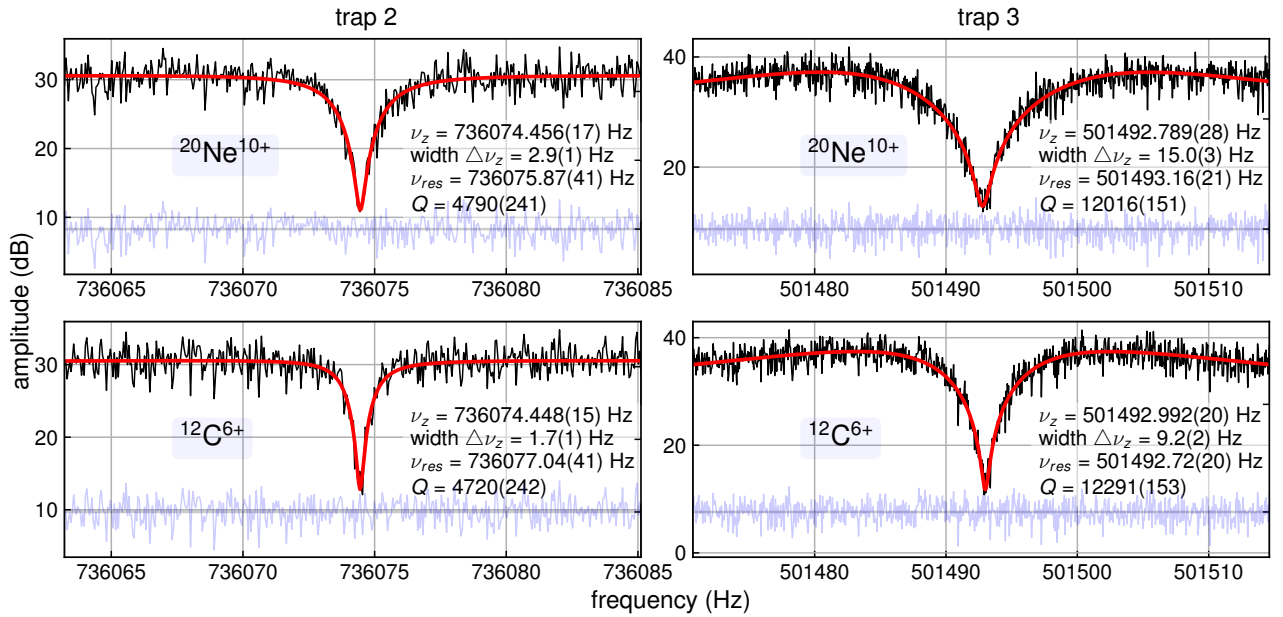


Figure 5.1: Example dip spectra (zoomed in to enlarge the actual dip region) of $^{20}\text{Ne}^{10+}$ (top) and $^{12}\text{C}^{6+}$ (bottom) in trap 2 (left) and trap 3 (right). The dip model fit is displayed as the red line and the most relevant fit results are given, with the values in the brackets representing the uncertainties of the fit parameters for that particular least square fit. The pale blue data on the bottom are the fit residuals.

be discussed near the end of this section along with all other systematic effects that are relevant for this measurement.

5.3 Cyclotron frequency ratio

The measurement sequence follows the description in section 3.3: A set of three ions is loaded in an A-B-A sequence, and the eigenfrequencies are determined roughly using the dip and double-dip method. The guess-frequencies are easily calculated using the literature masses and c_2 and B_0 determined in previous measurement campaigns. Searching for the modified cyclotron frequency with zero knowledge is a little more cumbersome. A method is described in section 3.3.

Example dip spectra are shown in Figure 5.1. The dips are centered on the resonance frequency as precisely as possible, which is limited by the determination of the resonator frequency to approximately 2 Hz, depending on the quality factor of the resonator circuit as well as possible noise structures around the resonance. Additionally, the axial frequencies of the two different ions are matched on sub-Hz level, which results in a higher confidence that both ion signals are on the same position in relation to the resonance of the detection system. The radial frequencies are determined to better than 1 Hz via the double-dip method, which will be sufficient for the later used short reference phase evolution time of only 0.1 s.

These preliminary measurements and the resulting trap settings are summarized in Table 5.1. These settings already include optimized tuning ratios determined using the method presented in subsection 4.2.1. The determination of eigenfrequencies is repeated after each reloading, and, if necessary, parameters like the trap depth or pulse settings are adjusted (marginally) due to drifts of the magnetic field or drifts of the trap potentials supplied from the StaRep to ensure a centered dip. For the majority of this measurement campaign the number of averages, different evolution times and other related settings

Table 5.1: Trap and ion properties during the neon mass measurement campaign. The values in the brackets given here are not measurement uncertainties but ranges for these values during the measurement campaign.

	Trap 2		Trap 3	
	$^{12}\text{C}^{6+}$	$^{20}\text{Ne}^{10+}$	$^{12}\text{C}^{6+}$	$^{20}\text{Ne}^{10+}$
B_0 (T)	7.002154 (5)		7.002163 (5)	
U_0 (V)	-14.9024 (1)	-14.8968 (1)	-6.9172 (1)	-6.9146 (1)
TR (1)	0.8788 (5)		0.8766 (5)	
ν_+ (MHz)	≈ 53.772656	≈ 53.792994	≈ 53.775425	≈ 53.795762
ν_z (Hz)	≈ 736074		≈ 501493	
ν_- (Hz)	5038.4	5036.1	2338.3	2337.5
ν_{res} (kHz)	736075.5 (2)		501493.0 (2)	
Q factor (1)	4750 (300)		12150 (200)	

Table 5.2: Summary of measurement settings for the N determination and main cycle. In the main cycle only the shortest and longest t_{evol} are used. The excitation amplitude was varied and the range of used settings is given. The amplitudes A for PnP pulses are the set values for the function generators, not the actual voltage on the electrodes.

Setting	Trap 2	Trap 3
N determination averages (1)		6
N determination t_{evol} (s)	(0.1, 0.25, 0.6, 1.05, 5.05, 11.05, 15.0, 20.05)	
main cycle duration (h)		12
subcycle averages (1)		10
FFT delay (ms)		1
FFT window / zero padding (s)	0.1 / 9.9	0.04 / 9.96
A_{exc} (V) / t_{exc} (ms)	0.15 – 0.6 / 1	0.2 – 0.6 / 1
$\approx \rho_{\text{exc}}$ (μm)		15 – 50
$A_{\text{coupl.}}$ (V) / $t_{\text{coupl.}}$ (ms)	1.0 / 8	1.0 / 8
pulse window function		tukey (0.5)

are not changed and summarized in Table 5.2. The measurement sequence is described in section 3.3 and will not be repeated at this point, as it is described well enough in combination with the presented measurement settings.

These settings have been optimized to reach highest phase stability at longest phase evolution times. In this measurement, the phase evolution time was limited to just 20 s, which is much less than in previous measurements of heavy highly charged ions [13, 14]. The reason for this is the relativistic *jitter*: As described in subsection 2.3.5, the strong magnetic field, high mean thermal radii (low masses) and high ν_+ (high charge-to-mass ratio) result in a jitter of the modified cyclotron frequency dominant over other frequency jitter sources. The frequency jitter results in a phase jitter, as explained in subsection 2.5.3, which increases with the phase accumulation time. This limits the accumulation time to 20 seconds, after which the measured phases can still be unwrapped with confidence.

Due to the simultaneous measurement of the long phase and the axial dip, the binning and possible averaging of the axial spectra are defined by the long evolution time and repetitions (averages) within one subcycle. Therefore, the axial spectra have a binning of 50 mHz and are averaged over 10 spectra. Each subcycle with 10 averages takes about 20 min, resulting in about 35 subcycles for a full 12 h measurement main cycle.

In Figure 5.2 example phase data and ν_z data from one complete main cycle are shown. The shown data is averaged data, meaning that each data point of phases is the average of 10 phases measured after the short reference phase accumulation time subtracted from 10 phase measured after the long phase accumulation time. The ax-

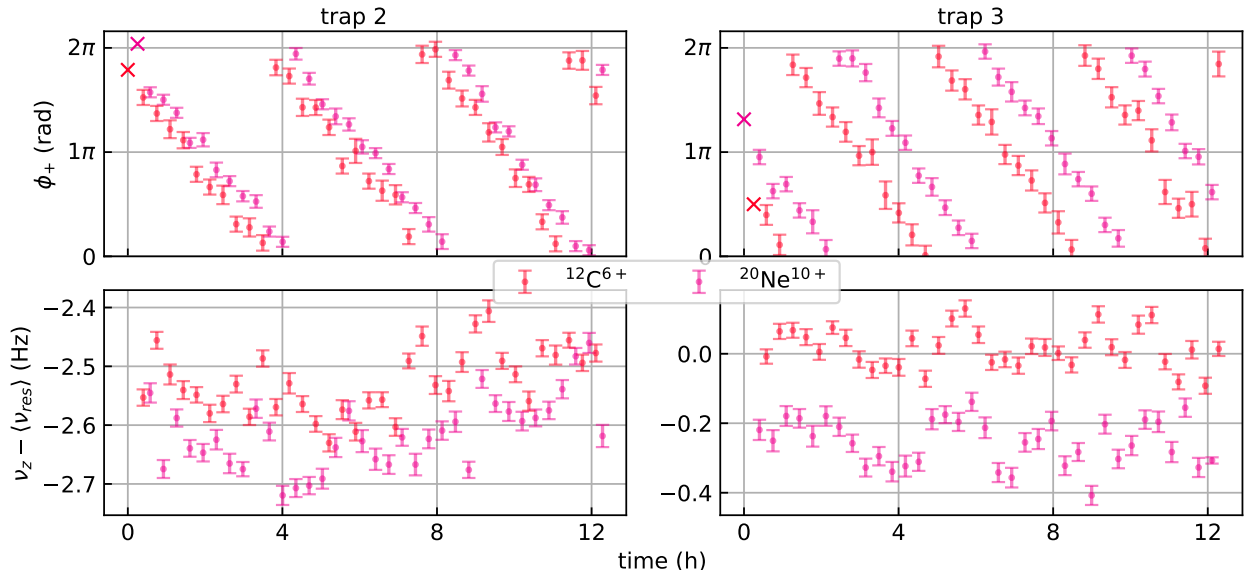


Figure 5.2: Example phase and axial fit data of measurement run #8. The upper panels show the phase data: Each value is an average of phase differences between the phases after the long accumulation time of 20 seconds and the phases after the short accumulation time of 0.1 seconds per cycle. The crosses at the beginning of the measurement data show the last value of the long accumulation time during the N determination at the beginning of a measurement run. The lower panels show the axial frequency data, determined from the averaged spectra during the long phase accumulation times of the PnP measurement via dip fit.

ial frequencies are determined from 10 averaged axial spectra, each measured during the long phase accumulation time measurement. The individual time stamps are the averages of the long accumulation time phase measurements. The continuous drift of the phase is due to the magnets drifting field strength which declines continuously. Given one full phase revolution over approximately 4 hours at the given phase evolution time of approximately 20 s, the relative magnetic field drift, which is equal to the relative cyclotron frequency drift, results in approximately $\Delta B/B/t = 2 \cdot 10^{-10} \text{h}^{-1}$ or $\Delta B/B/\text{subcycle} = 9 \cdot 10^{-11}$ from one subcycle to the next.

From the measured phases and the N -determination at the beginning of each measurement run, the absolute modified cyclotron frequency can be deduced, resulting in ν_+ values for each ion and trap for each subcycle. Considering possible errors in the N -determination, the effect on the determined frequency and ratio can be easily estimated and is specific for each measurement campaign depending on the cyclotron frequency and phase accumulation times. For this measurement campaign, if the total number of periods during the effective accumulation time ($N \approx 19.95 \text{s} \cdot 54 \text{MHz} \approx 1 \times 10^9$) is incorrect by only one period, the ratio is shifted by approximately 10^{-9} , which would be an obvious deviation. More difficult is the detection of common errors for both ions, e. g. both N determinations are missing one period. Fortunately, in this measurement this shifts the ratio only by approximately 3.5×10^{-13} , which is insignificant compared to the statistical measurement uncertainty.

For the determination of the free cyclotron frequency the invariance theorem is used. The magnetron frequency is obtained from the double-dip measurement during the measurement preparation. Due to a lack of confidence regarding the systematics of the magnetron frequency determination using the double dip method, we actually calculate the magnetron frequency of one ion from the measured magnetron frequency of the other, the trap voltage difference and mass ratios from literature. The literature mass value for ^{20}Ne and the voltage ratio are precise enough to get an accurate magnetron frequency ratio. The absolute accuracy of the magnetron frequencies is close to irrelevant

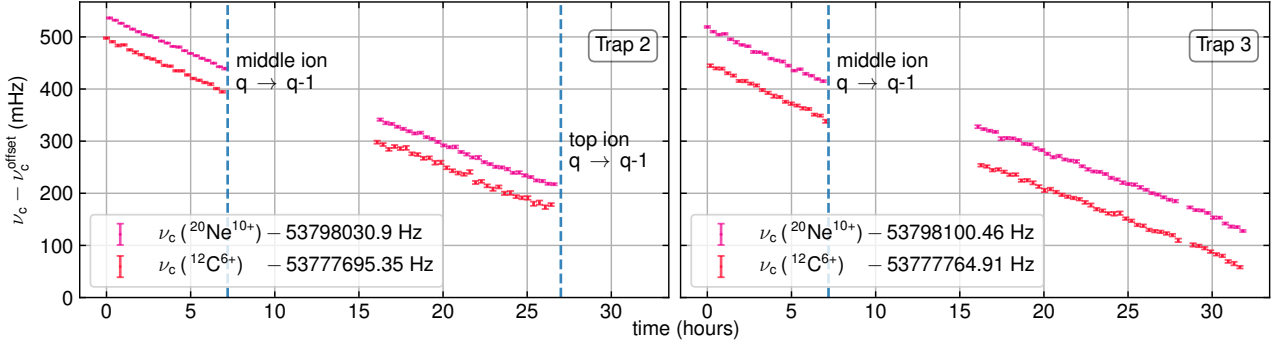


Figure 5.3: Example free cyclotron frequency data of measurement run #10 and #11. Charge exchanges due to interaction with rest gas limit the life time of the ions, resulting in data loss for one or both traps and require a reloading of the ion set.

for the determined ratio using the invariance theorem as long as the magnetron frequency ratio is accurate. An example of ν_c data is shown in Figure 5.3. The gaps in the measurement data are due to one of the following reasons:

- **Charge exchange** of the trapped ions with residual gas atoms happen for one of the three ions about once per day. The resulting lesser charged ion is either lost, possibly by the recoil, or has just very different eigenfrequencies and is not visible as a dip signal on the resonator anymore. This could be counteracted by implementing a cryogenic valve above the trap tower to prevent gas inflow from the room-temperature beamline section.
- Strong magnetic **field instabilities**, which can occur due to other experiments in the experimental hall ramping magnets or the ceiling crane being used [109], can cause strong enough jumps in the data, making an unwrap of the phases impossible. This is monitored using external magnetic field sensors and the data is discarded.
- **Additional ions** that have not been removed during cleaning start interacting with the ion of interest. Although cleaning measures are applied during the measurement preparation (see section 3.3), to ensure single ions in each trapping potential, additional ions are occasionally still present during the measurement run. Because these ions were not detected during preparation, they either have a very different charge-to-mass ratio or, more likely, are additional neon or carbon ions on high cyclotron radii, initially not interacting with the ion of interest. Due to repeated broadband sideband coupling during the measurement, it can happen that the radius reduces and the contamination ion starts to interact with the original ion, which causes the phase measurement and axial dip to become unstable. If this is observed, the data of the complete measurement run is discarded.

The determination of the cyclotron frequency ratios $\mathcal{R}^{\text{CF}} = \nu_c(^{20}\text{Ne}^{10+}) / \nu_c(^{12}\text{C}^{6+})$ is done by interpolation method as explained in section 4.1. The statistical shot-to-shot jitter of \mathcal{R}^{CF} (about 7×10^{-11}) is caused by the relativistic jitter mentioned above. Determinations by the polynomial method are made as a cross-check, but not used for final ratio determinations. Figure 5.4 shows all determined \mathcal{R}^{CF} in this measurement campaign, as well as averaged results of each full or partial main cycle and the total averaged results per trap. The simply averaged trap ratio results are $\mathcal{R}_{\text{trap2, average}}^{\text{CF}} = 1.000\,378\,141\,781(3)$ and $\mathcal{R}_{\text{trap3, average}}^{\text{CF}} = 1.000\,378\,141\,787(4)$, with $\chi_{\text{red}}^2 = 0.83$ and 0.80 for traps 2 and 3, respectively. These results averaged over all used excitation amplitudes are only given for completeness, see next section.

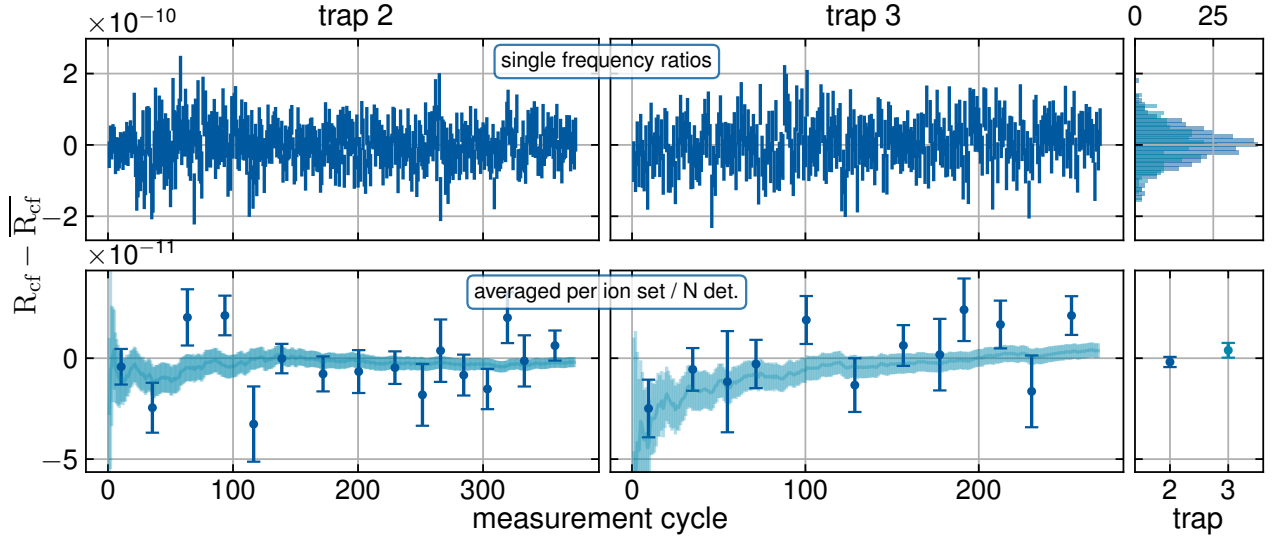


Figure 5.4: All determined \mathcal{R}^{CF} during the neon campaign from both traps. The upper panel shows all individual determined ratios per subcycle and the respective histograms in the figure on the right. The lower panels show the determined ratios per full or partial main cycle and the evolution of the statistical error of the mean ratio and the final mean ratio values per trap in the figure on the right. The averaged results here are just for demonstration, see text.

5.4 Extrapolation to zero excitation amplitude

As mentioned above, the use of different excitation amplitudes was done to reduce the final systematic uncertainty due to systematic shifts proportional to ρ_+^2 (mainly due to the relativistic mass increase). For each trap, about six different settings are used and data acquired to reach a relative precision of approximately 5×10^{-12} to 10×10^{-12} for each cyclotron frequency ratio. The results are shown in Figure 5.5. In contrast to the method deployed at the *Liontrap* experiment, where excitation amplitudes are also varied between ions in one measurement [21], here both ions always get the same excitation strength. This allows us to perform a simple two-dimensional fit of ratio values in dependence of the squared excitation amplitude, instead to the area fit applied at LIONTRAP. This method requires less data and measurement time to reach sufficient statistical uncertainties, but some requirements are set on the relation of the excitation radii of the two ions to each other. Using Equation 2.36 and Equation 2.63 the dependency of \mathcal{R}^{CF} on the excitation radii ratio $R_\rho = \rho_{+,B}/\rho_{+,A}$ is:

$$\begin{aligned}
 \Delta \mathcal{R}_{\text{rel.}}^{\text{CF}} &\approx \mathcal{R}_{\text{meas}}^{\text{CF}} \left[\frac{\Delta \omega_{c,B}}{\omega_{c,B}} - \frac{\Delta \omega_{c,A}}{\omega_{c,A}} \right] \approx \mathcal{R}_{\text{meas}}^{\text{CF}} \left[\left(\frac{\omega_{+,A} \rho_{+,A}}{2c} \right)^2 - \left(\frac{\omega_{+,B} \rho_{+,B}}{2c} \right)^2 \right] \\
 &= \mathcal{R}_{\text{meas}}^{\text{CF}} \left(\frac{\rho_{+,A}}{2c} \right)^2 \left[\omega_{+,A}^2 - \omega_{+,B}^2 R_\rho^2 \right] \\
 &\approx \mathcal{R}_{\text{meas}}^{\text{CF}} \left(\frac{\omega_{+,A} \rho_{+,A}}{2c} \right)^2 \left[1 - \left(\mathcal{R}_{\text{meas}}^{\text{CF}} R_\rho \right)^2 \right].
 \end{aligned} \tag{5.1}$$

All approximations are based on the frequency hierarchy or approximating the ν_+ ratio to $\mathcal{R}_{\text{meas}}^{\text{CF}}$. This shows, that the resulting systematic shift of the cyclotron frequency *ratio* is strongly suppressed in comparison to the shift in the individual cyclotron frequencies. For equal radii after excitation $R_\rho = 1$, the suppression factor is $1 - \mathcal{R}_{\text{meas}}^{\text{CF}}$, which is in case of this measurement $4 \cdot 10^{-4}$. More importantly, the relation is proportional to $(\omega_{+,A} \rho_{+,A})^2$, even with an $R_\rho \neq 1$ as long as it is constant. Given that the reached motional amplitude after a dipolar excitation is proportional to the duration

Table 5.3: Relative systematic corrections and their uncertainties on \mathcal{R}^{CF} at PENTATRAN after the extrapolation to zero-excitation amplitude for both traps. All values are given in parts per trillion (10^{-12}).

Effect (parameters)	Trap 2	Trap 3
$T_z (B_2, C_3, C_4, C_6)$	-0.8 (0.3)	-1.7 (0.5)
Magnetron frequency	0.0 (0.5)	0.0 (0.5)
Non-linear phase read-out	0.0 (1.0)	0.0 (1.9)
Position difference	0.0 (1.0)	0.0 (0.8)
Dip lineshape	0.0 (1.0)	0.0 (1.8)
Image charge shift	19.5 (1.0)	19.5 (1.0)
Total	18.7 (2.1)	17.8 (3.0)

Table 5.4: Thermal amplitudes of the different ions in trap 2 and 3, respectively. The results differ between traps due to the different eigenfrequencies.

	Trap 2		Trap 3	
	$^{12}\text{C}^{6+}$	$^{20}\text{Ne}^{10+}$	$^{12}\text{C}^{6+}$	$^{20}\text{Ne}^{10+}$
T_z (K)	7 (2)			
$\langle z_{0,\text{thermal}} \rangle$ (μm)	18.9 (30)	14.7 (25)	27.6 (40)	21.5 (35)
$\langle \rho_{\pm,\text{thermal}} \rangle$ (μm)	2.2 (3)	1.7 (3)	2.7 (4)	2.1 (3)

the thermal amplitudes, the effective temperatures of the detection systems are measured, using the c_4 -method described in subsection 4.2.4. With these measurements the detection systems show an average temperature of 7(2)K.

The even higher-order electric field coefficients c_4 and c_6 can be sufficiently estimated from the uncertainty of the tuning ratio and the trap design values of d_4 and d_6 , see section 3.2.2. The tuning ratios have been determined to approximately 5×10^{-4} mUnits, see Table 5.1. An example tuning ratio scan during this campaign can be found in Figure 5.6a. With the systematic shifts now being calculated only from thermal amplitudes, the shifts originating from the higher-order even coefficients c_4 and c_6 can be neglected in both traps being below 1×10^{-12} on the extracted ratio. Still, they are included in the summarized shift in Table 5.3.

The temperature and tuning ratio determinations are typically done by magnetron excitation, in order to avoid an additional shift due to B_2 , but also some measurements were performed using cyclotron excitation as a comparison, agreeing with the given uncertainties. Additionally, the measurements allowed one to extract calibration factors for the cyclotron excitation. B_1 has been determined with the method described in subsection 4.2.3. An example fit is given in Figure 5.6b. The B_2 has been simply determined for each trap by excitation of ν_+ to a specific radius ρ_+ and determining the axial frequency shift at the optimal tuning ratio.

Especially relevant for this measurement is an estimation of the difference of the equilibrium position for the both ions in each trap, to estimate the effective ratio shift due to B_1 . A measurement of c_1 was *not* performed, but a measurement of $c_1 c_3$ was performed using the method described in subsection 4.2.2, see Figure 5.7a. The result is used as a sanity check for the size of possible patch potentials and for the estimation of the difference in axial position, I used a Monte Carlo simulation of 500

Table 5.5: Higher order field coefficients extracted from characterization measurements.

	Trap 2	Trap 3
B_1 ($\frac{\text{mT}}{\text{m}}$)	1.41 (27)	-1.49 (16)
B_2 ($\frac{\text{mT}}{\text{m}^2}$)	64 (5)	22 (5)

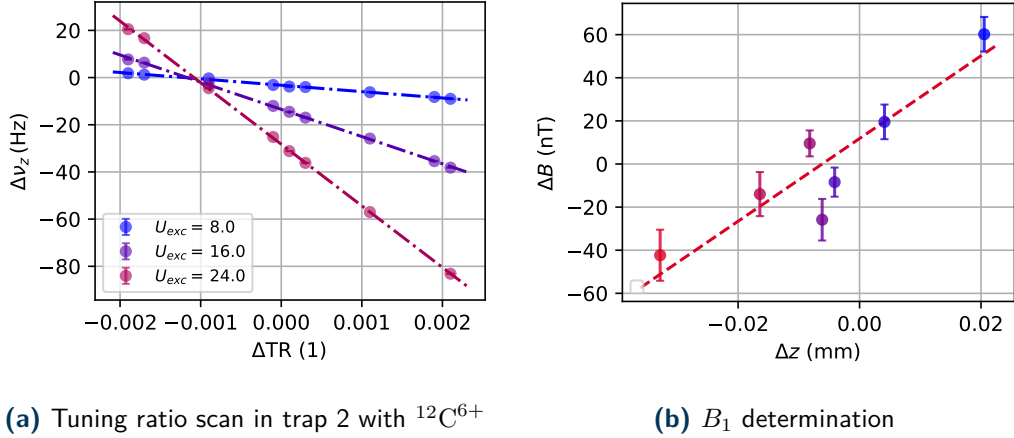


Figure 5.6: (a) Simple tuning ratio determination via excitation of the magnetron motion, scanning the tuning ratio and measuring the shift in axial frequency. Each data set and fit correspond to one excitation strength, defining the magnetron radius. The intercept point is used to extract the optimized tuning ratio with $c_4 = 0$. (b) Determination of the linear magnetic field gradient B_1 by applying asymmetric potentials $\Delta U_{UCE} = -\Delta U_{LCE}$ on the correction electrodes to shift the axial equilibrium position of the ion. The effective change in z -position is determined from simulating the respective potential. All eigenfrequencies are measured in order to extract the free cyclotron motion and using literature mass and charge values the probed magnetic field strength. The red line is a fit.

simulated potentials from trap towers with randomly varied electrode lengths³ and radii according to twice the machining precision and additional random patch potentials on all electrodes with $U_{patch} = 0(100)$ mV. For each simulated tower the voltage settings of the two positions for $^{20}\text{Ne}^{10+}$ and $^{12}\text{C}^{6+}$ are applied (including patch potentials) and the difference in potential minimum is determined, see Figure 5.7b. This way a conservative uncertainty on the position difference of the two in our traps is extracted, resulting in $\Delta(\Delta z)_{\text{trap } 2} = 0(5)$ nm and $\Delta(\Delta z)_{\text{trap } 2} = 0(4)$ nm for trap 2 and 3, respectively. These positional differences correspond to the direct δz caused by c_1 independent of the motional amplitudes, see Equation 2.42. The positional shift due to c_3 (or rather the change in c_3), see Equation 2.43, using thermal amplitudes as well as the shift in axial frequency are negligible in the cyclotron frequency ratio.

Magnetron frequency The magnetron frequency is measured only occasionally during a campaign (mostly to ensure that sideband cooling is working properly). The measurement of the magnetron frequency via the double-dip method is also not very precise, and we conservatively assign an uncertainty of 1 Hz. Given the low statistics, the uncertainty is also treated as a systematic uncertainty. The impact on the free cyclotron frequency determined by the invariance theorem is still relatively low with 2×10^{-12} due to the maximized frequency hierarchy in this measurement of ions with charge-to-mass ratio of $0.5e/u$. This can easily be reduced by calculating the difference of magnetron frequencies from theory with the literature mass ratio as an input and use only one measured magnetron frequency. The uncertainty of 0.5×10^{-12} is still very conservative in this case.

Non-linear phase read-out The non-linear phase transfer in our setup was investigated during another measurement campaign, the results are shown in subsection 4.2.6.

³Be careful to also vary the length of the electrode gaps (sapphire ring thickness), the potential is surprisingly sensitive on these.

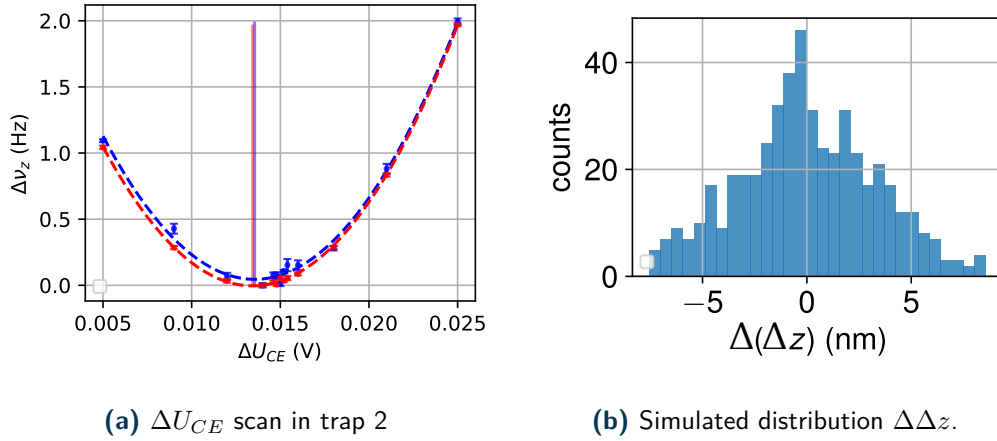


Figure 5.7: Investigation of the effect of patch potentials and machining errors. (a) Changing axial frequency of a $^{12}\text{C}^{6+}$ and $^{20}\text{Ne}^{10+}$ during an asymmetric ΔU_{CE} scan in trap 2. The minima, marked with the vertical lines, correspond to $c_3c_1 = 0$ and the corresponding ΔU_{CE} is used to estimate the size of patch potentials. The precision of the determined minimum is 0.5 mV (b) Simulated distribution of the potential minimum difference $\Delta\Delta z$ in trap 2 between $^{12}\text{C}^{6+}$ and $^{20}\text{Ne}^{10+}$ for multiple trap towers with random variations in electrode lengths applied corresponding to twice the machining tolerances as well as random patch potentials normally distributed around 0(100) mV. More details see Text.

During this measurement campaign, pulse shaping was applied for the PnP excitation and coupling pulses. With pulse shaping, the measured amplitude of non-linearity is within its uncertainty, agreeing with 0. The given estimate for the systematic uncertainty is based on the statistical uncertainty of the amplitude determination.

Dip lineshape error The dip lineshape error in this measurement is slightly relaxed, due to tuning the axial frequencies and matching them for the two ions, resulting in strongly correlated systematic shifts for the two ions. The different dip widths still result in different dip lineshape systematics, which have been investigated by scanning a fixed resonator frequency in the dip fit routine. This way, the dependency on the resonator frequency can be estimated conservatively, since an actual resonator shift is additionally adjusted in the full fit routine.

The axial frequencies follow a linear trend in this scan, as shown in Figure 5.8. The difference in the two ions linear dependencies of the axial frequency on the resonator frequency multiplied with a conservative uncertainty of 5 Hz on the resonator frequency is used to calculate the effective shift on the cyclotron frequency ratio given in Table 5.3.

Image charge shift The image charge shift is easily calculated from an analytical estimate, see Equation 2.66. With the analytical estimate experimentally verified to a level of 5%, this precision is also used as an uncertainty for the ratio shift. All other parameters are known to higher precision.

Corrected ratio Given these shifts and the cyclotron frequency ratios determined in the extrapolation fit, the following results for \mathcal{R}^{CF} are acquired with the values in the parenthesis being the statistical, systematic and total uncertainties, respectively:

$$\begin{aligned}\mathcal{R}_{\text{Trap } 2}^{\text{CF}} &= 1.000\,378\,141\,803\,(4)(2)(5), \\ \mathcal{R}_{\text{Trap } 3}^{\text{CF}} &= 1.000\,378\,141\,798\,(8)(3)(9).\end{aligned}$$

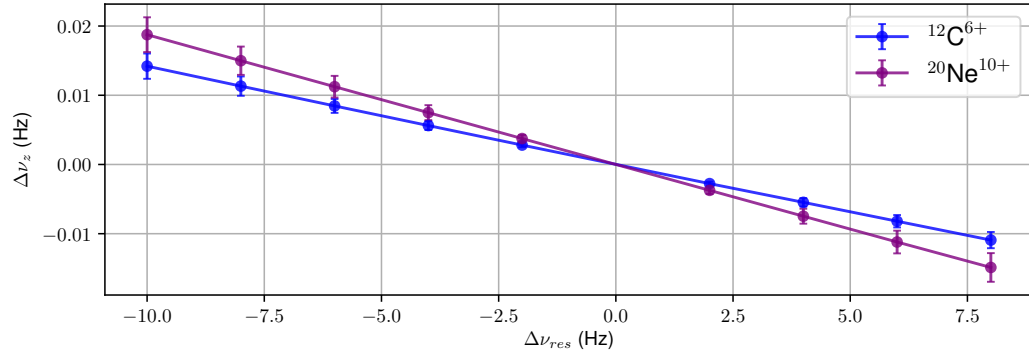


Figure 5.8: Axial frequency ν_z determined via dip fit with fixed resonator frequency ν_{res} scanned around the ν_{res} determined from a free fit for both ions in trap 2. Only the difference of these two slopes has to be considered for the systematic uncertainty since the matching of axial frequencies is generally better than 0.5 Hz.

The systematic shifts are assumed to be uncorrelated between traps. With one exception being the magnetron frequency uncertainty which is negligible in comparison to the others. Given the near double uncertainty, the measurement result from trap 3 can rather be considered a cross-check than a significant contribution to the measurement result. However, the weighted mean of the two traps yields $\mathcal{R}_{\text{mean}}^{\text{CF}} = 1.000\,378\,141\,802(4)$.

5.6 Atomic mass of neutral ^{20}Ne

The neutral mass $m(^{20}\text{Ne})$ is determined, using Equation 2.29, by adding the masses of the missing electrons and their corresponding binding energies [35, 37] with an additional uncertainty of 2×10^{-11} u resulting in

$$m(^{20}\text{Ne}) = 19.992\,440\,168\,77(9) \text{ u}.$$

The relative uncertainty of this mass determination is 5×10^{-12} and represents the most precise mass value *in atomic mass units* to my knowledge to date. Interestingly, this value deviates by 4σ , or in relative terms 3.2×10^{-10} , from the current literature value, see Figure 5.9. The literature mass value $m(^{20}\text{Ne})_{\text{lit.}} = 19.992\,440\,175\,25(165) \text{ u}$ [75] is based mainly on a measurement performed at the University of Washington (UW).

5.7 g -factor of hydrogenlike $^{20}\text{Ne}^{9+}$

The motivation behind this measurement, the comparison of the determined g -factor of the bound electron of $^{20}\text{Ne}^{9+}$ to theory, see Table 5.6, allows for a cross-check using the $\Gamma = \nu_L/\nu_c$ determined at ALPHATRAP at a level of 1×10^{-10} . The newly measured mass value fits the theoretical g -factor within one standard deviation [31], while the old mass value results in a 3σ deviation from the theoretical g -factor. This, as well as other measurements made at the Liontrap experiment [121, 122] also showing significant differences from the measurements performed at UW, gives additional confidence in the accuracy of the presented results. With the g -factor comparison limited by the experimental uncertainty, the accuracy of the mass measurement could be tested to higher precision by improving the precision of the Γ determination by up to one order of magnitude to match the theoretical uncertainty.

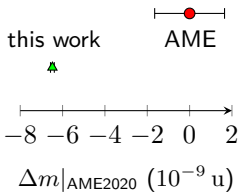


Figure 5.9: New mass value compared to AME2020-value.

Table 5.6: The measured Γ with the ALPHATRAP setup for $^{20}\text{Ne}^{9+}$ is given including the statistic and systematic uncertainties from [31]. The measured and theoretical g -factors are shown with combined uncertainties. For the g -factor the current CODATA m_e and $m(^{20}\text{Ne})$ determined in this work are used. The mass is corrected in respect to the hydrogenlike state using literature binding energies [37]. Individual contributions to the BS-QED g -factor are listed below with their respective uncertainty from theory calculations.

Γ	4045.837 341 56 (34)(13)
g_{exp}	1.998 767 276 99(19)
g_{theo}	1.998 767 277 11(12)
Dirac (relativistic point nucl.) [123]	1.996 445 170 90
Free-electron QED [36]	0.002 319 304 35
BS 1-loop Self energy [124–126]	0.000 002 717 05
BS 1-loop Vacuum polarisation [80]	- 0.000 000 063 22
BS 2-loop [80]	- 0.000 000 003 17(12)
BS 3-loop [127]	0.000 000 000 03
Recoil [80]	0.000 000 146 41
Size [80]	0.000 000 004 76 (1)

Given the much lower relative precision of the Γ measurement, the question could arise as to why the mass was measured so precisely. The first reason is that with the Γ determination at ALPHATRAP the g -factor comparison had a significant discrepancy and with the literature mass value of ^{20}Ne being one possible source of error, we were asked to measure its mass preferably with the same precision as the current literature value or better. The second reason then to improve the uncertainty even further was the question of how well the PENTATRAP experiment performs in the low-mass regime, especially against the atomic mass unit defined by $1/12$ of the mass of ^{12}C . These mass measurements in atomic mass units are also relevant for upcoming mass measurements related to QED tests, electron mass determinations, or measurement of the fine structure constant α .

Chapter 6

Ytterbium Mass-Ratio Determinations

In this chapter, the procedure and results of the determination of *nuclear* mass ratios between the five stable even ytterbium isotopes ($Z = 70$ and $N \in \{98, 100, 102, 104, 106\}$) will be discussed. First, the ion production is briefly presented, followed by some preparatory systematic uncertainty estimations. After an overview of the measurement settings and some measurement data examples, this chapter is concluded with a discussion of the systematic corrections, including the comparison of determined binding energies with theoretical values as a method cross-check, and the final results of mass ratios.

6.1 Ion production anwithring choices

The ions are produced with the TIP-EBIT ion source [104]. For the ytterbium measurement campaign, a single target was prepared with five positions, each containing an isotope-enriched sample of ytterbium oxide fixed with PLA, see figure Figure 6.1. For laser ablation, a frequency-doubled Nd:YAG laser with 7 ns pulse duration and a wavelength of 532 nm is used. The laser is guided through a vacuum viewport on the target and can be positioned via a stepper motor controlled mirror to hit a single position for isotope-selective ion production. The laser power applied per shot for ablation is around 0.1 mW to 0.5 mW, attenuated from the default laser pulse power of approximately 15 mW by a rotate-able $\lambda/4$ -waveplate and a polarizing beam splitter. The optimal power is a compromise of sufficient ablated material and as low as possible increase of the pressure inside the EBIT, which reduces the charge breeding efficiency and maximal reachable charge states.

Since the laser is optimized for a repetition rate of 1 Hz, this also defines the minimal breeding time of the EBIT, which was used here¹. The voltage of the center drift tube of the EBIT was 4.5 kV, with a cathode voltage of -1 kV which results in an electron beam energy of about $E_{\text{kin}} = 5.5$ kV. This would allow in principle the ionization of Yb to the charge state $56+$ after sufficient breeding time. This maximum charge state is populated in very small quantities because of recombination processes in the plasma. A general rule of thumb is that the maximum of the charge distribution of an element in the EBIT after reaching an equilibrium state corresponds to a charge state with an ionization energy of approximately $E_{\text{kin}}/2.3$. In the case of Yb that would be the charge state $42+$. This fits perfectly, since this charge state and the direct neighbors allow us to pick charge-to-mass doublets for the mass-ratio determinations of $A = 172$ relative to $A = 168$ and to $A = 176$, see Table 6.1. Other doublets in that quality exist only for $A = 170$ relative to $A = 174$, and for odd ratios only in lower charge states and

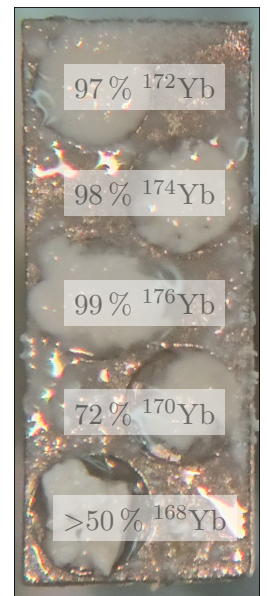


Figure 6.1: Target holder for the TIP-EBIT for five samples, $2 \text{ mm} \times 5 \text{ mm}$, each position with isotope-enriched ytterbium oxide mixed in liquid PLA. The target is backed next to harden the PLA for use in vacuum.

¹One can trigger multiple ejections between laser shots to reduce the effective breeding time, but the minimal extraction frequency of the real ion bunch will still be 1 s

Table 6.1: Approximate values for the cyclotron frequency ratios and tuned parameters $|\Delta U_0|$ or $|\Delta\nu_z|$ for a resonator at around 700 kHz planned for the ytterbium measurement campaign. The doublet measurements have been done first, before the upgrade of the detection system with varactors. The binding energy determinations are an additional cross check of the measurement scheme.

topic	ion _A	ion _B	$ R - 1 $	$ \Delta U_0 $ (mV)	$ \Delta\nu_z $ (kHz)
mass ratios	$^{172}\text{Yb}^{43+}$	$^{168}\text{Yb}^{42+}$	2.4×10^{-5}	0.63	-
doublets	$^{172}\text{Yb}^{43+}$	$^{176}\text{Yb}^{44+}$	2.4×10^{-5}	1.17	-
	$^{172}\text{Yb}^{42+}$	$^{168}\text{Yb}^{42+}$	0.023	-	8.29
mass ratios	$^{172}\text{Yb}^{42+}$	$^{170}\text{Yb}^{42+}$	0.012	-	4.11
same U_0	$^{172}\text{Yb}^{42+}$	$^{174}\text{Yb}^{42+}$	0.012	-	4.04
	$^{172}\text{Yb}^{42+}$	$^{176}\text{Yb}^{42+}$	0.023	-	8.02
	$^{172}\text{Yb}^{41+}$	$^{172}\text{Yb}^{42+}$	0.024	-	8.49
Binding energies	$^{172}\text{Yb}^{42+}$	$^{172}\text{Yb}^{43+}$	0.023	-	8.29

inaccessible higher charge states. The odd ratios were initially planned to be measured as well, but since the predicted precision of isotope shift spectroscopy for these isotopes was not very promising, they were last priority and finally not measured.

Since the charge state 42+ has a *closed-shell* electron configuration $[\text{Ar}]3d^{10}$, it was also considered a beneficial charge state with respect to the possible precision of the theoretical calculations of binding energies necessary to correct the cyclotron frequency ratios to the neutral mass ratios.

The *default* procedure for the determination of cyclotron frequency ratios at PEN-TATRAP involves tuning the trap depth to adjust the axial frequencies of both ions to match the *fixed-frequency* detection system. This is trivial for the determination of metastable state energies and low energy decay Q -values, because their mass differences are typically so small that the axial frequencies sufficiently match at the same trapping potential [13–15, 128]. When determining mass ratios of larger charge-to-mass ratio differences, it is necessary to use different trap depths for the two ions involved to match the resonance frequency of the detection system, which in turn can lead to dominant systematic uncertainties due to trap asymmetries and magnetic field inhomogeneities [11], see subsection 2.3.2. The systematic shift, or rather the uncertainty, can be determined equally to the method applied in the neon campaign. However, with a higher difference in trap depth, the uncertainty increases as well.

For use in the King plot analysis, it is typically beneficial to measure direct neighbors, since some of the spectroscopy isotope shift determinations are measured directly as frequency differences, and these are typically of neighboring isotopes. Each combination of results to form a different pairing results in an increase in uncertainties, reducing the quality of the linearity check. Mass-ratio measurements of neighboring isotopes normally require large trap potential differences to match the axial frequencies of the two ions because no near charge-to-mass doublets can be formed. This in turn results in higher systematic uncertainties due to our B_1 and is therefore discarded.

As mentioned above, the available charge-to-mass doublets around the given charge states are available for pairings of even ytterbium isotopes with mass difference of 4 u. These would result in only three relevant cyclotron frequency ratios and additionally in an unsatisfactory pairing. Better pairing would be measurements against one single reference isotope: Using e. g. the isotope $A = 172$ as a reference would allow combining two measured ratios to extract an inverse mass difference of neighboring isotopes:

$$\mathbf{w}^{A,A'} = \hat{m}_{172}/\hat{m}_A - \hat{m}_{172}/\hat{m}_{A'} = \hat{m}_{172}\mu_{A,A'}, \quad (6.1)$$

with the inverse mass ratio $\mu_{A,A'}$ defined in Equation 1.4. The reference mass \hat{m}_{172} is still a prefactor here, but since this will only scale both axes of the King plot equally, it will not affect the linearity check. While this gives some flexibility regarding possible pairings, the uncertainty of these combinations will be higher by a factor of $\sqrt{2}$ compared to direct measurements.

However, this requires the measurement of at least two even isotopes with a mass difference of 2 u. In order to circumvent the trap tuning, it was decided to upgrade the detection system with a controllable capacitance, allowing to tune the resonance frequency. With this upgrade, it is also possible to measure isotope ratios in equal charge states, reducing the impact of theoretical binding energies on the final result, since the difference in binding energy between the two isotopes is negligible (see Equation 2.31). This method was already introduced in ref. [21]. However, the necessary range, see Table 6.1, is about two orders of magnitude higher. As described in section 3.2.2, our detection systems are now tunable via variable capacities over a range of at least 10 kHz² (trap 3) and 12 kHz (trap 2), allowing us to bridge the differences in axial frequencies given in the table.

Using the tunable detection system, the binding energy of an outer electron in a highly charged ytterbium ion can also be determined with high precision by using the same isotope in consecutive charge states, e. g. $^{172}\text{Yb}^{41+}$ and $^{172}\text{Yb}^{42+}$. The advantage compared to charge-to-mass doublet measurements is (i) that no isotope shift has to be considered and (ii) that the literature mass value does not need to be as precise as the necessary isotope mass ratio in the doublet case, see Equation 2.32 and Equation 2.29. The tunable detection system is used again to overcome the difference in axial frequency, see Table 6.1, without tuning the trap depth.

Comparison of the determined electron binding energies with the respective calculated values from the group of Z. Harman (MPIK), especially Chunhai Lyu, acts as a cross-check of the measurement method and systematics, since these theoretical values are the most precise references, which we can compare to. For that purpose, the binding energies of the most outer electrons of the charge states $^{172}\text{Yb}^{41+}$ and $^{172}\text{Yb}^{42+}$ are determined. The theoretical binding energies for these electrons are 2035.4(1) eV and 3444.8(1) eV, respectively [129].

Additionally, if the measurements are trusted, the comparison can also be seen as a possible test of the theoretical calculations. This will not yield the most stringent test of QED but the measurement precision could be enough, for the first time with mass measurements alone, to test already sizeable contributions to the calculated binding energies, e. g. Breit and electron-correlation effects, which are on the order of 1 eV [129].

6.2 Mass-ratio determinations with detection system tuning

Preparatory estimations Considering the systematics, the measurements with resonance tuning suffer less from shifts due to axial displacement, since the trap depth does not have to be tuned. Furthermore, the high mass of the isotopes will result in lower thermal amplitudes compared to the light ion case above, which are additionally very equal for two ions, further suppressing systematic effects. Due to the rather high value of $R - 1$, some of these still play a role, especially the relativistic mass increase, see Figure 6.2. Given the size of the shifts, a small enough excitation radius would not require an extrapolation to zero excitation amplitude as it was done in the neon measurement campaign, see Equation 5.1.

²This range can be slightly increased without upgrading the tuning system by using a voltage supply that can deliver a potential between -1 V and 20 V with sufficient stability.

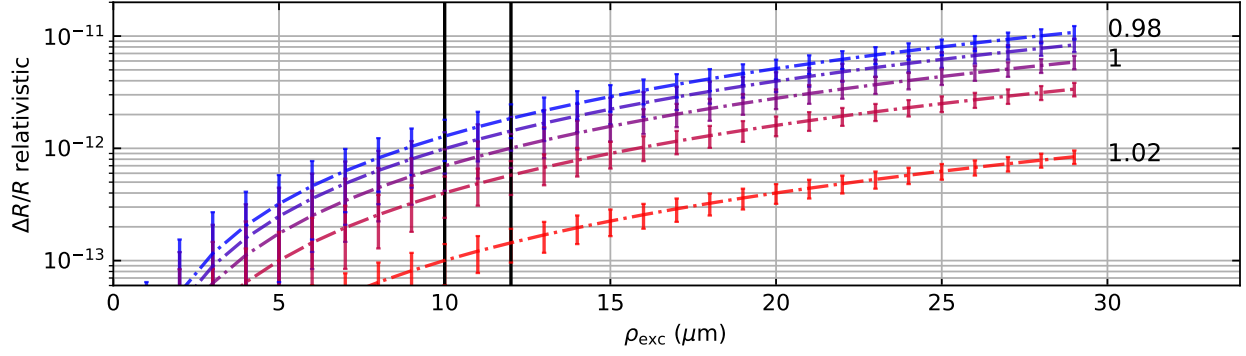


Figure 6.2: Size of the systematic shift on the measured ratio of the two ions $^{172}\text{Yb}^{42+}$ and $^{176}\text{Yb}^{42+}$ caused by the relativistic mass increase in dependence of the excitation amplitude used during the PnP measurement scheme. Additionally, the ratio between the excitation radii $\rho_\rho = \rho_{+,176}/\rho_{+,172}$ is scanned from 0.98 to 1.02 as annotated on the right. Approximately the inverse of the cyclotron frequency ratio R^{CF} minimizes the shift. The excitation radii used are marked with the vertical black lines. For more details, see text.

With the thermal radii of $\rho_\pm \approx 0.7 \mu\text{m}$ and $\rho_\pm \approx 1 \mu\text{m}$ for trap 2 and 3, respectively, as well as the high charge state of 42+, very low excitation radii are already sufficient for successful phase imprint and sufficient SNR during phase measurement. For most measurements, an excitation amplitude of approximately $12(2) \mu\text{m}$ was used, for some measurements also $10(2) \mu\text{m}$, resulting in relativistic shifts and uncertainties below 2×10^{-12} . Although not done during this campaign, with these high $R - 1$ values, it would be beneficial to intentionally excite the ions with slightly different excitation pulses (see ratio 1.02 in Figure 6.2) to minimize the shift on the determined cyclotron frequency ratio.

A tuning ratio optimization was performed before the main measurements as well as the calibration of the excitation radii. In contrast to the neon measurement, a more precise tuning ratio determination was performed afterwards. Due to this, the c_4 and c_6 field coefficients deviate slightly from the optimum for the time of the measurements. However, they are still small enough considering the resulting systematic shifts below 1×10^{-12} . A summary of the trap parameters during that measurement campaign is given in Table 6.2. In addition, the measurement settings are given in Table 6.3.

Axial frequency detection Due to the high charge states, the dip signals induced by the trapped ytterbium ions in our detection system are wide compared to the neon measurement campaign, see Figure 6.3. Despite the larger dip width, the uncertainty of the axial frequency determination is not much increased. The narrow bin-width of down to 10 ms (100 s evolution time) benefits the fit precision. On the other hand, the cooling constant is increased and the time for the phase determination is drastically reduced, see *FFT window* in Table 6.3. In each position, i.e. ion type, the varactor voltage is adjusted as precise as possible to tune the resonance frequency, with an uncertainty of approximately 2 Hz , on the axial frequency of the ion. Accidentally higher differences due to a faulty preparation is spotted in the final analysis and results in discarding the respective measurement run.

An example data set of ϕ_+ and ν_z of measurement run #11 is shown in Figure 6.4. Common fluctuations for both ions (positions) are visible in the phase data as well as in the axial frequencies. The axial frequency stability from shot-to-shot (30 min cycle duration) corresponds to relative 3×10^{-8} and 7×10^{-8} for trap 2 and 3, respectively. If this value is dominated by voltage fluctuations and not by the measurement method

Table 6.2: Trap parameters during the ytterbium measurement campaign (with varactor tuning). The approximate eigenfrequencies are given for the common reference ion $^{172}\text{Yb}^{42+}$. The magnetic field was calculated using the cyclotron frequency ν_c and ion's charge-to-mass ratio from literature [75].

Parameter	Trap 2	Trap 3
r_0 (mm) [58]	5.000 (5)	5.000 (5)
TR (1)	0.87966 (15)	0.879002 (7)
U_0 (V)	-28.14	-12.85
T_z (K)	5 (2)	8 (2)
$\rho_{+,exc}$ (μm)	12 (2)	12 (2)
RLC Q -factor (1)	≈ 3300	≈ 9800
ν_+ (MHz)	≈ 26.26	≈ 26.27
ν_z (kHz)	≈ 707.3	≈ 478.1
ν_- (kHz)	≈ 9.5	≈ 4.4
B_0 (T)	7.002 15 (2)	7.002 16 (2)
B_1 ($\frac{\text{mT}}{\text{m}}$)	1.41 (27)	-1.49 (16)
B_2 ($\frac{\text{m}^2}{\text{m}^2}$)	28 (2)	-5 (2)
c_2 (10^{-3} mm^{-2})	-14.88576(1)	-14.89708(1)
c_4/c_2 (10^{-5} mm^{-2})	-3 (8)	-7 (8)
c_6/c_2 (10^{-6} mm^{-4})	-4 (6)	-2 (6)

Table 6.3: Summary of measurement settings for the N determination and main cycle. In the main cycle only the shortest and longest t_{evol} are used. The amplitudes A for PnP pulses are the set values for the function generators, not the actual voltage on the electrodes.

Setting	Trap 2	Trap 3
N determination averages (1)		3 – 4
N determination t_{evol} (s)	(0.1, 0.25, 0.6, 1.05, 5.05, 11.05, 17.0, 35.05, 70.05, 100.05)	
main cycle duration (h)		12
subcycle averages (1)		5
FFT delay (ms)		1
FFT window / zero padding (s)	0.12 / 9.88	0.015 / 9.985
A_{exc} (V) / t_{exc} (ms)		0.5 / 0.3
$\approx \rho_{\text{exc}}$ (μm)		10 – 12
$A_{\text{coupl.}}$ (V) / $t_{\text{coupl.}}$ (ms)	1.5 / 11	1.3 / 11
pulse window function		tukey (0.5)

itself, the corresponding relative potential stability over the measurement time is 6×10^{-8} and 1.4×10^{-7} for trap 2 and 3, respectively. Due to the different trap potential depths in the two traps, this corresponds to an absolute voltage stability of approximately $2 \times 10^{-6} \mu\text{V}$ for both traps, supporting the hypothesis that the potential is dominated by the same noise source.

Single N+1 error corresponds to a shift of approximately 4×10^{-10} in the measured ratio, which is easily spotted during analysis and can be corrected. For N \pm 1 error common on both ions N determinations, would be harder to spot with only a shift of 9×10^{-12} in the measured ratio. For a single main cycle measurement, the statistical error could be larger than this shift. We gain confidence in our values due to very low deviations of the residuals in the N determination measurement at the beginning of the measurement run, as well as the fact that the cyclotron frequency over multiple measurement runs (multiple N determinations) match to each other. For the cyclotron frequency measurements a shot-to-shot jitter of only 2×10^{-11} to 3×10^{-11} is observed for a shot-time of 2.5 min per subcycle.

Like in all measurements, the magnetron frequency is only measured occasionally, and also in these measurements the magnetron difference is calculated from literature

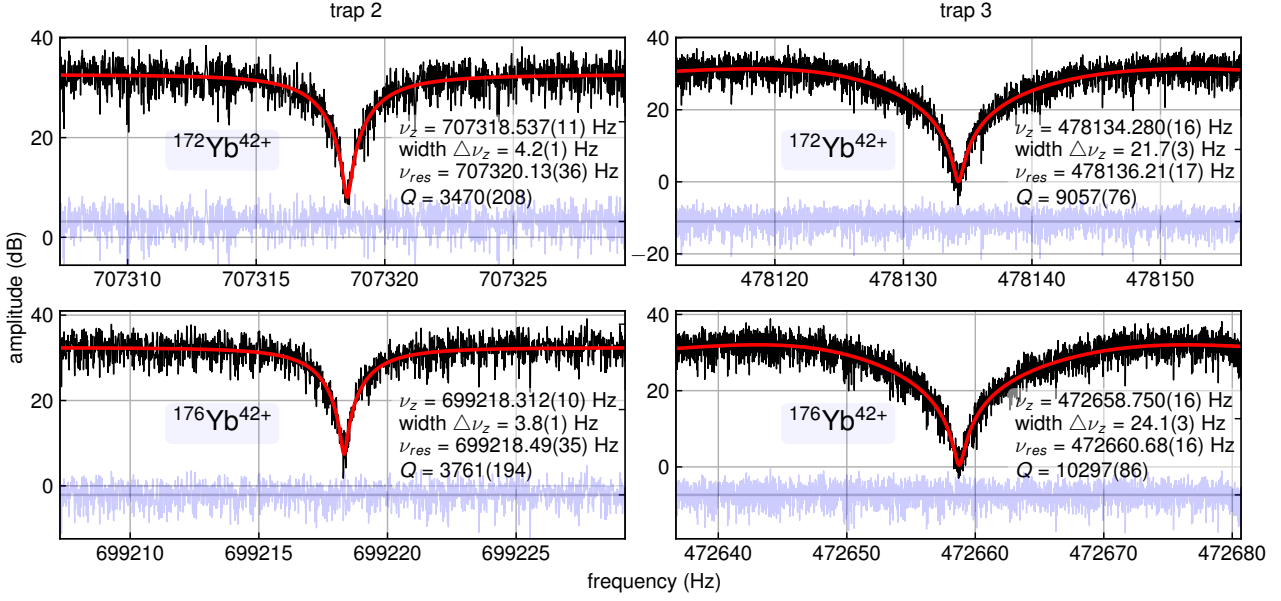


Figure 6.3: Example dip spectra (zoomed in to enlarge the actual dip region) of $^{176}\text{Yb}^{42+}$ (top) and $^{172}\text{Yb}^{42+}$ (bottom) in trap 2 (left) and trap 3 (right). The dip model fit is displayed as the red line and the most relevant fit results are given, with the values in the brackets representing the uncertainties of the fit parameters for that particular least square fit. The pale blue data on the bottom are the fit residuals.

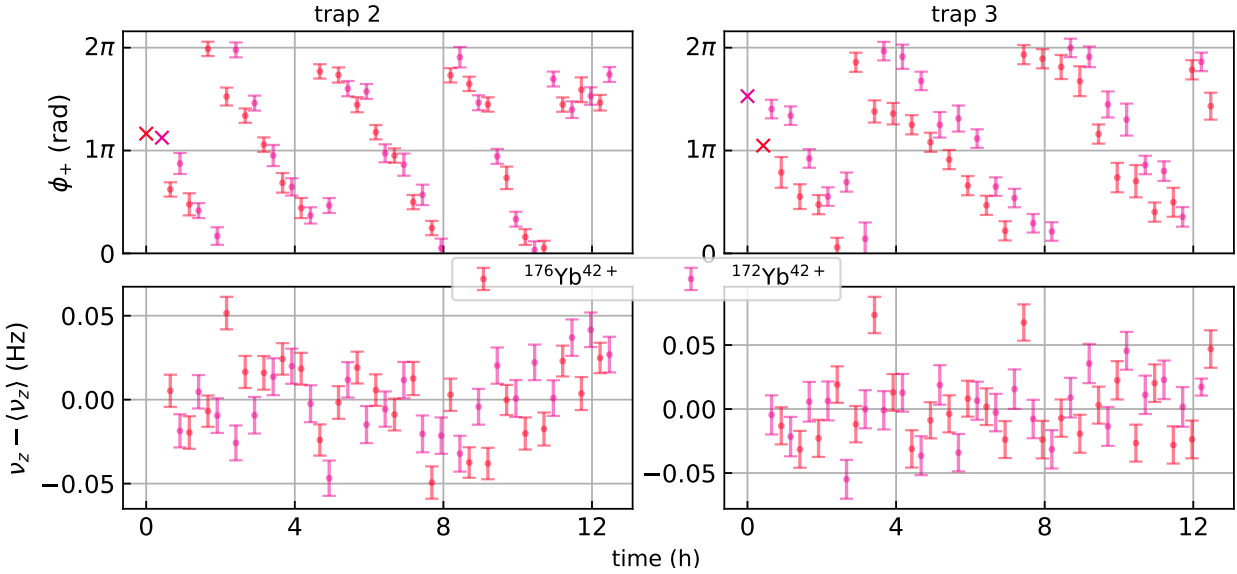


Figure 6.4: Example phase and axial fit data of measurement run #11. The upper panels show the phase data: Each value is an average of phase differences between the phases after the long accumulation time of 20 seconds and the phases after the short accumulation time of 0.1 seconds per cycle. The crosses at the beginning of the measurement data show the last value of the long accumulation time during the N determination at the beginning of a measurement run. The lower panels show the axial frequency data, determined from the averaged spectra during the long phase accumulation times of the PnP measurement via dip fit.

values and used to calculate one magnetron frequency from the one of the other ion. The cyclotron frequency is again calculated using the invariance theorem Equation 2.20, two example measurement runs are shown in Figure 6.5. The final summary of the cyclotron frequency ratios R^{CF} determined via the interpolation method for the ions

$^{172}\text{Yb}^{42+}$ and $^{176}\text{Yb}^{42+}$ are plotted in Figure 6.6. All additional summary plots of the cyclotron frequency ratios for the other isotope ratios can be found in section A.1. The final statistical uncertainties are between 1 and 2×10^{-12} and are given in Table 6.4. These are some of the lowest statistical uncertainties reached at PENTATRAP.

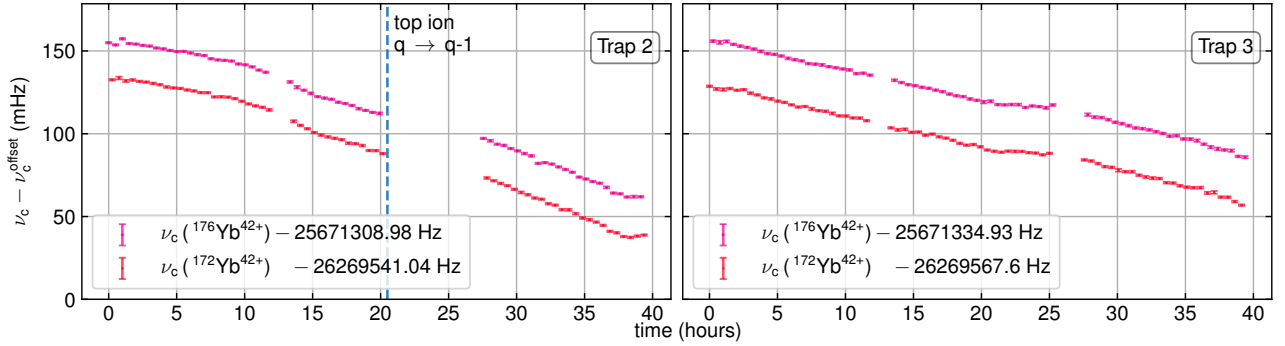


Figure 6.5: Example free cyclotron frequency data of measurement run #10 and #11 of cyclotron frequencies of the ratio of $^{176}\text{Yb}^{42+}$ and $^{172}\text{Yb}^{42+}$. Charge exchanges due to interaction with rest gas limit the life time of the ions, resulting in data loss for one or both traps and require a reloading of the ion set.

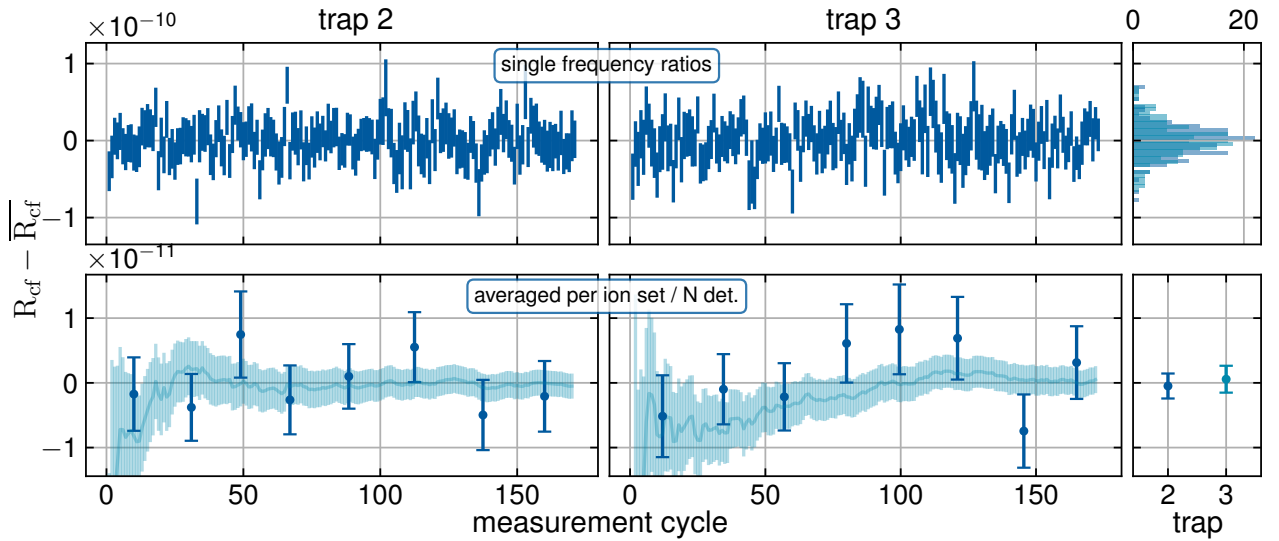


Figure 6.6: Cyclotron frequency ratios (via interpolation method) of $^{176}\text{Yb}^{42+}$ and $^{172}\text{Yb}^{42+}$ ions minus the total mean frequency ratio. The top panels show each determined ratio over chronological measurement numbering (discarded data is not shown) for the two measurement traps 2 and 3 and both datasets as histograms on the right. The lower panels show the average results per individual phase unwrap and N determinations as well as the evolving total average in the background. The lower right panel show the final average of each trap.

Table 6.4: Measured cyclotron frequency ratios of even isotopes A of ytterbium in charge state $42+$ relative to the isotope $A = 172$ in the same charge state.

Isotope A	$R_A^{\text{CF}} = \nu_{c,172} / \nu_{c,A}$
168	0.976 717 951 137 (2)
170	0.988 356 814 141 (2)
174	1.011 648 196 821 (1)
176	1.023 303 526 706 (1)

6.2.1 Systematic corrections

A summary of all systematic corrections for all isotope ratios is given in Table 6.5. Most systematic shifts have been discussed in detail before, only some differences in a selection of shifts will be described in the following. The final corrected ratios are given below in Table 6.6 together with the deduced nuclear mass ratios.

Table 6.5: Systematic corrections ΔR for the determined ratio $R^{\text{CF}} = R' + \Delta R$ with $R' = \nu_{c,172}/\nu_{c,A}$ being the measured ratio. All values are expressed in parts per trillion ($1 \cdot 10^{-12}$). The common total is the quadratically added error of the uncertainties above. For more details see text.

Effect	A	Trap 2	Trap 3
Field imperfections (B_i, c_i)	all	0.0 (0.5)	0.0 (0.5)
Nonlinear phase readout	all	0.0 (1.0)	0.0 (1.5)
Magnetron frequency	all	0.0 (1.0)	0.0 (1.0)
Dip lineshape	all	0.0 (4.0)	0.0 (5.0)
Common total	all	0.0 (4.4)	0.0 (5.3)
	176	-10.0 (0.5)	
Image charge shift	174	- 4.9 (0.2)	
	170	4.8 (0.2)	
	168	9.5 (0.5)	
	176	1.0 (1.5)	
Special relativity	174	0.5 (1.5)	
	170	-0.5 (1.5)	
	168	-1.0 (1.5)	

Field imperfections For the correction of systematic shifts due to field imperfections (c_4, c_6, B_2), the same methods as for the neon campaign apply. The tuning ratio was determined with a little higher precision, by fitting the axial shift in dependence of the excitation radius according to Equation 2.40. The method is explained in more detail in subsection 4.2.1.

Nonlinear phase readout The characterization of the nonlinear phase readout was performed as described in subsection 4.2.6. With the use of shaped pulses, this effect could not be resolved given the achieved statistical uncertainty of the measurements, meaning a sinusoidal fit of the nonlinearity results in an amplitude of 0 with uncertainties of 0.25 and 0.5 degrees in trap 2 and 3, respectively.

Dip lineshape The dip-lineshape error is quite different in this measurement compared to the neon measurements: In the neon measurements the precisely matched axial frequencies helped to actually suppress this systematic uncertainty from slightly off-resonant dip fits. Here, the axial frequencies are not matched, but the resonator frequency is matched to each ions axial frequency. Since each ion is differently off-resonant, no suppression takes place. Although one can now determine the effect more realistically, by scanning the resonance around the axial frequency to determine the dependence, the uncertainty of the correction is still higher. An example determination of the lineshape effect is given in Figure 6.7. In order to reduce the systematic shift due to this effect, we try to position the dips equally in respect to the resonator. The difference between axial frequency and resonator frequency, controlled in the analysis, is kept below 2 Hz. Measurements where the dip positions are not equally off-resonant for both positions or deviating by more the 2 Hz from the resonator are discarded in the

analysis. With varying positions for the measurements used, this effect averages down by a small amount.

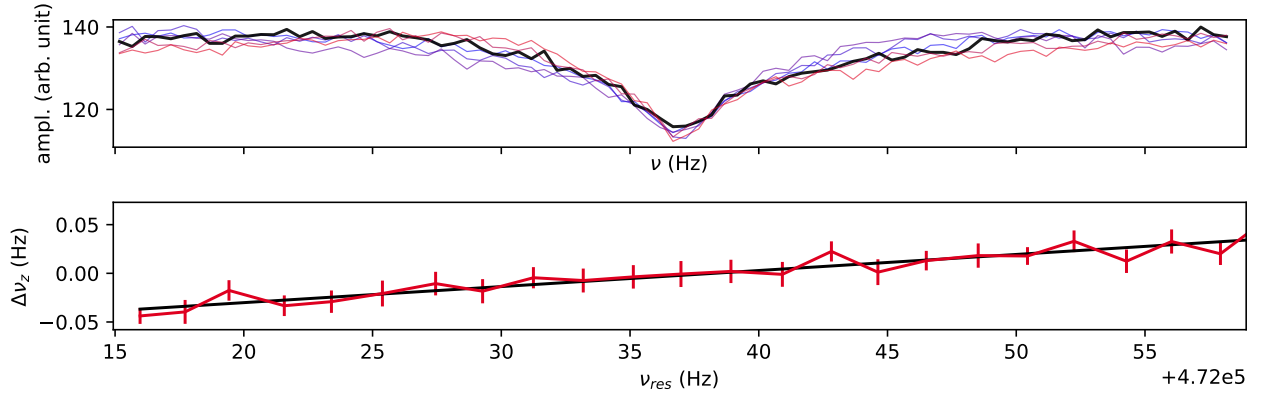


Figure 6.7: Determination of the systematic shift due to imperfect dip-fit lineshape model in trap 3. In the top panel a few example spectra are shown where the resonance is scanned, while the axial frequency is unchanged. In the lower panel the resulting change in axial frequency, averaged over tens of axial dips to resolve the effect, is displayed.

6.2.2 Nuclear mass ratios and neutral masses

The measured cyclotron frequency ratios R^{CF} can be used to directly extract the mass ratio of the respective ions in the traps, but for use in the King plot analysis they have to be corrected to nuclear mass ratios using Equation 2.31. In addition to the measurement results, the electron mass [36] is needed as well as the electron binding energies: The total binding energies of the 28 electrons in the $^{172}\text{Yb}^{42+}$ ion and of the 70 electrons in the ^{172}Yb atom have been calculated with the GRASP2018 code [130] by Chunhai Lyu to be $E_{172}^{(28)} = 350\,773(5)$ eV and $E_{172}^{(70)} = 382\,301(16)$ eV respectively, and are calculated [53]. The difference of the binding energies of the two isotopes, the isotope shift, has also be accounted for and is estimated to be $\Delta E_A^{(28)} = E_{172}^{(28)} - E_A^{(28)} = 0.125\Delta A$, with $\Delta A = A - 172$. The resulting nuclear mass ratios are given in Table 6.6.

Table 6.6: Systematic shift corrected cyclotron frequency ratios R_A^{CF} and resulting nuclear mass ratios η_A of the even, stable ytterbium isotopes relative to the nuclear mass of isotope $A = 172$. The nuclear mass ratios of the ytterbium isotopes with even atomic mass number are determined according to Eq. (2.31) using the cyclotron frequency ratios, the electron mass and binding energies, details see Text.

Isotope A	$R_A^{\text{CF}} = \nu_{c,172}/\nu_{c,A}$	$\eta_A = m_A/m_{172}$
168	0.976 717 951 145 (4)	0.976 715 921 748 (4)
170	0.988 356 814 144 (4)	0.988 355 799 257 (4)
174	1.011 648 196 817 (4)	1.011 649 212 140 (4)
176	1.023 303 526 697 (4)	1.023 305 557 965 (4)

With the binding energy $E_{172}^{(28)}$, the electron mass and the neutral mass of the ^{172}Yb atom, the neutral masses of the other even isotopes can also be calculated. These values are limited by the mass uncertainty of the reference mass ^{172}Yb [75] of 14 nu. All neutral masses are given in Tab. 6.7 and are compared to the current literature values of the atomic mass evaluation 2020 [75]. The masses of three isotopes agree within 1.5σ and the mass of ^{168}Yb shows a deviation by 3.5σ . The uncertainty of $m(^{168}\text{Yb})$ is improved compared to the literature value by a factor of 7.

Table 6.7: Neutral masses in atomic mass units of the five even ytterbium isotopes determined from the measured cyclotron frequency ratios $R_A^{\text{CF}} = \nu_{c,172}/\nu_{c,A}$, the binding energy of the 42 missing electrons $E_{172}^{(70)} - E_{172}^{(28)}$ and the literature mass of isotope $m(^{172}\text{Yb})$ [75]. For comparison also the literature mass values listed in the atomic mass evaluation 2020 [75] are given.

Isotope A	$m(A)$ (this work)	$m(A)$ [75]
168	167.933 890 939 (14)	167.933 891 297 (100)
170	169.934 767 218 (14)	169.934 767 242 (11)
174	173.938 867 541 (14)	173.938 867 545 (11)
176	175.942 574 697 (14)	175.942 574 706 (15)

6.3 Mass-ratio determinations with trap-depth tuning

Before upgrading the detection system, a few determinations of isotope mass ratios have been performed by trap depth tuning for $\nu_z = \nu_{\text{res}}$ -matching and are used here as a cross-check. The measured ratios, as well as the neutral mass ratios determined from these measurements and the respective binding energy, are given in Table 6.8. Also given are the corresponding ratios from the measurements using varactor diodes described above.

Table 6.8: Measured cyclotron frequency ratios including systematic correction, the respective neutral mass ratios and the respective neutral ratios determined from the measurements using the tunable detection system. Details see text.

Isotope A', A	$R_{A,A'}^{\text{CF}} = \nu_{c,A'}/\nu_{c,A}$	$(m_A/m_{A'})_{\text{doublets}}$	$(m_A/m_{A'})_{\text{varactor}}$
168, 172	0.999 976 309 873 082 (6)	0.976 721 066 453 (6)	0.976 721 066 461 (4)
176, 172	1.000 023 690 688 153 (6)	1.023 300 408 494 (6)	1.023 300 408 492 (4)

The uncertainty is higher in these measurements due to the higher statistical uncertainty of 4×10^{-12} and a conservative estimate of the uncertainty of 4×10^{-12} due to the trap tuning and position difference of this rather good doublet, which only needs a change in trap depth of $\approx 1\text{mV}$. The dip-lineshape shift is strongly suppressed here, due to the matching of axial frequencies and because these ions have very equal dip widths and equal individual dip shift characteristics.

Both pairs of neutral mass ratios show agreement within 1σ comparing these charge-to-mass doublet measurements with the tunable detection system measurements. These results are not going to be averaged with the measurements above, but they give confidence that the new measurement method with the tunable detection system does not introduce additional systematic shifts.

6.4 Binding energy measurement

Two cyclotron frequency ratios have been determined with the aim of extracting the electron binding energy difference between the charge states $^{172}\text{Yb}^{41+}$ and $^{172}\text{Yb}^{42+}$ as well as $^{172}\text{Yb}^{42+}$ and $^{172}\text{Yb}^{43+}$. The parameters of these measurements are very similar to the cases of 4 u mass difference of the varactor measurements above, and the same systematic shifts apply with the exception of the image charge shift, which is considered negligible in this case, since the mass difference is marginal; see subsection 2.3.6.

The resulting uncertainties of the binding energies are 0.6 and 0.7 eV, respectively. The determined binding energies are in agreement with theory within 1.5σ . This is the most accurate comparison of measurement results to an external reference value performed at PENTATRAP.

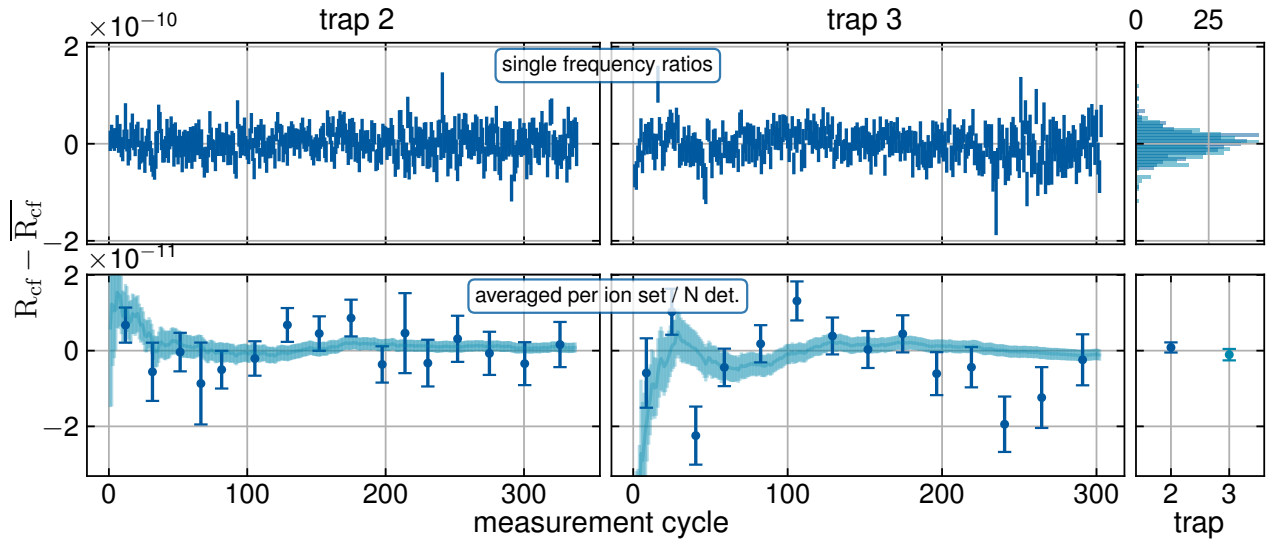


Figure 6.8: Cyclotron frequency ratios (via interpolation method) of $^{172}\text{Yb}^{41+}$ and $^{172}\text{Yb}^{42+}$ ions minus the total mean frequency ratio. The top panels show each determined ratio over chronological measurement numbering (discarded data is not shown) for the two measurement traps 2 and 3 and both dataset as histograms on the right. The lower panels show the average results of data-groups with individual phase unwrap and N determinations as well as the evolving total average in the background. The lower right panel shows the final average of each trap.

Table 6.9: Measured cyclotron frequency ratios (systematics corrected) of two differently charged ^{172}Yb ions and the resulting binding energy of the most outer electron in the respective lower charge state q . The binding energies are extracted using Equation 2.32. The last column gives the respective binding energy from theory calculations [129].

$q + 1/q$	$R^{\text{CF}} = \nu_{c,q+1}/\nu_{c,q}$	E_{172}^q (eV)	$E_{172}^{q,\text{theo}}$ (eV)
42+/41+	1.024 393 499 730 (4)	2036.0 (6)	2035.4 (1)
43+/42+	1.023 812 768 789 (4)	3445.8 (7)	3444.8 (1)

6.5 King Plot analysis

The measured cyclotron frequency ratios, or rather the nuclear mass ratios, are used in combination with IS spectroscopy measurements [131] performed by Chih-Han Yeh at PTB Braunschweig in a King plot analysis. The results have been published in ref. [53]. The details for the extraction of the actual exclusion bounds for a new boson, coupling electrons and neutrons, as well as the extraction of nuclear deformation parameters and the comparison to nuclear theory estimations can be found in the given reference. For a demonstration of the impact of these masses, the mass-normalized king plot is given in Figure 6.9.

A strong nonlinearity is present in the constructed King plot: The residuals show deviations from zero of a few hundred sigma (the error bars in the plot are inflated for visibility). Considering only the first-order approximation in Equation 1.5, this could be interpreted as a signal from a new boson, which is hardly the reality. Considering also the next-order SM contributions of the field shift, the quadratic field shift and the nuclear deformation, the nonlinearity can be explained. As already proposed in [52], the nuclear deformation, which is a higher-order moment of the charge radius r^4 , is considered the most dominant contributor here. This could also be shown in our publication, and an additional analysis was developed and applied by Fiona Kirk from the Group of Elina Fuchs at the Leibniz Universität Hannover to extract the change in nuclear deformation δr^4 as a novel output from these measurements.

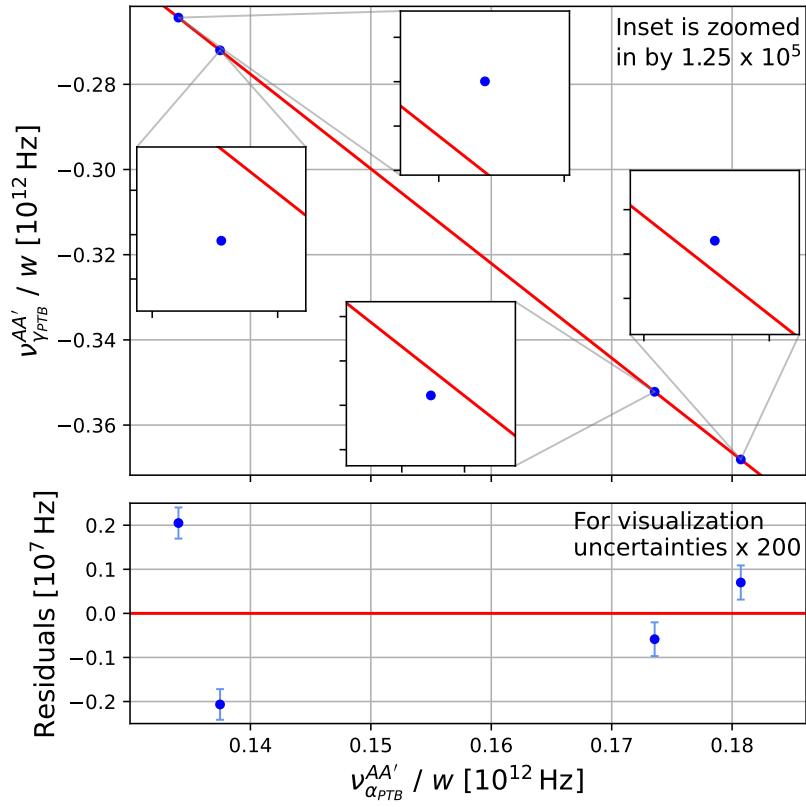


Figure 6.9: Mass normalized King plot from ref. [53] constructed from the IS measurements in [131] and the mass measurements presented here.

Chapter 7

Conclusion & Outlook

7.1 Conclusion

The experimental success in the scope of this thesis is based on the integral improvements of the setup and investigation of measurement systematics over years of experiments. In the course of this thesis, significant contributions and improvements were made to the control system, simulation software and analysis scripts for PENTATRAP, improvement of the stabilization system of the magnet, upgrade of the room-temperature and cryogenic ion beam diagnostics, upgrades to the detection system as well as upgrades of the ion sources and detailed investigation of systematic measurement shifts. Furthermore, the following results have been achieved:

- The most precise mass measurement in atomic mass units to date was performed on ^{20}Ne , contributing to a stringent test of bound-state QED.
- Mass ratios of a chain of stable Yb isotopes were determined on a single digit ppt level, at least a factor of 2 more precise than previous isotope chain ratios determined at PENTATRAP [11, 97], contributing to the search for physics beyond the standard model.
- For the first time direct determination of electron binding energies via mass difference determinations have been achieved on a sub-eV precision, directly testing electron correlation and Breit interaction effects.

Neon mass - tests of bound-state QED The precision of 4×10^{-12} achieved for the determination of an *absolute*¹ atomic mass, demonstrates the capabilities of our mass spectrometer. The measurement performed represents the so far most precise mass determination in atomic mass units (corresponding to an uncertainty of 9×10^{-11}) and clears up a previous deviation between the theoretical and experimental g -factor determined via the literature mass and at the same improves upon this value by a factor of 19. As the first mass determination of a light isotope and the first mass determination with ^{12}C as a reference isotope at PENTATRAP, these measurements pave the way for future measurements to improve the mass values of $m(^{133}\text{Cs})$ and $m(^{87}\text{Rb})$, which is of utmost importance for the determination of α via photon-recoil experiments [72, 73].

The effects limiting the reached precision in this measurement were actually statistical, and the main reason for that is the increased frequency jitter due to the relativistic mass increase depending on the cyclotron frequency and radius, see Equation 2.63. While the mean systematic shift is handled to large extend with the extrapolation to zero amplitude, the necessary large excitation also increases the absolute frequency jitter and therefore the phase jitter of the PnP measurements. Reducing this jitter is not

¹In the sense that it is a measurement in atomic mass units (1/12 of the mass of ^{12}C).

trivial in respect to measurement methods, since the smallest excitation amplitudes used here, were already the minimal excitation radii for a stable phase imprint, so also the PnA method [132] would not help here. The easiest solution is to reduce the charge states and therewith the cyclotron frequency. Although this in principle comes also at the cost of relative precision, we have shown with the ytterbium measurement at half the charge-to-mass ratio a shot-to-shot relative uncertainty of down to 2×10^{-11} for both traps compared to the shot-to-shot relative uncertainty of approximately 7×10^{-11} to 9×10^{-11} in case of neon and carbon at charge-to-mass ratios near $0.5 e/u$. Another solution would be to reduce the field of the magnet, and while that could be the only solution in case of measurements where the charge states is essential to the measurement motivation (meta stable state or binding energy determination), it is probably not worth it.

The systematic uncertainties are more or less equally distributed over the relevant effects. The shift in position difference is easily reduced with the tunable detection system. The image charge shift depends on the mass difference between the used ions, so the relevance of this shift is highly case dependent. If it is a strong limitation, the image charge shift can be measured via the magnetron motion to better than 5% as it was shown in ref. [85]. The nonlinear phase read-out can be eliminated easily by randomizing the phase offset of the excitation and coupling pulses in the PnP measurement. In this way, the nonlinearity should be averaged out. In order to keep the analysis simple, it is recommended to use the same phase offsets for every set of long- and short-phases, so that the offsets will cancel immediately when taking the phase difference.

The dip lineshape error is the least trivial to improve. Reducing the width of the dip and reducing the Q-value of the resonance helps, since it reduces the impact of the resonance frequency on the axial frequency determination via the dip fit, the latter can be done by adding negative feedback to the detection system [133]. Replacing the dip fit determination with phase sensitive measurement of the axial frequency would be a straightforward removal of this systematic shift, but requires a good correction of the image current shift, which is not impossible. Also, performing the axial PnP measurement simultaneously to the modified cyclotron PnP measurement cannot be recommended because: (i) the increased axial amplitude will strongly increase systematic shifts, and (ii) without interaction with the resonator, the axial amplitude will stay on the set value after excitation. Although this interaction-free time is necessary for the phase evolution, an additional shot-to-shot radius distribution is now added and (very likely) increases the phase jitter of the modified cyclotron measurement. The measurements therefore have to be done asynchronously with the reduced cyclotron measurements, which are more sensitive to instabilities of the trapping field. More possibilities arise with the tunable detection system in place, as will be discussed below.

In the end, measurements of light ions are definitely possible with the PENTATRAP setup with relative uncertainties in the low ppt range.

Ytterbium isotope ratios - search for new physics The achieved precision of the ytterbium isotope mass ratios can be attributed to the upgrade of the detection system. With the now tunable resonance frequencies, the prior requirements on the charge-to-mass differences of two ions are now strongly relaxed and much more ion combinations can be used to perform precision mass-ratio determinations at PENTATRAP. The precision of the mass ratios was improved up to 100-fold. The improvements in the neutral atomic mass are quite marginal, and the reason is that, since the King plot analysis only requires precision mass ratios, there was no motivation to improve one of the masses in atomic mass units (currently at best 6×10^{-11}) by measuring one of the isotopes against a better reference. If one of the atomic mass values of the isotopes is improved in the

future, the measured mass ratios from this work will pass the improved uncertainty down to the complete chain to a level of 4×10^{-12} .

The mass-ratios in combination with recent measurements of isotope shifts at the PTB [131], have been used to perform a King plot analysis, which resulted in the strongest bounds for the proposed boson determined by the King plot method to date [53]. A strong King-nonlinearity in this system is confirmed and limits the extracted bounds: The responsible higher-order field shift effects cannot be calculated to sufficient precision in order to correct this SM effect. The measurement data would allow in principle to extract stronger bounds, and with improved theory models, this might be done in the future. Also, the mass-ratio precision reached impacts the King plot to about 0.3 Hz equivalent spectroscopy uncertainty, which therefore will likely support IS measurements in the near future, as the current IS spectroscopy uncertainty is an order of magnitude larger.

In addition to the exclusion bounds for the new boson, with the collaboration of Fiona Kirk from University Hannover (Group of Elina Fuchs), higher-order nuclear charge moments could be extracted from the experimental data as well and have been compared to theoretical predictions of these moments made by Matthias Heinz [134] (Group of Achim Schwenk at TU Darmstadt). These *new observables* can act as a benchmark for nuclear theory.

The main systematics in this measurement is again the infamous dip lineshape error and with more than twice the size of the respective error in the neon mass campaign. The reason is unfortunately the tunable detection system: Since the axial frequencies can be determined to two orders of magnitude better than the detection system resonance frequency, the matching of axial frequencies by adjusting the trap depth (as done in the neon measurements) can be done very precisely. Due to the certainty about the at least near equal off-resonance position in this type of measurement, both axial frequencies will be affected by a largely common shift (depending also on the difference in dip width) that cancels out in the ratio. Compared to that, the tuning of the resonance frequency on the respective axial frequencies has a much higher uncertainty, and there is no common off-resonance aspect that can be exploited here. On the other hand, the shift can be investigated more realistically than varying the dip-fit resonator parameter by scanning the resonance below the dip. The next higher-order systematic shifts can be addressed in the same way as explained before.

The statistical shot-to-shot jitter, as mentioned above, is minimal in these measurements and relative stabilities of down to 2×10^{-11} are achieved. The origin of this jitter is not yet determined. Although it could be a simple magnetic field jitter, like in most other Penning-trap mass spectrometers, also other sources could be possible, such as the stability of the electrostatic field or the mechanical stability, i. e. the stability of the angle between the trap axis and the magnetic field axis or the z -position of the setup in relation to the magnet coils. Although the simultaneous phase measurement of ν_+ and ν_- suggests that it is not the magnetic field, further studies have to be conducted to pinpoint the origin exactly.

The investigation of the ytterbium isotope chain in connection with the King plot analysis has been completed for the time being with these measurements. However, we recently finished the measurements of stable and even Ca isotopes and the analysis, also in combination with IS spectroscopy data from the PTB (Group of Piet Schmidt), is ongoing [135]. In the near future, further measurements on Ca as well as measurements of the isotope chains of Sn and Sr are planned.

Ytterbium binding energies - test of bound-state QED The tunability of the detection system also opens the door to more precise and flexible ion choices for binding

energy determinations in highly charged ions. The determined binding energies in ytterbium are the first direct binding energy determinations in highly charged ions via mass spectrometry on a sub-eV precision. Comparing the determined values to calculated binding energies for this system, present the most precise test of measurement accuracy for the PENTATRAP mass spectrometer so far on a level of 4×10^{-12} . With one measured binding energy in agreement and one with merely 1.5σ this accuracy test is considered passed.

Although these measurements are not precise enough for a stringent test of bound-state QED, they can already verify the validity of electron correlation and Breit effect contributions to the theoretical binding energy determination [129]. The publication of these measurement results and the comparison to calculations including a detailed discussion of the effects probed is in progress.

In addition, these measurements provide a glimpse of the possibilities in this field and pave the way for measurements of binding energies in heavy, highly charged ions, e. g. $^{208}\text{Pb}^{81+}$, allowing stringent tests of bound-state QED. For that purpose an improvement in axial frequency determination would be beneficial. One way one might get rid of the dip lineshape effect is to do the same as for the magnetron frequency: calculate the axial frequency of one ion using the measured axial frequency of the other ion. This way, the systematic shift can be considered common. This method is currently investigated.

7.2 Outlook

7.2.1 Improvements of the apparatus

Some things can still be done to improve the setup. At the accuracy we are, there are several interesting measurements to make, and a higher *duty cycle* of the experiment and lower statistical uncertainty can significantly increase the overall output of the experiment. In the following, I will give an overview of the improvements planned for PENTATRAP.

Cryovalve Our current life-time, which depends on the charge state due to the different cross sections for rest gas atoms, is limited to approximately two days, which typically requires us, for a set of three ions for the measurement scheme, reload the ion set daily. The life-time is dependent on the rest gas pressure in the trap, which currently suffers due to the open connection to the room-temperature beamline. In the next iteration of the cryogenic insert, a cryovalve is implemented to separate the cryogenically cooled trap vacuum from the room-temperature beamline. This will, as already shown by other experiments [80], improve the vacuum conditions and, subsequently, the *lifetime* of highly charged ions in our traps.

Although night-time measurements will still be preferred for mass-ratio measurements to avoid magnetic-field disturbances, multiple characterization measurements can be performed at daytime due to a lesser sensibility. The average statistical uncertainty reached per day, especially for highly charged heavy ions, can be significantly improved for all measurement types, since it is currently suffering from incomplete measurement cycles because of charge exchange with the rest gas.

DC filter The stability of the electrostatic field could in principle be improved by simply increasing the filter constant for the DC trap electrode connections. On the other hand, this is problematic in regard to transport, requiring longer settling times before starting

measurements. This can be addressed with bypass switches or, even simpler, with diodes and appropriate voltage profiles for transport .

An improved trap potential stability could help to disentangle the origin of the phase jitter in the modified cyclotron determination. A definite improvement would be in the phase-sensitive determination of the axial frequency. Due to the high impact of an excited axial motion on the systematic shifts of the cyclotron mode, it is generally not recommended to perform simultaneous phase measurements of the two frequencies. One could perform sequential frequency determinations, but the advantage of performing simultaneous measurements of the two higher eigenfrequencies is in most cases higher than the phase measurement. Although these measurements are not straightforward to use in mass ratio determinations, phase-sensitive ν_z determinations could greatly improve the capabilities for trap characterization measurements.

Cancellation scheme The cancellation scheme, or rather the cancellation analysis scheme, currently does not improve the statistical uncertainty of mass ratios. The interpretation can be that magnetic field fluctuations are not common in neighboring traps or that the phase fluctuations on long evolution times are not dominantly caused by magnetic field fluctuations at all. Other sources could be the electrostatic field as mentioned above. A possible test of this assumption could be to perform simultaneous measurements with a pair of heavy highly charged ions that can be made resonant with the tunable detection system at the same trap depth *in both traps*. Given the same trap depth can be used, the same voltage source can be used for both traps, which would allow us to test if the phase jitter is then correlated between the traps.

In the initial design of PENTATRAP, it was actually planned to have matching resonator frequencies and therefore also equal potentials [59]. Although a good idea in principle, it requires cumbersome tuning of the resonators. Even more relevant, it would cause more equal conditions for both measurement traps, which weakens our current situation regarding comparison of the results from both traps acting as a type of internal systematic cross-check.

Lower temperature This is not new: A temperature reduction can often improve systematic and statistical uncertainty. Although methods like the extrapolation to zero excitation amplitude used in the neon campaign help to reduce the systematic uncertainties a lot, a lower temperature would still improve on top of that. The statistical uncertainty can benefit considerably from a reduction in thermal radii, especially for light ions. There are multiple ideas on how to reach lower temperatures, the easiest being feedback cooling of the resonator, which can easily result in temperature reduction of a factor of 4 or more. Although this definitely works and could be shown as well in test measurements at PENTATRAP with a new FPGA-based system [133], possible systematics have yet to be investigated.

Another approach is to directly cool the cyclotron motion using a resonator instead of sideband coupling to the axial motion. This would reduce the thermal radius in the cyclotron motion by nearly two orders of magnitude. This has not been done at PENTATRAP because high Q factors in this frequency range are difficult to achieve and the cooling time with low Q factors is often on a time scale of a few tens of minutes to hours. This would greatly increase the measurement time and is simply not practical. A possible solution to this specific problem of low Q factors would be to slightly modify the measurement scheme starting by loading four ions in an A-B-B-A sequence. This would allow us to measure in traps 2 and 4 simultaneously, while cooling the cyclotron motion of the ions stored in trap 1, 3 or 5. These three traps need to be connected to cyclotron resonators, though at least for trap 1 and 5 the same resonator could be used.

An additional problem with this is that in order to use these in multiple measurement campaigns, a vast tunable range would be necessary. Limiting to the most relevant cases (highly charged light ions), one could aim at cyclotron frequencies near $0.5e/u$ charge-to-mass ratio.

Other ideas exist, which have much lower possible end temperatures: Methods like laser cooling of beryllium ions in a neighboring trap and coupling them to the ion of interest via shared resonator [136, 137] or shared endcap have in parts been demonstrated and are currently also investigated for example at the μTEX experiment at the MPIK. Instead of a laser-cooled beryllium cloud, also an electron cloud could be used as a *heat bath*, which cools its cyclotron motion *automatically* via emission of synchrotron radiation, currently investigated at the ELCOTRAP experiment at the MPIK. Although these methods could achieve temperatures much lower than those for feedback cooling, the experimental effort is also much larger and requires a redesign of the experimental setup and further development and testing.

Two-ion balance The two-ion balance method, developed at the MIT [70, 71], uses two co-trapped ions on a common magnetron orbit (the magnetron motion of the two ions is strongly coupled) to determine the difference of cyclotron frequencies with a strong suppression of common magnetic field fluctuations². Since the two ions are only separated by a few hundred μm , magnetic field fluctuations will be highly correlated and while in a phase sensitive determination of the cyclotron frequency the phase jitter can be huge after a long accumulation time, the difference of the phases of two ions should remain stable. This allows for very precise determinations of cyclotron frequency differences even in challenging environments with regard to field fluctuations. The drawbacks are systematics: Even though this method allows one to reach low statistical uncertainties very fast, the systematics due to imperfect trapping fields are much stronger due to the higher motional amplitude. This was also the limit and was strongly discussed in the publications of the original measurements at MIT. Additionally, all technical and thermal phase jitter will remain and can also increase as a result of the higher amplitudes. Furthermore, a high magnetron orbit can increase the shifts as a result of image charges on the electrodes.

The systematic shift situation can be improved when looking at different quantities: In the ALPHATRAP experiment, the two-ion balance method has been successfully applied to measure the difference in Larmor frequencies of two co-trapped neon isotopes [33]. The g -factor difference was determined with an increase in precision of two orders of magnitude compared to the difference determined from single g -factor determinations. The same idea could be applied to other measurement cases where the accuracy of the absolute cyclotron frequency is not that relevant. An example in regard of mass measurements would be the determination of meta-stable states or low-energy Q -values of nuclear reactions because there the absolute frequencies are also not as relevant compared to the frequency differences. Unfortunately, the respective axial frequencies and modified cyclotron frequencies are so similar that these motions will also strongly couple, making a measurement of the difference of the free cyclotron frequencies probably impossible. Even if these motions are not coupled, the axial frequencies will be so similar that distinguishing the signals of two ions is not easy.

Still, this method should be tested, especially to see if the coupling of the higher motions can be avoided, and if so, if it is possible to actively cause systematic shifts of the axial frequencies at the time of the phase readout to allow an easy extraction of the phase difference.

²Sometimes referred to as using a decoherence-free subspace.

7.2.2 Additional motivations for future mass determinations

Beside the motivations relevant for the measurements performed during this thesis, there are several more motivations for high precision mass and mass-ratio determinations of which a few have already been mentioned.

Meta stable states and Q-values of nuclear reactions The detection of meta-stabilized states in highly charged ions, the first time measured by accident [97], is interesting for future developments of optical atomic clocks, which can also be used to probe for physics beyond the standard model, e.g. temporal variation of the fine structure constant [128, 138–140]. Since the energies of metastable states can be calculated to higher precision than we can measure them, and the principal possibilities have already been demonstrated, the motivation for these measurements is somewhat reduced. Still, PENTATRAP aims to perform measurements of metastable states in the future, especially those with life times on the order of (just) a few hours, where a decay could be monitored during measurement in the traps. For these the motivation is still high, since the theoretical estimation of the life-time of metastable states is quite poor. Very promising cases with also sufficient energy for easy detection predicted by our theory colleagues might be, for example, the metastable state $[\text{Ar}] 3d^4 5D_4$ in Xe^{32+} with a proposed life time of approximately 3 h and an energy difference to the ground state of 18 eV as well as the same electronic configuration in Ba^{34+} with a proposed life time of approximately 10 h and an energy difference to the ground state of 21 eV.

Test of special relativity A direct test of special relativity was planned from the beginning. The idea is to measure the Q-value of a nuclear reaction and compare it with the complete energy and masses released. This was also the motivation behind one of the two-ion-balance measurements at MIT [69], which at that time resulted in the most precise direct test of special relativity. At PENTATRAP a similar measurement is planned, measuring the Q-value of the neutron capture in ^{35}Cl . The single γ emitted in the decay makes an energy determination possible via Bragg crystal spectroscopy, e.g. at the GAMS6 experiment at ILL in Grenoble.

Total binding energy determinations The determination of binding energies of valence electrons in highly charged ions was already discussed above, being also part of the measurements conducted in this thesis. Determining the total binding energy that was necessary to produce an HCl can be even more interesting. The absolute error on the measurement will only slightly increase, while the uncertainty of the respective theory calculations will. This will be a much stronger test of the models and theory behind the binding energy calculations than the single binding energies measured so far. In principle, one can simply rearrange Equation 2.29 to extract the total binding energy of one HCl by measuring the cyclotron frequency ratio to a light ion (e.g. carbon) and entering the light ions binding energies, which are likely known to high precision from other experiments, as well as the mass ratio from the literature. This already exposes the difficulties of these measurements: (i) The precision of the mass ratio has to be very high in order to reach binding energies of only a few eV and (ii) the systematic effects can be very high because of the large mass difference, especially the image charge shift. The image charge shift could be measured to correct for it in higher precision. Regarding the mass ratio, some promising candidates would be e.g. ^{84}Kr or ^{86}Kr , but also ^{133}Cs or ^{174}Yb could be used.

Absolute masses for the determination of the fine structure constant The most precise determinations of the fine structure constant α , or rather the vacuum permittivity

ϵ_0 , are currently performed by matter-wave interferometry measuring the recoil velocity of a ^{133}Cs or ^{87}Rb atom that absorb a photon [72, 73]. With improved precision of the interferometry, the mass values in atomic mass units need to be improved as well to not limit the uncertainty of the results. These mass measurements are rather difficult, since ideally it should be a measurement against carbon to highest precision. With two ions of vastly different masses, systematics have to be investigated thoroughly. The image charge shift has to be determined precisely, the dip-lineshape shift is very different for the two ions, all other systematics depending on the different thermal amplitudes will increase as well and feedback cooling might be necessary. The output, on the other hand, is considerable: not only the determination of the fine structure constant, but also an improved conversion factor $\frac{\text{eV}}{\text{u}}$ is determined [36], which has impacts in numerous precision experiments.

List of Publications

Sorted by citation number equal to the thesis. For publications with significant contributions, my name is underlined. For publications as (shared-) first-author, my name is marked with an asterix *.

- [11] A. Rischka, H. Cakir, **M. Door**, P. Filianin, Z. Harman, W. J. Huang, P. Indelicato, C. H. Keitel, C. M. König, K. Kromer, M. Müller, Y. N. Novikov, R. X. Schüssler, C. Schweiger, S. Eliseev, and K. Blaum. „Mass-Difference Measurements on Heavy Nuclides with an eV/c^2 Accuracy in the PENTATRAP Spectrometer“. In: *Phys. Rev. Lett.* 124 (11 2020), p. 113001. DOI: 10.1103/PhysRevLett.124.113001 (cit. on pp. 1, 2, 13, 20, 35, 37, 78, 89).
- [13] R. X. Schüssler, H. Bekker, M. Braß, H. Cakir, J. R. Crespo López-Urrutia, **M. Door**, P. Filianin, Z. Harman, M. W. Haverkort, W. J. Huang, P. Indelicato, C. H. Keitel, C. M. König, K. Kromer, M. Müller, Y. N. Novikov, A. Rischka, C. Schweiger, S. Sturm, S. Ulmer, S. Eliseev, and K. Blaum. „Detection of metastable electronic states by Penning trap mass spectrometry“. In: *Nature* 581.7806 (2020), pp. 42–46. DOI: 10.1038/s41586-020-2221-0 (cit. on pp. 1, 13, 35, 37, 66, 78).
- [14] P. Filianin, C. Lyu, **M. Door**, K. Blaum, W. J. Huang, M. Haverkort, P. Indelicato, C. H. Keitel, K. Kromer, D. Lange, Y. N. Novikov, A. Rischka, R. X. Schüssler, C. Schweiger, S. Sturm, S. Ulmer, Z. Harman, and S. Eliseev. „Direct Q -Value Determination of the β^- Decay of ^{187}Re “. In: *Phys. Rev. Lett.* 127 (7 2021), p. 072502. DOI: 10.1103/PhysRevLett.127.072502 (cit. on pp. 1, 35, 37, 66, 78).
- [15] C. Schweiger, M. Braß, V. Debierre, **M. Door**, H. Dorrer, C. E. Düllmann, C. Enss, P. Filianin, L. Gastaldo, Z. Harman, M. W. Haverkort, J. Herkenhoff, P. Indelicato, C. H. Keitel, K. Kromer, D. Lange, Y. N. Novikov, D. Renisch, A. Rischka, R. X. Schüssler, S. Eliseev, and K. Blaum. „Penning-trap measurement of the Q value of electron capture in ^{163}Ho for the determination of the electron neutrino mass“. In: *Nature Physics* (2024). DOI: 10.1038/s41567-024-02461-9 (cit. on pp. 1, 78).
- [17] L. Gastaldo, K. Blaum, K. Chrysalidis, T. D. Goodacre, A. Domula, **M. Door**, H. Dorrer, C. E. Düllmann, K. Eberhardt, S. Eliseev, C. Enss, A. Faessler, P. Filianin, A. Fleischmann, D. Fonnesu, L. Gamer, R. Haas, C. Hassel, D. Hengstler, J. Jochum, K. Johnston, U. Kebschull, S. Kempf, T. Kieck, U. Köster, S. Lahiri, M. Maiti, F. Mantegazzini, B. Marsh, P. Neroutsos, Y. N. Novikov, P. C. O. Ranitzsch, S. Rothe, A. Rischka, A. Saenz, O. Sander, F. Schneider, S. Scholl, R. X. Schüssler, C. Schweiger, F. Simkovic, T. Stora, Z. Szücs, A. Türler, M. Veinhard, M. Weber, M. Wegner, K. Wendt, and K. Zuber. „The electron capture in ^{163}Ho experiment – ECHO“. English. In: *The European Physical Journal. Special Topics* 226.8 (2017), pp. 1623–1694 (cit. on pp. 2, 36).
- [31] F. Heiße, **M. Door***, T. Sailer, P. Filianin, J. Herkenhoff, C. M. König, K. Kromer, D. Lange, J. Morgner, A. Rischka, C. Schweiger, B. Tu, Y. N. Novikov, S. Eliseev, S. Sturm, and K. Blaum. „High-Precision Determination of g Factors and Masses of $^{20}\text{Ne}^{9+}$ and $^{22}\text{Ne}^{9+}$ “. In: *Phys. Rev. Lett.* 131 (25 2023), p. 253002. DOI: 10.1103/PhysRevLett.131.253002 (cit. on pp. 2, 3, 70, 74, 75).
- [53] **M. Door***, C.-H. Yeh, M. Heinz, F. Kirk, C. Lyu, T. Miyagi, J. C. Berengut, J. Bieroń, K. Blaum, L. S. Dreissen, S. Eliseev, P. Filianin, M. Filzinger, E. Fuchs, H. A. Fürst, G. Gaigalas, Z. Harman, J. Herkenhoff, N. Huntemann, C. H. Keitel, K. Kromer, D. Lange, A. Rischka, C. Schweiger, A. Schwenk, N. Shimizu, and T. E. Mehlstäubler. *Search for new bosons with ytterbium isotope shifts*. 2024. DOI: 10.48550/arXiv.2403.07792 (cit. on pp. 5, 85, 87, 88, 91).

- [74] K. Kromer, C. Lyu, **M. Door**, P. Filianin, Z. Harman, J. Herkenhoff, W. Huang, C. H. Keitel, D. Lange, Y. N. Novikov, C. Schweiger, S. Eliseev, and K. Blaum. „High-precision mass measurement of doubly magic ^{208}Pb “. In: *Eur. Phys. J. A* 58 (10 2022), p. 202. DOI: 0.1140/epja/s10050-022-00860-1 (cit. on pp. 12, 35).
- [85] K. Kromer, C. Lyu, J. Bieroń, **M. Door**, L. Enzmann, P. Filianin, G. Gaigalas, Z. Harman, J. Herkenhoff, W. Huang, C. H. Keitel, S. Eliseev, and K. Blaum. „Atomic mass determination of uranium-238“. In: *Phys. Rev. C* 109 (2 2024), p. L021301. DOI: 10.1103/PhysRevC.109.L021301 (cit. on pp. 21, 61, 62, 90).
- [98] R. X. Schüssler, **M. Door**, A. Rischka, H. Bekker, J. R. C. Lopez-Urrutia, P. Filianin, S. Eliseev, Y. N. Novikov, S. Sturm, S. Ulmer, and K. Blaum. „Recent Developments at the High-Precision Mass Spectrometer PENTATRAP“. In: *JPS Conf. Proc.* 18 (2017), p. 011020. DOI: 10.7566/JPSCP.18.011020 (cit. on pp. 35, 37).
- [104] C. Schweiger, C. M. König, J. R. Crespo López-Urrutia, **M. Door**, H. Dorrer, C. E. Düllmann, S. Eliseev, P. Filianin, W. Huang, K. Kromer, P. Micke, M. Müller, D. Renisch, A. Rischka, R. X. Schüssler, and K. Blaum. „Production of highly charged ions of rare species by laser-induced desorption inside an electron beam ion trap“. In: *Rev. Sci. Instrum.* 90.12 (2019), p. 123201. DOI: 10.1063/1.5128331 (cit. on pp. 36, 77).
- [107] C. Schweiger, **M. Door**, P. Filianin, J. Herkenhoff, K. Kromer, D. Lange, D. Marschall, A. Rischka, T. Wagner, S. Eliseev, and K. Blaum. „Fast silicon carbide MOSFET based high-voltage push-pull switch for charge state separation of highly charged ions with a Bradbury-Nielsen gate“. In: *Review of Scientific Instruments* 93.9 (2022), p. 094702. DOI: 10.1063/5.0083515 (cit. on p. 37).
- [108] E. Piselli, A. Akroh, K. Blaum, **M. Door**, D. Leimbach, and S. Rothe. „CERN Accelerators Beam Optimization Algorithm“. In: *Proc. ICALEPCS'19* (New York, NY, USA). International Conference on Accelerator and Large Experimental Physics Control Systems 17. JACoW Publishing, Geneva, Switzerland, 2020, pp. 1379–1384. DOI: 10.18429/JACoW-ICALEPCS2019-WEPHA124 (cit. on p. 37).
- [118] A. Kaiser, S. Dickopf, **M. Door**, R. Behr, U. Beutel, S. Eliseev, A. Kaushik, K. Kromer, M. Müller, L. Palafox, S. Ulmer, A. Mooser, and K. Blaum. „Josephson voltage standards as an ultra-stable low-noise voltage source for precision Penning-trap experiments“. In: *Applied Physics Letters* 124 (2024), p. 000000. DOI: 10.1063/5.0206779 (cit. on p. 46).
- [128] K. Kromer, C. Lyu, **M. Door**, P. Filianin, Z. Harman, J. Herkenhoff, P. Indelicato, C. H. Keitel, D. Lange, Y. N. Novikov, C. Schweiger, S. Eliseev, and K. Blaum. „Observation of a Low-Lying Metastable Electronic State in Highly Charged Lead by Penning-Trap Mass Spectrometry“. In: *Phys. Rev. Lett.* 131 (22 2023), p. 223002. DOI: 10.1103/PhysRevLett.131.223002 (cit. on pp. 78, 95).
- [133] J. Herkenhoff, **M. Door**, P. Filianin, W. Huang, K. Kromer, D. Lange, R. X. Schüssler, C. Schweiger, S. Eliseev, and K. Blaum. „A digital feedback system for advanced ion manipulation techniques in Penning traps“. In: *Rev. Sci. Instrum.* 92.10 (2021), p. 103201 (cit. on pp. 90, 93).
- [135] **M. Door** and et al. *Nonlinear isotope shifts in calcium*. (2024) in preparation (cit. on p. 91).
- [141] **M. Door*** and et al. *Binding energy determination of the valence electron in $^{172}\text{Yb}^{41+}$ and $^{172}\text{Yb}^{42+}$ to test QED*. (2024) in preparation.

Bibliography

- [1] T. KAJITA. „Atmospheric neutrinos and discovery of neutrino oscillations“. In: *Proceedings of the Japan Academy, Series B* 86.4 (2010), pp. 303–321. DOI: 10.2183/pjab.86.303 (cit. on p. 1).
- [2] M. Gonzalez-Garcia and M. Maltoni. „Phenomenology with massive neutrinos“. In: *Physics Reports* 460.1 (2008), pp. 1–129. DOI: <https://doi.org/10.1016/j.physrep.2007.12.004> (cit. on p. 1).
- [3] M. Dine and A. Kusenko. „Origin of the matter-antimatter asymmetry“. In: *Rev. Mod. Phys.* 76 (2003), pp. 1–30. DOI: 10.1103/RevModPhys.76.1 (cit. on p. 1).
- [4] M. Markevitch et al. „Direct Constraints on the Dark Matter Self-Interaction Cross Section from the Merging Galaxy Cluster 1E 0657–56“. en. In: *The Astrophysical Journal* 606.2 (2004). Publisher: IOP Publishing, p. 819. DOI: 10.1086/383178 (cit. on p. 1).
- [5] D. Clowe et al. „A Direct Empirical Proof of the Existence of Dark Matter“. en. In: *The Astrophysical Journal* 648.2 (2006). Publisher: IOP Publishing, p. L109. DOI: 10.1086/508162 (cit. on p. 1).
- [6] M. Bradac et al. „Revealing the Properties of Dark Matter in the Merging Cluster MACS J0025.4–1222*“. en. In: *The Astrophysical Journal* 687.2 (2008). Publisher: IOP Publishing, p. 959. DOI: 10.1086/591246 (cit. on p. 1).
- [7] V. C. Rubin and W. K. Ford Jr. „Rotation of the Andromeda nebula from a spectroscopic survey of emission regions“. In: *Astrophysical Journal, vol. 159, p. 379* 159 (1970), p. 379 (cit. on p. 1).
- [8] A. Jenkins et al. „Evolution of Structure in Cold Dark Matter Universes“. en. In: *The Astrophysical Journal* 499.1 (1998). Publisher: IOP Publishing, p. 20. DOI: 10.1086/305615 (cit. on p. 1).
- [9] P. J. E. Peebles and B. Ratra. „The cosmological constant and dark energy“. In: *Rev. Mod. Phys.* 75 (2 2003), pp. 559–606. DOI: 10.1103/RevModPhys.75.559 (cit. on p. 1).
- [10] M. Mougeot et al. „Mass measurements of 99–101In challenge ab initio nuclear theory of the nuclide 100Sn“. In: *Nature Physics* 17.10 (2021), pp. 1099–1103. DOI: 10.1038/s41567-021-01326-9 (cit. on p. 1).
- [11] A. Rischka et al. „Mass-Difference Measurements on Heavy Nuclides with an eV/c² Accuracy in the PENTATRAP Spectrometer“. In: *Phys. Rev. Lett.* 124 (11 2020), p. 113001. DOI: 10.1103/PhysRevLett.124.113001 (cit. on pp. 1, 2, 13, 20, 35, 37, 78, 89).
- [12] F. Heiße et al. „High-Precision Measurement of the Proton’s Atomic Mass“. In: *Phys. Rev. Lett.* 119 (3 2017), p. 033001. DOI: 10.1103/PhysRevLett.119.033001 (cit. on pp. 1, 49).
- [13] R. X. Schüssler et al. „Detection of metastable electronic states by Penning trap mass spectrometry“. In: *Nature* 581.7806 (2020), pp. 42–46. DOI: 10.1038/s41586-020-2221-0 (cit. on pp. 1, 13, 35, 37, 66, 78).
- [14] P. Filianin et al. „Direct Q-Value Determination of the β^- Decay of ¹⁸⁷Re“. In: *Phys. Rev. Lett.* 127 (7 2021), p. 072502. DOI: 10.1103/PhysRevLett.127.072502 (cit. on pp. 1, 35, 37, 66, 78).

- [15] C. Schweiger et al. „Penning-trap measurement of the Q value of electron capture in ^{163}Ho for the determination of the electron neutrino mass“. In: *Nature Physics* (2024). DOI: 10.1038/s41567-024-02461-9 (cit. on pp. 1, 78).
- [16] J. Karthein et al. „Direct decay-energy measurement as a route to the neutrino mass“. en. In: *Hyperfine Interact* 240.1 (2019), p. 61. DOI: 10.1007/s10751-019-1601-z (cit. on p. 1).
- [17] L. Gastaldo et al. „The electron capture in ^{163}Ho experiment – ECHO“. English. In: *The European Physical Journal. Special Topics* 226.8 (2017), pp. 1623–1694 (cit. on pp. 2, 36).
- [18] S. Rainville, J. K. Thompson, and E. G. Myers. „A direct test of $E = mc^2$ “. English. In: *Nature* 438 (2005), p. 1096 (cit. on pp. 2, 12).
- [19] K. Blaum. „High-accuracy mass spectrometry with stored ions“. In: *Physics Reports* 425.1 (2006), pp. 1–78. DOI: <https://doi.org/10.1016/j.physrep.2005.10.011> (cit. on p. 2).
- [20] J. Repp et al. „PENTATRAP: a novel cryogenic multi-Penning-trap experiment for high-precision mass measurements on highly charged ions“. In: *Appl. Phys. B* 107.4 (2012), pp. 983–996. DOI: 10.1007/s00340-011-4823-6 (cit. on pp. 2, 35).
- [21] F. Heiße et al. „High-precision mass spectrometer for light ions“. In: *Phys. Rev. A* 100.2 (2019), p. 022518. DOI: 10.1103/PhysRevA.100.022518 (cit. on pp. 2, 11, 64, 69, 79).
- [22] D. J. Fink and E. G. Myers. „Deuteron-to-Proton Mass Ratio from Simultaneous Measurement of the Cyclotron Frequencies of H_2^+ and D^+ “. In: *Phys. Rev. Lett.* 127 (24 2021), p. 243001. DOI: 10.1103/PhysRevLett.127.243001 (cit. on pp. 2, 11).
- [23] C. Smorra et al. „BASE – The Baryon Antibaryon Symmetry Experiment“. en. In: *The European Physical Journal Special Topics* 224.16 (2015), pp. 3055–3108. DOI: 10.1140/epjst/e2015-02607-4 (cit. on p. 2).
- [24] M. Redshaw et al. „Status of CHIP-TRAP: The Central Michigan University High-Precision Penning Trap“. en. In: *Atoms* 11.10 (2023). Number: 10 Publisher: Multi-disciplinary Digital Publishing Institute, p. 127. DOI: 10.3390/atoms11100127 (cit. on p. 2).
- [25] M. J. Gutiérrez et al. „The TRAPSENSOR facility: an open-ring 7 tesla Penning trap for laser-based precision experiments“. en. In: *New Journal of Physics* 21.2 (2019). Publisher: IOP Publishing, p. 023023. DOI: 10.1088/1367-2630/aafa45 (cit. on p. 2).
- [26] I. Beltrami et al. „New precision measurements of the muonic $3d_{5/2}-2p_{3/2}$ X-ray transition in ^{24}Mg and ^{28}Si : Vacuum polarisation test and search for muon-hadron interactions beyond QED“. In: *Nucl. Phys. A* 451.4 (1986), pp. 679–700. DOI: [https://doi.org/10.1016/0375-9474\(86\)90299-X](https://doi.org/10.1016/0375-9474(86)90299-X) (cit. on p. 2).
- [27] S. Sturm et al. „ g Factor of Hydrogenlike $^{28}\text{Si}^{13+}$ “. In: *Phys. Rev. Lett.* 107.2 (2011), p. 023002. DOI: 10.1103/PhysRevLett.107.023002 (cit. on p. 2).
- [28] S. Sturm et al. „ g -factor measurement of hydrogenlike $^{28}\text{Si}^{13+}$ as a challenge to QED calculations“. In: *Phys. Rev. A* 87.3 (2013), p. 030501. DOI: 10.1103/PhysRevA.87.030501 (cit. on p. 2).
- [29] J. Ullmann et al. „High precision hyperfine measurements in Bismuth challenge bound-state strong-field QED“. In: *Nat. Commun.* 8 (1 2017), p. 15484. DOI: 10.1038/ncomms15484 (cit. on p. 2).
- [30] S. Alighanbari et al. „Precise test of quantum electrodynamics and determination of fundamental constants with HD^+ ions“. In: *Nature* 581.7807 (2020), pp. 152–158 (cit. on pp. 2, 3).
- [31] F. Heiße et al. „High-Precision Determination of g Factors and Masses of $^{20}\text{Ne}^{9+}$ and $^{22}\text{Ne}^{9+}$ “. In: *Phys. Rev. Lett.* 131 (25 2023), p. 253002. DOI: 10.1103/PhysRevLett.131.253002 (cit. on pp. 2, 3, 70, 74, 75).

- [32] J. Morgner et al. „Stringent test of QED with hydrogen-like tin“. In: *Nature* 622.7981 (2023), pp. 53–57. DOI: 10.1038/s41586-023-06453-2 (cit. on p. 2).
- [33] T. Sailer et al. „Measurement of the bound-electron g -factor difference in coupled ions“. In: *Nature* 606.7914 (7914 2022), pp. 479–483. DOI: 10.1038/s41586-022-04807-w (cit. on pp. 2, 94).
- [34] S. Sturm et al. „The ALPHATRAP experiment“. In: *Eur. Phys. J. Spec. Top.* 227.13 (2019), pp. 1425–1491. DOI: 10.1140/epjst/e2018-800225-2 (cit. on pp. 2, 3, 19).
- [35] S. Sturm et al. „High-precision measurement of the atomic mass of the electron“. In: *Nature* 506.7489 (2014), pp. 467–470 (cit. on pp. 2, 74).
- [36] E. Tiesinga et al. „CODATA recommended values of the fundamental physical constants: 2018“. In: *Rev. Mod. Phys.* 93.2 (2021), p. 025010. DOI: 10.1103/RevModPhys.93.025010 (cit. on pp. 3, 12, 75, 85, 96).
- [37] A. Kramida et al. NIST Atomic Spectra Database (ver. 5.11), [Online], [2024, April 10]. National Institute of Standards and Technology, Gaithersburg, MD. 2023. DOI: 10.18434/T4W30F (cit. on pp. 3, 12, 63, 64, 74, 75).
- [38] A. J. G. Martínez et al. „The Heidelberg EBIT: Present Results and Future Perspectives“. In: *Journal of Physics: Conference Series* 72.1 (2007), p. 012001. DOI: 10.1088/1742-6596/72/1/012001 (cit. on p. 3).
- [39] M. S. Safronova et al. „Search for new physics with atoms and molecules“. In: *Rev. Mod. Phys.* 90 (2018), p. 025008. DOI: 10.1103/RevModPhys.90.025008 (cit. on p. 4).
- [40] D. Bettoni et al. „The high intensity frontier“. In: *Phys. Rep.* 434 (2006), pp. 47–111 (cit. on p. 4).
- [41] M. Mangano. „LHC at 10: the physics legacy“. In: *arXiv preprint arXiv:2003.05976* (2020) (cit. on p. 4).
- [42] S. Knapen, T. Lin, and K. M. Zurek. „Light Dark Matter: Models and Constraints“. In: *Phys. Rev. D* 96 (2017), p. 115021. DOI: 10.1103/PhysRevD.96.115021 (cit. on p. 4).
- [43] D. Antypas et al. *New Horizons: Scalar and Vector Ultralight Dark Matter*. 2022 (cit. on p. 4).
- [44] C. Delaunay et al. „Probing atomic Higgs-like forces at the precision frontier“. In: *Phys. Rev. D* 96 (2017), p. 093001. DOI: 10.1103/PhysRevD.96.093001 (cit. on p. 4).
- [45] C. Delaunay et al. „Probing new spin-independent interactions through precision spectroscopy in atoms with few electrons“. In: *Phys. Rev. D* 96 (2017), p. 115002. DOI: 10.1103/PhysRevD.96.115002 (cit. on p. 4).
- [46] C. Frugiuele et al. „Constraining new physics models with isotope shift spectroscopy“. In: *Phys. Rev. D* 96 (2017), p. 015011. DOI: 10.1103/PhysRevD.96.015011 (cit. on p. 4).
- [47] J. C. Berengut et al. „Probing New Long-Range Interactions by Isotope Shift Spectroscopy“. In: *Phys. Rev. Lett.* 120 (2018), p. 091801. DOI: 10.1103/PhysRevLett.120.091801 (cit. on pp. 4, 6).
- [48] J. C. Berengut et al. „Generalized King linearity and new physics searches with isotope shifts“. In: *Phys. Rev. Res.* 2 (2020), p. 043444. DOI: 10.1103/PhysRevResearch.2.043444 (cit. on p. 4).
- [49] W. H. King. *Isotope shifts in atomic spectra*. Springer Science & Business Media, 1984 (cit. on p. 4).
- [50] D. A. Nesterenko et al. „Phase-Imaging Ion-Cyclotron-Resonance technique at the JYFLTRAP double Penning trap mass spectrometer“. en. In: *Eur. Phys. J. A* 54.9 (2018), p. 154. DOI: 10.1140/epja/i2018-12589-y (cit. on p. 4).
- [51] D. A. Nesterenko et al. „Study of radial motion phase advance during motion excitations in a Penning trap and accuracy of JYFLTRAP mass spectrometer“. en. In: *Eur. Phys. J. A* 57.11 (2021), p. 302. DOI: 10.1140/epja/s10050-021-00608-3 (cit. on p. 5).

- [52] S. O. Allehabi et al. „Nuclear deformation as a source of the nonlinearity of the King plot in the Yb^+ ion“. In: *Phys. Rev. A* 103 (2021), p. L030801. DOI: 10.1103/PhysRevA.103.L030801 (cit. on pp. 5, 87).
- [53] **M. Door*** et al. *Search for new bosons with ytterbium isotope shifts*. 2024. DOI: 10.48550/arXiv.2403.07792 (cit. on pp. 5, 85, 87, 88, 91).
- [54] H. Dehmelt. „Radiofrequency Spectroscopy of Stored Ions I: Storage**Part II: Spectroscopy is now scheduled to appear in Volume V of this series.“ In: ed. by D. Bates and I. Estermann. Vol. 3. *Advances in Atomic and Molecular Physics*. Academic Press, 1968, pp. 53–72. DOI: [https://doi.org/10.1016/S0065-2199\(08\)60170-0](https://doi.org/10.1016/S0065-2199(08)60170-0) (cit. on pp. 7, 8).
- [55] F. Herfurth and K. Blaum. *Trapped Charged Particles and Fundamental Interactions*. en. Vol. 749. *Lecture Notes in Physics*. Berlin, Heidelberg: Springer, 2008. DOI: 10.1007/978-3-540-77817-2 (cit. on p. 7).
- [56] M. Vogel. *Particle Confinement in Penning Traps*. Vol. 100. *Springer Series on Atomic, Optical, and Plasma Physics*. Cham: Springer International Publishing, 2018. DOI: 10.1007/978-3-319-76264-7 (cit. on p. 7).
- [57] L. S. Brown and G. Gabrielse. „Geonium theory: Physics of a single electron or ion in a Penning trap“. In: *Rev. Mod. Phys.* 58 (1 1986), pp. 233–311. DOI: 10.1103/RevModPhys.58.233 (cit. on pp. 7, 25).
- [58] C. Roux et al. „The trap design of PENTATRAP“. In: *Applied Physics B* 107.4 (2011), pp. 997–1005. DOI: 10.1007/s00340-011-4825-4 (cit. on pp. 8, 35, 81).
- [59] C. E. Roux. „High-resolution mass spectrometry. The trap design and detection system of Pentatrap and new Q-values for neutrino studies“. eng. PhD thesis. Heidelberg University, 2012, Online-Ressource (cit. on pp. 8, 17, 25, 27, 35, 39–42, 63, 93).
- [60] G. Gabrielse, L. Haarsma, and S. Rolston. „Open-endcap Penning traps for high precision experiments“. In: *International Journal of Mass Spectrometry and Ion Processes* 88.2 (1989), pp. 319–332. DOI: [https://doi.org/10.1016/0168-1176\(89\)85027-X](https://doi.org/10.1016/0168-1176(89)85027-X) (cit. on p. 8).
- [61] C. Diehl. „First mass measurements with the MPIK/UW-PTMS“. eng. PhD thesis. Heidelberg, Univ., Diss., 2011, p. 128 (cit. on p. 8).
- [62] J. Ketter. „Theoretical treatment of miscellaneous frequency-shifts in Penning traps with classical perturbation theory“. eng. PhD thesis. Heidelberg, Univ., Diss., 2015, p. 231 (cit. on pp. 8, 16–18, 22).
- [63] H. Dehmelt. „Radiofrequency Spectroscopy of Stored Ions II: Spectroscopy**Part I, Sections 1 and 2 of this article appear in Volume 3 of this series.“ In: ed. by D. Bates and I. Estermann. Vol. 5. *Advances in Atomic and Molecular Physics*. Academic Press, 1969, pp. 109–154. DOI: [https://doi.org/10.1016/S0065-2199\(08\)60156-6](https://doi.org/10.1016/S0065-2199(08)60156-6) (cit. on p. 8).
- [64] G. Gabrielse and F. Mackintosh. „Cylindrical Penning traps with orthogonalized anharmonicity compensation“. In: *International Journal of Mass Spectrometry and Ion Processes* 57.1 (1984), pp. 1–17. DOI: [https://doi.org/10.1016/0168-1176\(84\)85061-2](https://doi.org/10.1016/0168-1176(84)85061-2) (cit. on p. 8).
- [65] L. S. Brown and G. Gabrielse. „Precision spectroscopy of a charged particle in an imperfect Penning trap“. In: *Phys. Rev. A* 25 (4 1982), pp. 2423–2425. DOI: 10.1103/PhysRevA.25.2423 (cit. on pp. 10, 20).
- [66] J. L. Verdú. „Ultrapräzise Messung des elektronischen g -Faktors in wasserstoffähnlichem Sauerstoff“. eng. PhD thesis. (Johannes Gutenberg-Universität Mainz, 2003 (cit. on p. 11).
- [67] L. Schweikhard and A. G. Marshall. „Excitation modes for fourier transform-ion cyclotron resonance mass spectrometry“. In: *Journal of the American Society for Mass Spectrometry* 4.6 (1993). PMID: 24235002, pp. 433–452. DOI: 10.1016/1044-0305(93)80001-F (cit. on p. 11).

- [68] *The International System of Units (SI)*. 9th. Sèvres, France: Bureau International des Poids et Mesures, 2019 (cit. on p. 11).
- [69] S. Rainville, J. K. Thompson, and D. E. Pritchard. „An Ion Balance for Ultra-High-Precision Atomic Mass Measurements“. English. In: *Science* 303.5656 (2004), pp. 334–338 (cit. on pp. 12, 47, 95).
- [70] S. Rainville. „A two-ion balance for high precision mass spectrometry“. eng. PhD thesis. Massachusetts Institute of Technology, Dept. of Physics., 2003 (cit. on pp. 12, 94).
- [71] J. K. Thompson. „Two-Ion Control and Polarization Forces for Precise Mass Comparisons“. eng. PhD thesis. Massachusetts Institute of Technology, Dept. of Physics., 2003 (cit. on pp. 12, 94).
- [72] P. R. H. et al. „Measurement of the fine-structure constant as a test of the Standard Model“. In: *Science* 360 (6385 2018), pp. 191–195. DOI: 10.1126/science.aap7706 (cit. on pp. 12, 89, 96).
- [73] L. Morel et al. „Determination of the fine-structure constant with an accuracy of 81 parts per trillion“. In: *Nature* 588 (7836 2020), p. 61. DOI: 10.1038/s41586-020-2964-7 (cit. on pp. 12, 63, 89, 96).
- [74] K. Kromer et al. „High-precision mass measurement of doubly magic ^{208}Pb “. In: *Eur. Phys. J. A* 58 (10 2022), p. 202. DOI: 0.1140/epja/s10050-022-00860-1 (cit. on pp. 12, 35).
- [75] W. J. Huang et al. „The AME 2020 atomic mass evaluation (I). Evaluation of input data, and adjustment procedures“. In: *Chinese Phys. C* 45.3 (2021), p. 030002. DOI: 10.1088/1674-1137/abddb0 (cit. on pp. 12, 63, 74, 81, 85, 86).
- [76] J. Verdú et al. „Calculation of electrostatic fields using quasi-Green's functions: Application to the hybrid Penning trap“. In: *New Journal of Physics* 10 (2008) (cit. on p. 16).
- [77] J. Ketter et al. „First-order perturbative calculation of the frequency-shifts caused by static cylindrically-symmetric electric and magnetic imperfections of a Penning trap“. In: *International Journal of Mass Spectrometry* 358 (2014), pp. 1–16. DOI: <https://doi.org/10.1016/j.ijms.2013.10.005> (cit. on pp. 17–19, 21, 23).
- [78] S. Dickopf. „High-precision Penning-trap measurements of the magnetic moments and hyperfine splitting in hydrogen-like beryllium-9“. eng. PhD thesis. Heidelberg, Univ., Diss., 2024 (cit. on pp. 18, 20, 30, 59).
- [79] M. Door. „New Controlsystem and first trap characterization measurements at the high-precision Penning-trap mass spectrometer Pentatrap“. eng. MA thesis. Heidelberg University, 2018 (cit. on pp. 18, 19, 35, 37, 38, 58).
- [80] T. Sailer. „Direct Bound-Electron g -Factor Difference Measurement of Coupled Ions at Alphasrap“. eng. PhD thesis. Heidelberg, Univ., Diss., 2022 (cit. on pp. 20, 75, 92).
- [81] A. Dörr. „PENTATRAP – a novel Penning-trap system for high-precision mass measurements“. eng. PhD thesis. Heidelberg, Univ., Diss., 2015, Online-Ressource (172 S.) (Cit. on pp. 20, 35–37, 41, 43).
- [82] F. Köhler. „Bound-Electron g -Factor Measurements for the Determination of the Electron Mass and Isotope Shifts in Highly Charged Ions“. eng. PhD thesis. Heidelberg University, 2015 (cit. on pp. 21, 31, 59, 60).
- [83] S. Rau. „High-precision measurement of the deuteron's atomic mass“. PhD thesis. Heidelberg University, 2020. DOI: 10.11588/heidok.00029010 (cit. on pp. 21, 23, 27–29, 60).
- [84] M. Schuh et al. „Image charge shift in high-precision Penning traps“. In: *Phys. Rev. A* 100 (2 2019), p. 023411. DOI: 10.1103/PhysRevA.100.023411 (cit. on pp. 21, 22, 61).
- [85] K. Kromer et al. „Atomic mass determination of uranium-238“. In: *Phys. Rev. C* 109 (2 2024), p. L021301. DOI: 10.1103/PhysRevC.109.L021301 (cit. on pp. 21, 61, 62, 90).

- [86] E. A. Cornell et al. „Mode coupling in a Penning trap: π pulses and a classical avoided crossing“. In: *Phys. Rev. A* 41 (1 1990), pp. 312–315. DOI: 10.1103/PhysRevA.41.312 (cit. on pp. 24, 29).
- [87] S. Ulmer. „First observation of spin flips with a single proton stored in a cryogenic Penning trap“. eng. PhD thesis. Heidelberg, Univ., 2011, Online-Ressource (cit. on p. 24).
- [88] D. J. Wineland and H. G. Dehmelt. „Principles of the stored ion calorimeter“. In: *J. Appl. Phys.* 46.2 (1975), pp. 919–930. DOI: 10.1063/1.321602 (cit. on p. 25).
- [89] S. R. Jefferts et al. „Superconducting resonator and a cryogenic GaAs field-effect transistor amplifier as a single-ion detection system“. In: *Review of Scientific Instruments* 64 (1993), p. 737. DOI: 10.1063/1.1144153 (cit. on p. 25).
- [90] W. Shockley. „Currents to Conductors Induced by a Moving Point Charge“. In: *Journal of Applied Physics* 9.10 (1938), pp. 635–636. DOI: 10.1063/1.1710367 (cit. on p. 25).
- [91] H. Nyquist. „Thermal Agitation of Electric Charge in Conductors“. In: *Phys. Rev.* 32 (1 1928), pp. 110–113. DOI: 10.1103/PhysRev.32.110 (cit. on p. 26).
- [92] J. B. Johnson. „Thermal Agitation of Electricity in Conductors“. In: *Phys. Rev.* 32 (1 1928), pp. 97–109. DOI: 10.1103/PhysRev.32.97 (cit. on p. 26).
- [93] S. Sturm. „The g -factor of the electron bound in $^{28}\text{Si}^{13+}$: the most stringent test of bound-state quantum electrodynamics“. eng. PhD thesis. Mainz: Johannes-Gutenberg Universität, 2012. DOI: 10.25358/OPENSCIENCE-2019 (cit. on pp. 27–30, 41).
- [94] A. Rischka. „The First Direct Q_{EC} Measurement in ^{163}Ho and the Development of the High-Precision Mass Spectrometer PENTATRAP for Neutrino Physics“. eng. PhD thesis. Heidelberg University, 2018 (cit. on pp. 27, 29, 35–37, 39, 41, 47, 59).
- [95] E. A. Cornell et al. „Single-ion cyclotron resonance measurement of $M(\text{CO}^+)/M(\text{N}_2^+)$ “. In: *Phys. Rev. Lett.* 63 (16 1989), pp. 1674–1677. DOI: 10.1103/PhysRevLett.63.1674 (cit. on p. 29).
- [96] A. Egl. „High-Precision Laser Spectroscopy of the Fine Structure in $^{40}\text{Ar}^{13+}$ at ALPHA-TRAP“. eng. PhD thesis. Heidelberg, Univ., Diss., 2020 (cit. on pp. 29, 59).
- [97] R. X. Schüssler. „First High-Precision Mass Measurements at PENTATRAP on highly charged Xe and Re ions“. eng. PhD thesis. Heidelberg University, 2020 (cit. on pp. 30, 31, 33, 35, 37, 39, 41, 50, 52, 89, 95).
- [98] R. X. Schüssler et al. „Recent Developments at the High-Precision Mass Spectrometer PENTATRAP“. In: *JPS Conf. Proc.* 18 (2017), p. 011020. DOI: 10.7566/JSPC.18.011020 (cit. on pp. 35, 37).
- [99] J. M. A. Repp. „The setup of the high-precision Penning-trap mass spectrometer PENTATRAP and first production studies of highly charged ions“. eng. PhD thesis. Heidelberg, Univ., Diss., 2012, Online-Ressource (cit. on pp. 35, 39, 41).
- [100] C. Böhm. *High-precision mass measurements of neutron-deficient Tl isotopes at ISOLTRAP and the development of an ultra-stable voltage source for the PENTATRAP experiment*. eng. 2015, p. 128 (cit. on pp. 35, 44).
- [101] M. Door. „Erzeugung hochgeladener Chlor- und Siliziumionen für das Pentatrap-Experiment in einer Elektronenstrahlionenquelle unter Anwendung der MIVOC-Methode“. deu. Bachelor thesis. Heidelberg University, 2015 (cit. on pp. 35–37, 64).
- [102] P. Micke et al. „The Heidelberg compact electron beam ion traps“. In: *Rev. Sci. Instrum.* 89.6 (2018), p. 063109. DOI: 10.1063/1.5026961 (cit. on p. 35).
- [103] B. M. Penetrante et al. „Evaporative cooling of highly charged dysprosium ions in an enhanced electron-beam ion trap“. In: *Phys. Rev. A* 43 (9 1991), pp. 4873–4882. DOI: 10.1103/PhysRevA.43.4873 (cit. on pp. 36, 64).
- [104] C. Schweiger et al. „Production of highly charged ions of rare species by laser-induced desorption inside an electron beam ion trap“. In: *Rev. Sci. Instrum.* 90.12 (2019), p. 123201. DOI: 10.1063/1.5128331 (cit. on pp. 36, 77).

- [105] U. Kentsch et al. „Dresden EBIT: Results and perspectives“. English. In: *Review of Scientific Instruments* 71.2 (2002), pp. 660–662. DOI: 10.1063/1.1429311 (cit. on pp. 36, 37).
- [106] N. E. Bradbury and R. A. Nielsen. „Absolute Values of the Electron Mobility in Hydrogen“. In: *Phys. Rev.* 49 (5 1936), pp. 388–393. DOI: 10.1103/PhysRev.49.388 (cit. on p. 37).
- [107] C. Schweiger et al. „Fast silicon carbide MOSFET based high-voltage push–pull switch for charge state separation of highly charged ions with a Bradbury–Nielsen gate“. In: *Review of Scientific Instruments* 93.9 (2022), p. 094702. DOI: 10.1063/5.0083515 (cit. on p. 37).
- [108] E. Piselli et al. „CERN Accelerators Beam Optimization Algorithm“. In: *Proc. ICALEPCS'19* (New York, NY, USA). International Conference on Accelerator and Large Experimental Physics Control Systems 17. JACoW Publishing, Geneva, Switzerland, 2020, pp. 1379–1384. DOI: 10.18429/JACoW-ICALEPCS2019-WEPHA124 (cit. on p. 37).
- [109] K. Kromer. „Environmentally-induced systematic effects at the high-precision mass spectrometer PENTATRAP.“ eng. MA thesis. Heidelberg University, 2019 (cit. on pp. 38, 54, 68).
- [110] A. Rischka. „Aufbau des Stabilisierungssystems des Heliumdrucks und Heliumlevels und Konstruktion eines kryogenen Faraday-Bechers für PENTATRAP“. deu. MA thesis. Heidelberg University, 2014 (cit. on p. 38).
- [111] *Bronkhorst Mass Flow Controller F-201*. <https://www.bronkhorst.com/en-gb/products/gas-flow-en/low-p-flow/f-201ev/>. Accessed on 2024-05-06. 2024 (cit. on p. 38).
- [112] *Paroscientific, Inc., 6000-23A Absolute Pressure Transducer*. <https://paroscientific.com/products.php>. Accessed on 2024-05-06. 2024 (cit. on p. 38).
- [113] R. X. Schüssler. „A new Detection System for the high-precision Penning-trap mass spectrometer PENTATRAP“. eng. MA thesis. Heidelberg University, 2015 (cit. on p. 41).
- [114] J.-W. Heo et al. „Characteristics of GaAs varactor diode with hyperabrupt doping profile“. In: *physica status solidi (a)* 212.3 (2015), pp. 612–616. DOI: <https://doi.org/10.1002/pssa.201431539> (cit. on p. 41).
- [115] C. Böhm et al. „An ultra-stable voltage source for precision Penning-trap experiments“. English. In: *Nuclear Instruments and Methods in Physics Research, A* 828 (2016), pp. 125–131 (cit. on pp. 43, 44).
- [116] *Analog Devices, LTZ1000 Ultra Precision Reference*. <https://www.analog.com/en/products/ltz1000.html>. Accessed on 2024-05-08. 2024 (cit. on p. 44).
- [117] S. Bauer et al. „Josephson voltage standards as toolkit for precision metrological applications at PTB“. In: *Measurement Science and Technology* 34.3 (2022), p. 032001. DOI: 10.1088/1361-6501/aca5a5 (cit. on p. 44).
- [118] A. Kaiser et al. „Josephson voltage standards as an ultra-stable low-noise voltage source for precision Penning-trap experiments“. In: *Applied Physics Letters* 124 (2024), p. 000000. DOI: 10.1063/5.0206779 (cit. on p. 46).
- [119] M. Carstens. *RME - Fireface UC*. <https://rme-audio.de/de/fireface-uc.html>. 2024 (cit. on p. 47).
- [120] J. E. Cavanaugh. „Unifying the derivations for the Akaike and corrected Akaike information criteria“. In: *Stat. & Probab. Lett.* 33.2 (1997), pp. 201–208. DOI: [https://doi.org/10.1016/S0167-7152\(96\)00128-9](https://doi.org/10.1016/S0167-7152(96)00128-9) (cit. on p. 55).
- [121] S. Rau et al. „Penning trap mass measurements of the deuteron and the HD⁺ molecular ion“. In: *Nature* 585.7823 (7823 2020), pp. 43–47. DOI: 10.1038/s41586-020-2628-7 (cit. on p. 74).
- [122] S. Sasidharan et al. „Penning-Trap Mass Measurement of Helium-4“. In: *Phys. Rev. Lett.* 131 (9 2023), p. 093201. DOI: 10.1103/PhysRevLett.131.093201 (cit. on p. 74).

- [123] G. Breit. „The Magnetic Moment of the Electron“. In: *Nature* 122 (3078 1928), p. 649. DOI: 10.1038/122649a0 (cit. on p. 75).
- [124] V. A. Yerokhin, P. Indelicato, and V. M. Shabaev. „Evaluation of the self-energy correction to the g factor of S states in H-like ions“. In: *Phys. Rev. A* 69 (5 2004), p. 052503. DOI: 10.1103/PhysRevA.69.052503 (cit. on p. 75).
- [125] V. A. Yerokhin and Z. Harman. „One-loop electron self-energy for the bound-electron g factor“. In: *Phys. Rev. A* 95 (6 2017), p. 060501. DOI: 10.1103/PhysRevA.95.060501 (cit. on p. 75).
- [126] V. A. Yerokhin, C. H. Keitel, and Z. Harman. „Nuclear-size self-energy and vacuum-polarization corrections to the bound-electron g factor“. In: *J. Phys. B: At. Mol.* 46.24 (2013), p. 245002. DOI: 10.1088/0953-4075/46/24/245002 (cit. on p. 75).
- [127] H. Grotch. „Electron g Factor in Hydrogenic Atoms“. In: *Phys. Rev. Lett.* 24 (2 1970), pp. 39–42. DOI: 10.1103/PhysRevLett.24.39 (cit. on p. 75).
- [128] K. Kromer et al. „Observation of a Low-Lying Metastable Electronic State in Highly Charged Lead by Penning-Trap Mass Spectrometry“. In: *Phys. Rev. Lett.* 131 (22 2023), p. 223002. DOI: 10.1103/PhysRevLett.131.223002 (cit. on pp. 78, 95).
- [129] C. Lyu. *Private Communication*. Private communication. Private communication. 2023 (cit. on pp. 79, 87, 92).
- [130] C. Froese Fischer et al. „GRASP2018 – A Fortran 95 version of the General Relativistic Atomic Structure Package“. In: *Comput. Phys. Commun.* 237 (2019), p. 184. DOI: <https://doi.org/10.1016/j.cpc.2018.10.032> (cit. on p. 85).
- [131] C.-H. Yeh. „Precision spectroscopy of ytterbium ions for tests of fundamental physics“. PhD thesis. Leibniz Universität Hannover, 2024 (cit. on pp. 87, 88, 91).
- [132] S. Sturm et al. „Phase-Sensitive Cyclotron Frequency Measurements at Ultralow Energies“. In: *Phys. Rev. Lett.* 107 (14 2011), p. 143003. DOI: 10.1103/PhysRevLett.107.143003 (cit. on p. 90).
- [133] J. Herkenhoff et al. „A digital feedback system for advanced ion manipulation techniques in Penning traps“. In: *Rev. Sci. Instrum.* 92.10 (2021), p. 103201 (cit. on pp. 90, 93).
- [134] M. Heinz. „tbd“. PhD thesis. TU Darmstadt, 2024 (cit. on p. 91).
- [135] **M. Door** and et al. *Nonlinear isotope shifts in calcium*. (2024) in preparation (cit. on p. 91).
- [136] B. Tu et al. „Front Cover: Tank-Circuit Assisted Coupling Method for Sympathetic Laser Cooling (Adv. Quantum Technol. 7/2021)“. In: *Advanced Quantum Technologies* 4.7 (2021), p. 2170071. DOI: <https://doi.org/10.1002/qute.202170071> (cit. on p. 94).
- [137] M. Bohman et al. „Sympathetic cooling of a trapped proton mediated by an LC circuit“. In: *Nature* 596.7873 (2021), pp. 514–518. DOI: 10.1038/s41586-021-03784-w (cit. on p. 94).
- [138] J. R. C. López-Urrutia. „Frequency metrology using highly charged ions“. In: *Journal of Physics: Conference Series* 723.1 (2016), p. 012052. DOI: 10.1088/1742-6596/723/1/012052 (cit. on p. 95).
- [139] C. Lyu et al. „Interrogating the Temporal Coherence of EUV Frequency Combs with Highly Charged Ions“. In: *Phys. Rev. Lett.* 125 (9 2020), p. 093201. DOI: 10.1103/PhysRevLett.125.093201 (cit. on p. 95).
- [140] C. Lyu, C. H. Keitel, and Z. Harman. „Ultrastable optical, XUV and soft-x-ray clock transitions in open-shell highly charged ions“. In: (2023) (cit. on p. 95).
- [141] **M. Door*** and et al. *Binding energy determination of the valence electron in $^{172}\text{Yb}^{41+}$ and $^{172}\text{Yb}^{42+}$ to test QED*. (2024) in preparation.

Appendix A

Appendix

A.1 Ytterbium cyclotron frequency ratios

Summary of all determined cyclotron frequency ratios of ytterbium isotopes which have not been shown within the main text. The first figure has the complete description in the caption, the latter only the ion species.

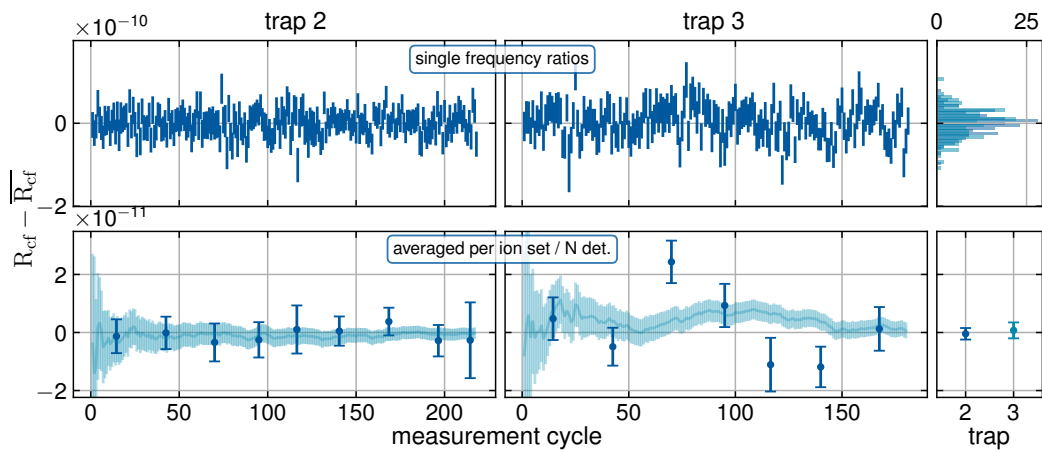


Figure A.1: Cyclotron frequency ratios (via interpolation method) of $^{168}\text{Yb}^{42+}$ and $^{172}\text{Yb}^{42+}$ ions minus the total mean frequency ratio. The top panels show each determined ratio over chronological measurement numbering (discarded data is not shown) for the two measurement traps 2 and 3 and both dataset as histograms on the right. The lower panels show the average results of data-groups with individual phase unwrap and N determinations as well as the evolving total average in the background. The lower right panel show the final average of each trap.

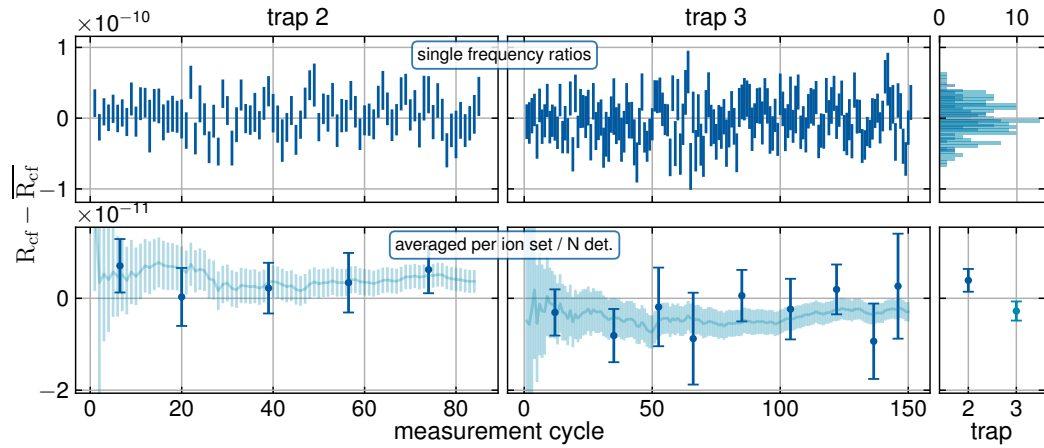


Figure A.2: Cyclotron frequency ratios (via interpolation method) of $^{170}\text{Yb}^{42+}$ and $^{172}\text{Yb}^{42+}$ ions minus the total mean frequency ratio.

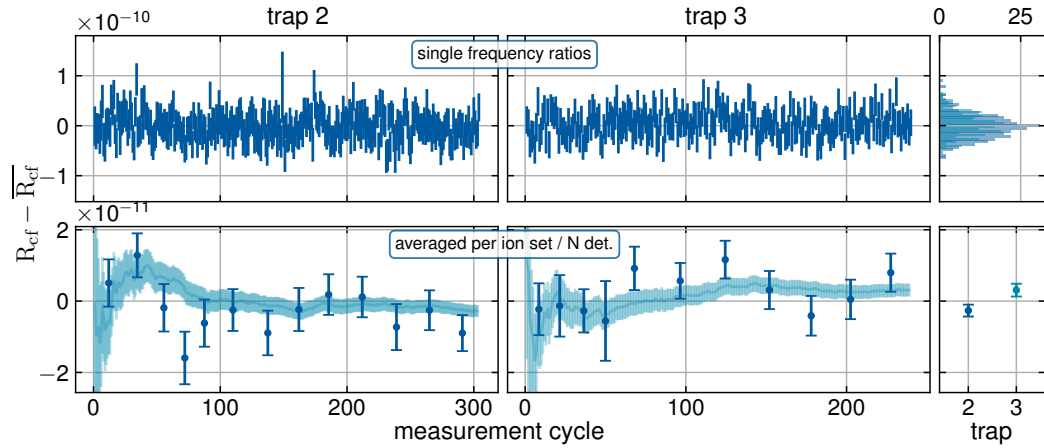


Figure A.3: Cyclotron frequency ratios (via interpolation method) of $^{174}\text{Yb}^{42+}$ and $^{172}\text{Yb}^{42+}$ ions minus the total mean frequency ratio.

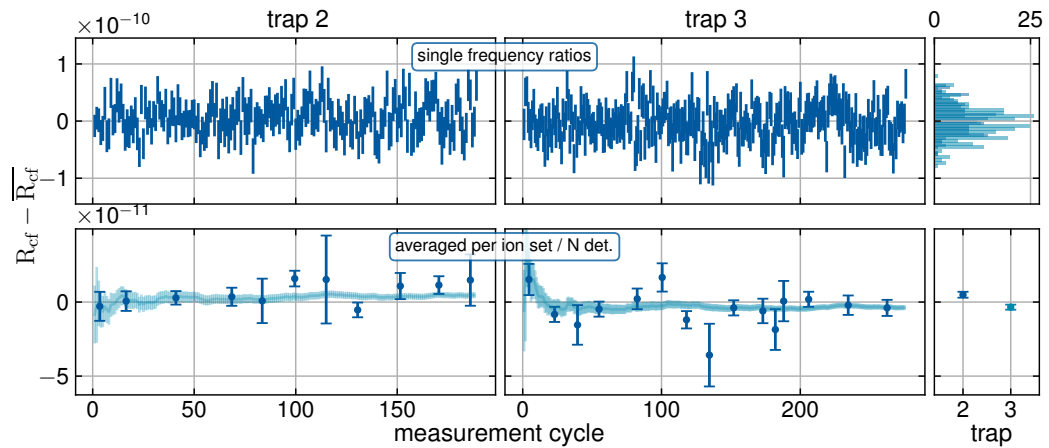


Figure A.4: Cyclotron frequency ratios (via interpolation method) of $^{172}\text{Yb}^{43+}$ and $^{172}\text{Yb}^{42+}$ ions minus the total mean frequency ratio.

A.2 Impact of fluctuating electrostatic potential

The impact of fluctuations of the potential source is described in section 3.2.3. Here is an overview plot of how a white noise fluctuation on U_0 of $1\ \mu\text{V}$ would impact the corresponding reduced cyclotron frequency:

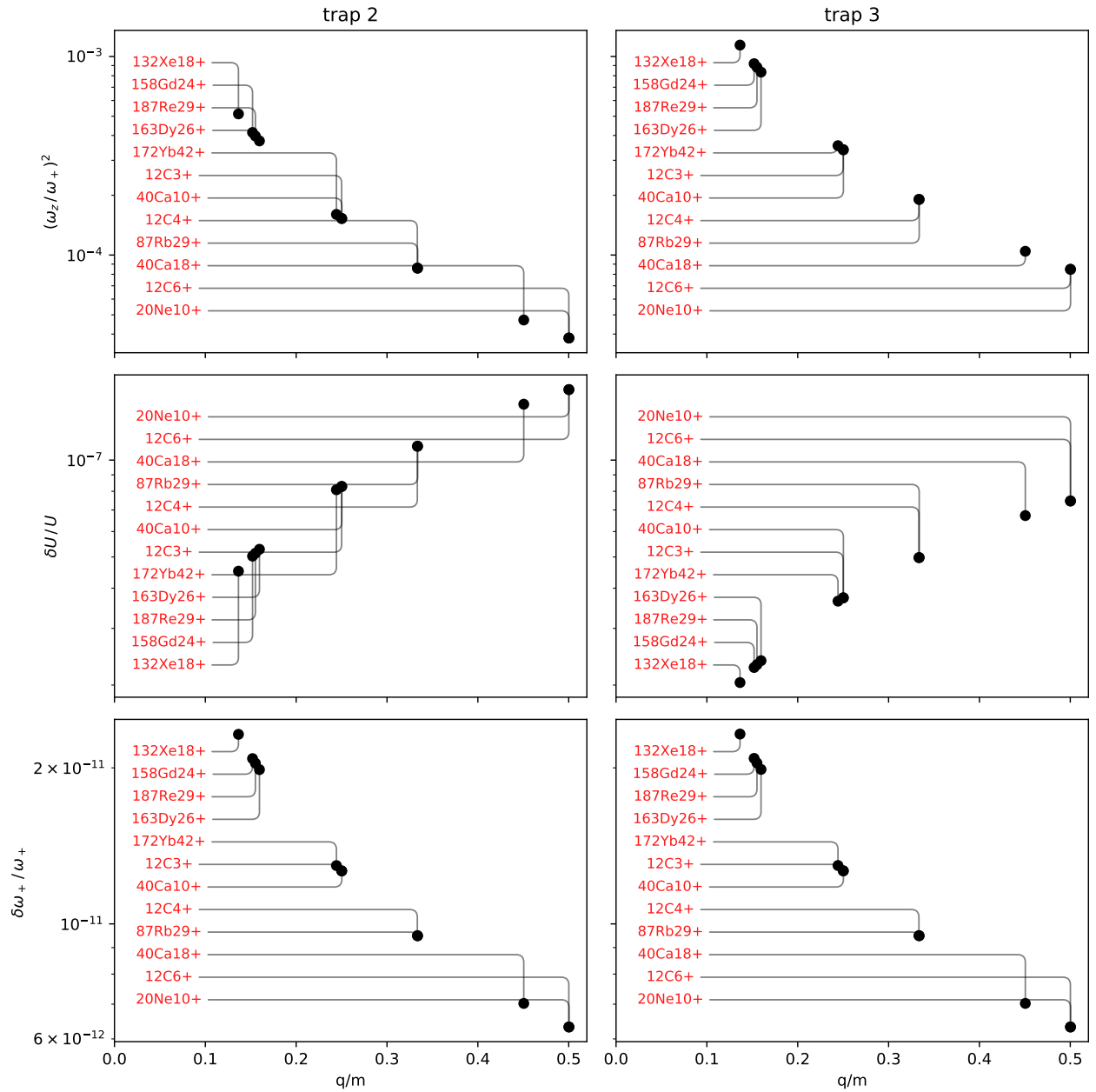


Figure A.5: Impact of white noise on the trap depth potential with a standard deviation of $\delta U = 1\ \mu\text{V}$ over the measurement time relative to the necessary voltage U_0 to tune the axial frequency in resonance with the detection system (top), the specific impact factor on the reduced cyclotron frequency for given the charge-to-mass ratio q/m (middle) and the resulting stability $\delta\omega_+/\omega_+$ (bottom).

Acknowledgements

Für die langen Jahre, die ich am PENTATRAP-Experiment arbeiten durfte, danke ich natürlich dir, Klaus. Es ist absolut beeindruckend, wie du es schaffst, mit der großen Menge an Mitglieder in deiner Gruppe nie den Überblick über die einzelnen Projekte zu verlieren und immer mit Rat und Tat zur Verfügung stehst, wenn es irgendwo Probleme gibt. Danke für die langjährige Unterstützung und für die einzigartigen Freiheiten, welche du mir und allen anderen in der Abteilung gibst, um unsere Möglichkeiten voll ausschöpfen zu können. Und natürlich großen Dank für die zahlreichen last minute Kommentare, welche du mir noch um Mitternacht innerhalb weniger Minuten zu Präsentationen und Texten gegeben hast. Danke für alles!

I would like to thank Prof. Skyler Degenkolb for being the second examiner of this thesis and for his kind support throughout the writing process.

Vielen Dank an dich, Sergey, für deine Unterstützung, für zahlreiche Diskussionen über Messungen und deine verlässliche Leitung von PENTATRAP.

Besonderen Dank an Alex: Du hast mich von Beginn an bei PENTATRAP betreut und alle meine Labor-Fähigkeiten habe ich von dir gelernt. Du bist ein hervorragender Kollege gewesen, nicht nur wegen deiner essentiellen Beiträge zum Experiment, sondern auch durch deine Kollegialität und der besten Kombination aus Unterstützung, Begeisterung und hohen Erwartungen, die man sich wünschen kann. Vielen Dank für deine Zeit, die du in das Experiment und mich investiert hast.

Vielen Dank an all die Doktorandinnen, Doktoranden und Studierenden von PENTATRAP, die mich im Laufe der Zeit begleitet haben: Rima, Christoph, Kathrin, Jost, Daniel und alle anderen ehemaligen und aktuellen Kolleginnen und Kollegen für eure Teilnahme und Beiträge zum Experiment und auch für die nette Zeit mit euch als Büronachbarinnen und -nachbarn und Kicker-Rivalen.

Thank you Pavel for your continued work at the PENTATRAP-experiment and for continuing and improving the analysis package.

Chunhai und Zoltan, thank you for your calculations of binding energies to such amazing accuracy and also for the contributions to the publications.

Fabian - Danke für deine zahlreichen Hilfen bei der Suche nach passender Literatur, für deine Gründlichkeit bei der Diskussion von *esoterischen* systematischen Effekten, für die gute Zusammenarbeit bei der Veröffentlichung zur g -Faktor-Bestimmung, für die Diskussionen über neue Messmethoden und -motivationen und für deine allgegenwärtige hilfsbereite Einstellung.

Tim - Danke auch dir für die Kollaboration in der Neon g -Faktor-Bestimmung.

Sven - Vielen Dank für Diskussionen und Hilfen zu jeglichen Themen, die irgendwie in Verbindung mit Penning-Fallen Experimenten stehen. Deine Kenntnisse sind einfach beeindruckend und fast jedes Gespräch mit dir endet mit einer guten Antwort auf eine Frage und zahlreichen interessanten neuen Fragen, über die man vorher gar nicht nachgedacht hat.

Stefan - Vielen Dank für unsere zahlreichen Gespräche zu systematischen Effekten und für die häufigen Mitfahrgelegenheiten.

Vielen Dank an all die Kolleginnen und Kollegen der MPIK Infrastruktur, allen voran der Elektronik-Abteilung, der Konstruktion und Mechanik und der Haustechnik! Eure Flexibilität, gute Kommunikation und eure Fähigkeiten erlauben es beeindruckend schnell Probleme zu Lösen und Ideen umzusetzen.

Großer Dank gilt auch den vielen Kollaborationspartnern mit denen ich zusammenarbeiten durfte: Luis und Ralf von der Josephson-Effect Abteilung der PTB, vielen Dank für die Bereitstellung der Josephson Voltage Source und euren außerordentlich guten Support, Diskussionen zu Messmethoden und Elektronik und eure Hilfe bei den Interpretationen der Messdaten.

Thanks also to Indy and Alexander from the PTB for their determinations of isotope shifts in ytterbium and calcium and the resulting shared publications. My measurements are only usefull in combination with yours, thank you.

Danke an meine Freunde in Heidelberg und auswärts, ihr habt mir über viele Jahre den notwendigen sozialen Halt gegeben. Besonderer Dank an André den Statistik-Guru ;)

Abschließend möchte ich meiner Familie danken. Trotz meiner Abwesenheit habt ihr es geschafft mich ab und zu aus meiner Bubble zu holen. Vielen Dank für eure Unterstützung vor und während meiner ganzen Studienzeit.

Danke, Helen, für deine Hilfe, dein Verständnis, deine Treue und Zuverlässigkeit, die Pausen, das Pushen, und für so vieles mehr.